Title
A Measurement of the Degree Scale B-mode CMB Angular Power Spectrum from the Polarbear Experiment

Author
Goeckner-Wald, Neil

Publication Date
2019

Peer reviewed|Thesis/dissertation

A Measurement of the Degree Scale B-mode CMB Angular Power Spectrum from the POLARBEAR Experiment

by

Neil Goeckner-Wald

A dissertation submitted in partial satisfaction of the

requirements for the degree of

Doctor of Philosophy

in

Physics

in the

Graduate Division

of the

University of California, Berkeley

Committee in charge:

Professor Adrian Lee, Chair
Professor William Holzapfel
Associate Professor Aaron Parsons

Summer 2019

A Measurement of the Degree Scale B-mode CMB Angular Power Spectrum from the POLARBEAR Experiment

Abstract

A Measurement of the Degree Scale B-mode CMB Angular Power Spectrum from the POLARBEAR Experiment

by

Neil Goeckner-Wald

Doctor of Philosophy in Physics

University of California, Berkeley

Professor Adrian Lee, Chair

Measurements of the polarization anisotropies in the cosmic microwave background (CMB) provide powerful experimental constraints on the contents and history of the universe. These anisotropies are conventionally split by spatial parity, with even (odd) parity modes called E-modes (B-modes). The degree-scale (multipole moment $\ell \approx 100$) B-mode polarization is expected to receive a contribution from a stochastic gravitational wave background in the early universe. This feature is a generic prediction of theories of cosmic inflation, however its overall amplitude r is a free parameter. Detecting this gravitational wave signal presents a formidable experimental challenge.

This analysis is based on three years of data from the POLARBEAR experiment using a continuously rotating half-wave plate to modulate the CMB polarization. This dissertation describes the analysis pipeline used to transform the raw detector time ordered data (TOD) into a CMB power spectrum and likelihood on r. This analysis is the tightest constraint on the degree scale B-mode power spectrum yet achieved from a mid-lattitude site or with a polarization modulator. As such, it serves as a pathfinder for future instruments including the Simons Array and Simons Observatory.

This dissertation is structured as follows. Chapter 1 presents an overview of the science case for precise measurements of the CMB B-mode power spectrum. Chapter 2 gives a brief description of the POLARBEAR instrument and the observation strategy used in this dataset. Chapter 3 describes the data pre-processing and calibration steps used in this analysis. Chapter 4 describes the pipeline used to turn the TOD into maps and subsequently power spectra. Chapter 5 describes the sensitivity degradation seen at large angular scales in this analysis and how it may be mitigated in future experiments. Chapter 6 describes the final calibrations and consistency of this data with existing E-mode measurements. Chapters 7 and 8 describe the detailed internal consistency checks preformed and simulations of a number of known sources of systematic contamination. Chapter 9 shows the recovered B-mode angular power spectrum. Chapter 10 shows the cross correlation with data from the Planck satellite to control contamination due to galactic foregrounds and the likelihood

model for the constraint on r. Chapter 11 summarizes these results and describes future experiments.

To my father, who first inspired me to do this, and my mother,
who made sure I survived my childhood science experiments.

Contents

List of Figures

List of Tables

Acknowledgments

This result represents a contribution to many years worth of work from a large number of people in the POLARBEAR collaboration. There are several people without whose heroic efforts this result simply would have not been possible. Dave Boettger, Darcy Barron, Praween Siritanasak, and many others worked tirelessly during the observations to keep the telescope running smoothly. Much of the early stages of this project including the low-level data processing and low freqency noise mitigation was done by Satoru Takakura, who has been enormously helpful throughout the entire project.

Several other people directly contributed to the analysis. Davide Poletti worked out the details of the foreground cleaning, helped to cross check important parts of the pipeline and contributed to the text of the final results paper that will appear soon. Mario Aguilar contributed to the validation of our power spectrum estimator. Fred Matsuda and Tucker Elleflot built our pointing model and David Leon did some of the early work on the beam calibration. Anh Pham developed the relative gain calibration and Greg Jaehnig calculated the detector polarization angle and efficiencies. Ted Kisner and Kolen Cheung built and maintained the software environment that allowed simulations to be run on NERSC.

At Berkeley, Yuji Chinone and Akito Kusaka provided invaluable mentorship and guided the project. Reijo Keskitalo helped us to correctly understand the Planck data and how to incorporate it into our analysis. Nathan Whitehorn provided useful suggestions and perspective on a wide range of topics.

I would also like to thank the other graduate students and postdocs in Adrian Lee's group including Aamir Ali, Shawn Beckman, Kevin Crowley, Ari Cukierman, John Groh, Charles Hill, Oliver Jeong, Aashrita Mangu, Ben Westbrook and Yuyang Zhao for creating an enjoyable, constructive, and occasionally distracting work environment. The "SPT corner" consisting of Jessica Avva, Sam Guns, Nick Harrington, and Nick Huang provided endlessly amusing and sometimes useful commentary.

This entire project would not have happened without the vision of the POLARBEAR PIs including Adrian Lee (my advisor), Kam Arnold, Brian Keating, and Masashi Hazumi.

I would like to thank the other mentors and teachers that have helped me over the years including Marco Ramirez, Manfred Paulini, Steven Garoff, Kunal Ghosh, and Bogdan Wojtsekhowski.

Finally, I would like to thank Chelsea Finn for her love, support and encouragement.

Chapter 1

The Cosmic Microwave Background

The anisotropy of the cosmic microwave background (CMB) has become one of the leading probes in modern cosmology. This chapter presents a brief overview of the science case for precision measurements of the CMB. More detailed information can be found in a number of references including the CMB Stage 4 Science Book [1], the WMAP and Planck cosmology papers [2, 3], and the Simons Observatory science forecasting paper [4].

A schematic view of the history of the universe can be found in Figure 1.1. Quantum fluctuations in the earliest moments of the universe seeded the anisotropies in the CMB and subsequent growth of galaxy clusters. Tthe CMB provides a snapshot of the expanding and cooling universe at 370,000 years after the Big Bang when electrons and protons recombined to form neutral hydrogen making the universe transparent to light. The temperature and polarization anisotropies directly correspond to inhomogeneities in the early universe. These fluctuations provide a backlight that traces the growth of large-scale structure over the subsequent history of the universe. At present the expansion of the universe is accelerating due to an unknown effect termed "dark energy." This chapter will present this cosmological standard model and how constraints have been derived from the CMB.

1.1 The Big Bang theory and the FRW model

The modern view of cosmology first became widely accepted after a pair of papers published jointly in 1965. In the first paper [5], Penzias and Wilson showed an excess source of noise in a radio antenna located at Bell Labs in Holmdel, New Jersey that was isotropic and invariant with time. In a companion paper [6], Dicke, Peebles, Roll, and Wilkinson offered a theoretical explanation that the excess radio noise was a thermal artifact of the expanding early universe. As the universe cooled, electrons and protons recombined to form neutral hydrogen and decoupled from thermal radiation. The resulting black body spectral shape was preserved by the further expansion of the universe. Penzias and Wilson reported a current temperature of 3.5 K, close to the 2.725 ± 0.002 K value reported by the FIRAS spectrometer aboard the COBE satellite [7] several decades later.

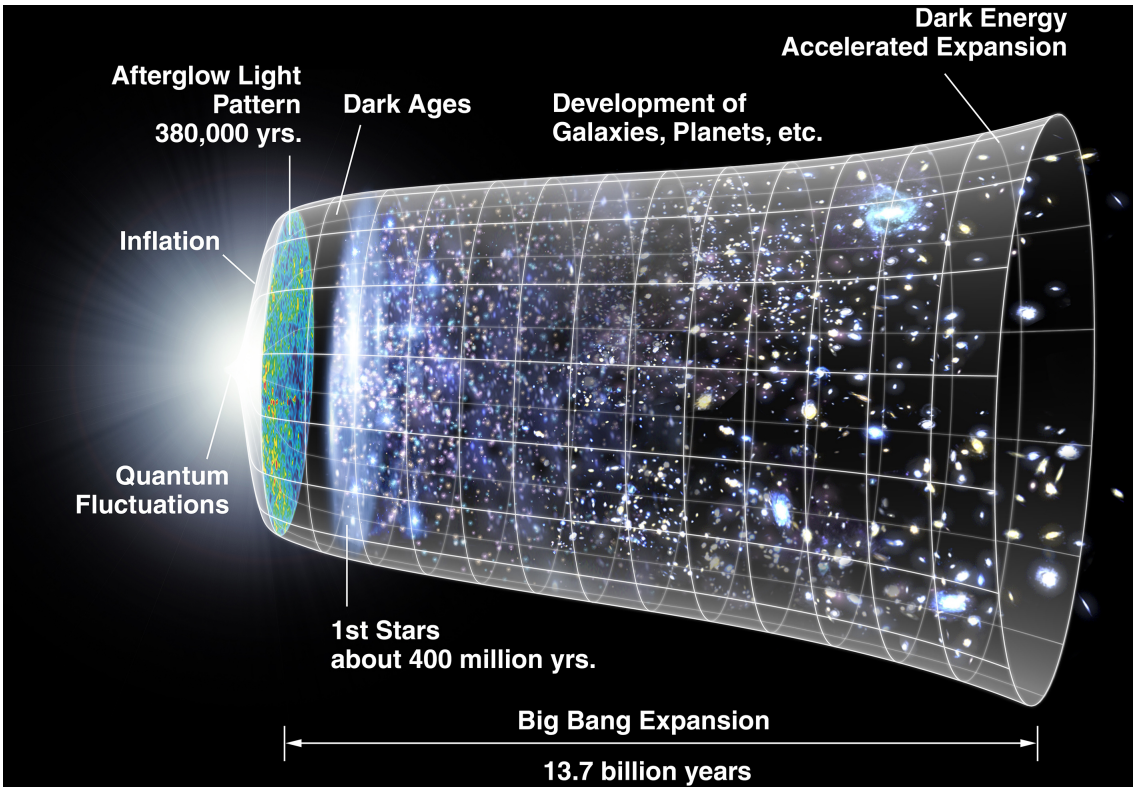

Figure 1.1: Schematic history of the universe including the inflationary epoch, the formation of the CMB, and the formation of galaxies. Image credit: WMAP team.

A detailed description of the modern cosmological model can be found in a number of books including [8] and [9]. We will present a summary of the most important results.

The modern cosmological model is predicated on the assumption that on the largest scales, the universe is *homogenous* and *isotropic*. These two terms have subtly different meanings. Here *homogenous* means that there is no preferred location in the universe and *isotropic* means that there is no preferred orientation. Within these constraints, the metric $g_{\mu\nu}$ must take a form known as the Freedman-Robertson-Walker (FRW) metric: [1]

$$g_{\mu\nu} = \begin{pmatrix} -1 & 0 & 0 & 0 \\ 0 & a(t) & 0 & 0 \\ 0 & 0 & a(t) & 0 \\ 0 & 0 & 0 & a(t) \end{pmatrix} \qquad x^{\mu} = \begin{pmatrix} t \\ x \\ y \\ z \end{pmatrix} \tag{1.1}$$

[1] For the rest of this section we will assume the absence of spatial curvature. Spatial curvature has been constrained by experimental measurements to constitute less than 0.3% normalized to the total energy in the universe, see [10]. Most textbooks including [8] show these equations without this assumption.

A single time-dependent scale factor $a(t)$ describes the expansion of space time and is in turn sourced by the matter and energy density of the universe. The Einstein field equations relate the metric to the matter and energy content of the universe following:

$$R_{\mu\nu} - \frac{1}{2}Rg_{\mu\nu} + \Lambda g_{\mu\nu} = 8\pi T_{\mu\nu} \tag{1.2}$$

where $R_{\mu\nu}$ is the Ricci curvature tensor consisting of derivatives of the metric, R is the Ricci curvature formed by contracting the Ricci tensor with the metric, and $T_{\mu\nu}$ is the stress-energy tensor. G and c (the gravitational constant and the speed of light) have been set to 1. In the absence of anisotropic stresses or bulk flows the stress-energy tensor takes the form:

$$T_{\mu\nu} = \begin{pmatrix} \rho & 0 & 0 & 0 \\ 0 & P & 0 & 0 \\ 0 & 0 & P & 0 \\ 0 & 0 & 0 & P \end{pmatrix} \tag{1.3}$$

where ρ represents the energy density and P represents isotropic pressure. The ratio between these is determined by the fractional energy density of radiation, matter, and dark energy.

The Einstein field equations as originally written contain a cosmological constant term denoted Λ. This was originally introduced to make the "steady state" cosmological model (i.e. $a(t) = \text{constant}$) mathematically viable, however later became unnecessary in an expanding universe. More recently, the cosmological constant has been re-introduced as a component of the stress-energy tensor called "dark energy" to explain the accelerating expansion of the universe observed in the brightness / redshift relation in Type 1a supernovae [11, 12].

In the FRW model the Einstein field equations reduce to two independent equations:

$$3\dot{a}^2/a^2 = 8\pi\rho, \tag{1.4}$$

$$3\ddot{a}/a = -4\pi(\rho + 3P). \tag{1.5}$$

The time derivative of the scale factor is known as the Hubble constant $H = \dot{a}/a$. There is a significant disagreement on the numerical value of the Hubble constant today. The Planck collaboration reports a value of $H_0 = 67.4 \pm 0.5 \text{kms}^{-1}\text{Mpc}^{-1}$ derived from the CMB and Baryon Acoustic Oscillations (BAO) [10] data. Local measurements report a value of $H_0 = 74.22 \pm 1.82 \text{kms}^{-1}\text{Mpc}^{-1}$, a nearly 5σ disagreement [13]. As of now there are no widely accepted explanations for this discrepancy.

The density corresponding to the current Hubble constant is known as the critical density:

$$\rho_{\text{cr}} = \frac{3}{8\pi}H_0^2. \tag{1.6}$$

It is conventional to normalize the density of matter and radiation to $\Omega^X = \rho_X/\rho_{\text{cr}}$. The current universe is dominated by matter and dark energy, with:

$$\Omega^{\text{matter}} = 0.311 \pm 0.006, \quad \Omega^{\Lambda} = 0.689 \pm 0.006, \quad \Omega^{\text{rad}} \approx 10^{-5}. \tag{1.7}$$

based on all Planck information and BAO data [10]. The majority of the matter density in the universe consists of dark matter that does not interact electromagnetically, or only does so weakly. The different forms of energy density scale with the scale factor $a(t)$ following:

$$\Omega^{\text{mat}} \propto a^{-3}, \quad \Omega^{\text{rad}} \propto a^{-4}, \quad \Omega^{\Lambda} \propto \text{constant}. \tag{1.8}$$

The universe has undergone three major epochs, beginning as radiation dominated, transitioning to matter dominated and then into the current dark energy dominated regime. This can be roughly inferred from the current values and the scaling laws of each component. In each regime, the scale factor $a(t)$ evolves following:

$$a(t)_{\text{rad dom}} \propto t^{1/2}, \quad a(t)_{\text{mat dom}} \propto t^{2/3}, \quad a(t)_{\Lambda \text{ dom}} \propto e^{Ht}. \tag{1.9}$$

This can be found by straightforward substitution into the FRW equations assuming $P = 0$ (matter), $P = \rho/3$ (radiation) and $P = -\rho$ (dark energy).

Often, instead of using t or $a(t)$ as an index for time, it is useful to work in terms of the redshifft z that relates the observed wavelength of a spectral feature to its emitted wavelength, $1+z = \lambda_{\text{obs}}/\lambda_{\text{emit}} = a_{\text{obs}}/a_{\text{emit}}$. The redshift is an experimentally useful quantity as it can be accurately determined by the apparent locations of spectral lines in the light from sources.

The period of radiation domination lasted for approximately the first 47,000 years after the Big Bang ($z \approx 3600$). This is somewhat before the surface of last scattering where the universe became transparent to light at approximately 380,000 years after the Big Bang ($z \approx 1100$). Matter dominated the energy density of the universe until the age of the universe reached approximately 9.8 billion years ($z \approx 0.3$) when the cosmological constant term took over.

1.2 Inflation

This section provides a brief overview of the theory of inflation including the motivation and basics of the single-field slow-roll model. Much more detailed descriptions can be found in several places including aforementioned references and the Particle Data Group inflation review [14].

The original Big Bang model posited that the early universe would be radiation dominated until arbitratily soon after the Big Bang. However, this assumption produces several subtle inconsistencies:

- **The flatness problem**: The universe today has a very small spatial curvature relative to the total energy density, i.e. $1 - \Omega_{\text{tot}} \ll 1$. Any initial spatial curvature will grow over the age of the universe (see Eq. 22.4 of the PDG review) meaning the early

universe must have been exponentially flatter. This poses a fine tuning problem as it requires the Hubble constant to precisely match the total energy density.

- **The horizon problem**: The cosmic microwave background is uniform to a few parts in 10^5, however the early universe was not small enough for long enough for regions separated by more than ~ 1 degree on the surface of last scattering to have been in thermal equlibrium. This poses yet another fine tuning problem.
- **The large scale structure seeding problem**: The power spectrum of anisotropies in the cosmic microwave background can be traced back to a nearly scale invariant spectrum of perturbations in the universe. Inflation provides a mechanism for the production of such perturbations.

The theory of inflation first proposed in the early 1980s by Andrei Linde, Alan Guth, and others [15, 16] offers a solution to all three of these problems simultaneously. The basic mechanism of inflation assumes an additional particle ϕ and associated potential $V(\phi)$ that dominated the total energy density in the early universe. Such an energy density term would remain approximately constant as the universe expanded.

Such a vacuum energy density has negative pressure in that expanding the volume of a closed system increases the internal energy. (There is an additional kinetic term proportional to $\dot{\phi}^2$ that will govern the dynamics as inflation unfolds. This will be discussed shortly.) In the limit that the energy density is constant (i.e. $\dot{\phi} \sim 0$) the Hubble constant H is also constant meaning the scale factor grows exponentially,

$$a \propto e^{Ht}. \tag{1.10}$$

This accelerating expansion solves the flatness problem by exponentially damping curvature. This can be seen by inspection of Eq. 22.4 in the PDG review in the limit that the the first and second time derivatives of the scale factor are both positive.

Additionally, the exponential expansion of the scale factor a during inflation can solve the horizon problem. To see this, transform the time unit t in the metric to conformal time η defined as:

$$\eta = \int \frac{dt}{a(t)}. \tag{1.11}$$

In these units null geodesics (i.e. the path of light rays) are diagonal in the η, x plane. The distance traveled by a light ray from time t_1 to t_2 can therefore be given by:

$$\eta = \int_{t_1}^{t_2} \frac{dt}{a(t)} \rightarrow \int_{t_1}^{t2} dt\ a(t_2)\ e^{-Ht} \tag{1.12}$$

which becomes unbounded as $t_1 \rightarrow -\infty$. In contrast, in a radiation-dominated universe this equation becomes

$$\eta = \int_{t_1}^{t_2} \frac{dt}{a(t)} \rightarrow \int_{t_1}^{t_2} dt\ t^{-1/2} \tag{1.13}$$

which is finite as $t_1 \rightarrow 0$. The need for the entire CMB to be in causal contact places a lower limit on the necessary expansion of the universe during the inflationary period that is $N \sim 40 - 60$ e-folds depending on the energy scale of $V(\phi)$.

There is an additional requirement that theories of inflation must satisfy - the period of inflation must come to an end. To satisfy this condition it is necessary to look beyond the approximation that V is constant and consider the $\dot{\phi}$ term. The evolution of the inflation field ϕ is governed by the equation

$$\ddot{\phi} = -3H\dot{\phi} - V'(\phi) \tag{1.14}$$

which is mathematically analogous to the equation of motion for a block sliding down a slope with the Hubble constant H forming the kinetic friction term. Such a slowly decaying potential gives rise to an imperfect scale invariance in the primordial fluctuations. It is conventional to define two terms based on the shape of the potential $V(\phi)$ that are known as the slow roll parameters

$$\epsilon = \frac{M_p^2}{16\pi}\left(\frac{V'}{V}\right)^2 \tag{1.15}$$

$$\eta = \frac{M_p^2}{8\pi}\left(\frac{V''}{V}\right) \tag{1.16}$$

where M_p is the reduced Planck mass. Both ϵ and η are dimensionless and must be $\ll 1$ for the slow roll approximation to hold. These slow roll parameters are related to the spectral shape of primordial perturbations.

1.3 Scalar and tensor perturbations

The inflationary paradigm provides a seed for the formation of large scale structure via quantum fluctuations in the inflaton field. Inflation is expected to source two types of perturbations, scalar (density) and tensor (gravitational wave) perturbations. The initial perturbations are expected to be nearly scale invariant and Gaussian.

The inflation slow roll parameters can be seen in several observable quantities in the CMB power spectra. The first is the slight scale invariance in the power spectrum of primordial scalar fluctuations $P(k)$ parameterized by n_s,

$$n_s - 1 = \frac{d\ln P(k)}{d\ln k} \approx -6\epsilon + 2\eta \tag{1.17}$$

Current measurements detect this slight scale invariance at high significance with the Planck 2018 constraint being $n_s = 0.965 \pm 0.004$. A second order scale invariance of n_s known as the running of the scalar spectral index has not been detected in current data.

In addition to scalar perturbations inflation is expected to produce a background of tensor perturbations. Gravitational waves appear in the metric as an alternating compression and stretching of space along the two directions perpendicular to the direction of propagation. This can be written for a wave propagating in the $\hat{z}$ direction

$$\Delta g_{\mu\nu} \propto (\epsilon_\times h^{\mu\nu}_\times + \epsilon_+ h^{\mu\nu}_+) e^{i(kz-\omega t)} \tag{1.18}$$

$$h^{\mu\nu}_\times = \begin{pmatrix} 0 & 0 & 0 & 0 \\ 0 & 0 & 1 & 0 \\ 0 & 1 & 0 & 0 \\ 0 & 0 & 0 & 0 \end{pmatrix} \quad h^{\mu\nu}_+ = \begin{pmatrix} 0 & 0 & 0 & 0 \\ 0 & 1 & 0 & 0 \\ 0 & 0 & -1 & 0 \\ 0 & 0 & 0 & 0 \end{pmatrix} \tag{1.19}$$

where $\omega/k = c$ is the speed of propagation. Theories of inflation generically predict the existence of primordial tensor perturbations with the overall amplitude described by a parameter

$$r = \frac{P_{\rm tensor}(k^*)}{P_{\rm scalar}(k^*)} \approx 16\epsilon, \tag{1.20}$$

where k^* is an aribtrary pivot scale conventionally taken to be $k^* = 0.05$ Mpc^{-1}. The tensor spectrum will not be exactly scale invariant and can be described by a similar spectral index

$$n_t = -\frac{r}{8}. \tag{1.21}$$

However, if the value of r is sufficiently small a detection of non-zero n_t may be outside the reach of CMB experiments.

1.4 CMB power spectra

The primary CMB anisotropies (neglecting the impact of weak gravitational lensing and foregrounds, which will be discussed in Section 1.5 and Chapter 10 respectively) are a Gaussian random field. It is conventional to decompose the CMB temperature field $T(\hat{n})$ into the spherical harmonic basis set:

$$T(\hat{n}) = \sum_\ell \sum_{-\ell \le m \le \ell} a_{\ell m} Y^m_\ell(\hat{n}) \tag{1.22}$$

with the power spectrum

$$C_\ell = \frac{1}{2\ell+1} \sum_{-\ell \le m \le \ell} a^*_{\ell m} a_{\ell m}. \tag{1.23}$$

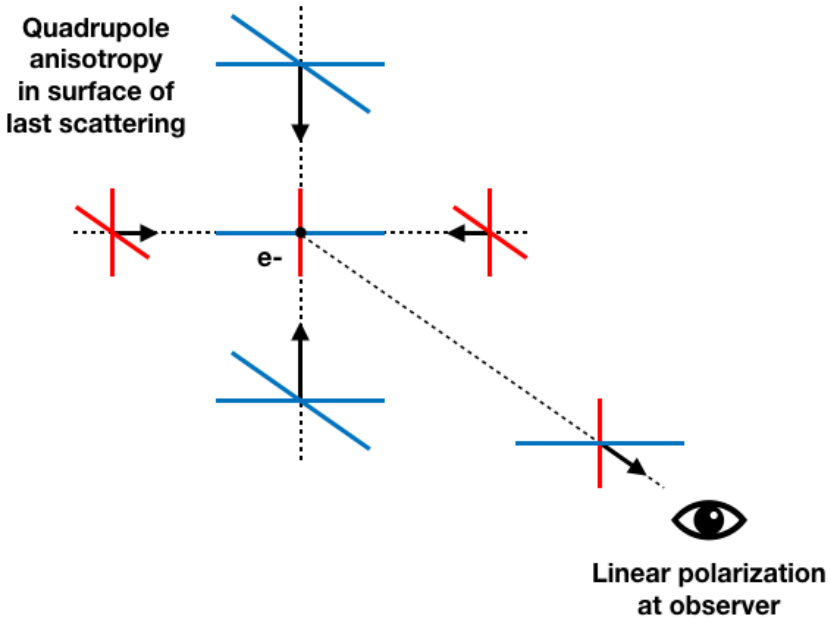

Figure 1.2: Formation of polarization in the CMB due to quadrupole anisotropies in the surface of last scattering.

The CMB anisotropies are polarized at the $\sim 10\%$ level. This polarization is produced by the polarization dependence of the Thompson scattering cross section and local quadrupole anisotropies in the surface of last scattering. This is shown schematically in Figure 1.2.

The temperature anisotropies of the CMB form a scalar field meaning simply that the value of the CMB temperature at any point on the sky is a scalar. The polarization signal, however, contains two independent pieces of information at every point: an amplitude and an orientation. This basis is impractical for most calculations so instead the polarization is conventionally written in terms of the Stokes parameters

$$Q = \langle E_x^2 \rangle - \langle E_y^2 \rangle \quad U = \langle E_a^2 \rangle - \langle E_b^2 \rangle \tag{1.24}$$

where the coordinate systems denoted $(\hat{x}, \hat{y})$ and $(\hat{a}, \hat{b})$ are rotated at 45° with respect to each other. The complex combination $Q + iU$ forms a spin-2 field in that the quantity transforms as

$$(Q + iU) \rightarrow e^{2i\theta}(Q + iU) \tag{1.25}$$

under a rotation of the coordinate system by θ. It is conventional to define two scalar quantities from this polarization field called E and B modes. A full-sky derivation can be found in [17] using the full spin spherical harmonic formalism. In this thesis we will focus on

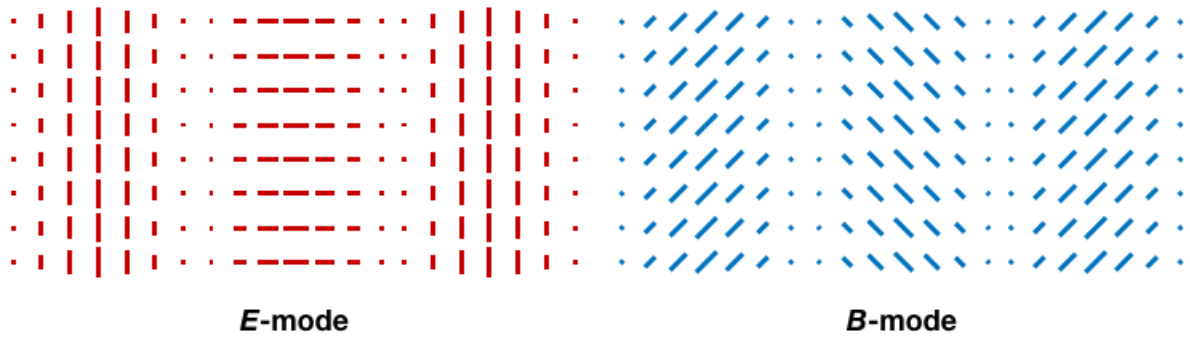

Figure 1.3: Illustration of Fourier E and B modes.

the simpler and more intuitive flat sky definitions. An accessible introduction including the connection between the curved and flat sky formalisms can be found in [18]. The flat-sky approximation can only be used in place of the full spherical harmonic expansion on small patches of sky.

Taking a Fourier transform of the $Q(\vec{x})$ and $U(\vec{x})$ fields yields their Fourier components

$$Q(\vec{\ell}) = \int \frac{d\vec{x}}{(2\pi)^2}\, Q(\vec{x})\, e^{-i\vec{\ell}\cdot\vec{x}} \quad U(\vec{\ell}) = \int \frac{d\vec{x}}{(2\pi)^2}\, U(\vec{x})\, e^{-i\vec{\ell}\cdot\vec{x}} \tag{1.26}$$

which are then combined to form E and B Fourier modes

$$E(\vec{\ell}) = \frac{1}{\sqrt{2}}\Big(\; Q(\vec{\ell})\cos(2\phi_\ell) + U(\vec{\ell})\sin(2\phi_\ell)\Big) \tag{1.27}$$

$$B(\vec{\ell}) = \frac{1}{\sqrt{2}}\Big(-Q(\vec{\ell})\sin(2\phi_\ell) + U(\vec{\ell})\cos(2\phi_\ell)\Big) \tag{1.28}$$

where ϕ_ℓ is the angle between $\vec{\ell}$ and the coordinate axes. A schematic diagram of E and B Fourier modes can be found in Figure 1.3. Under a parity inversion of the sky B modes will acquire a negative sign but E modes will not.

The flat-sky power spectra can be written similarly to the full-sky counterparts:

$$C_\ell = \langle X(\vec{\ell})Y^*(\vec{\ell})\rangle \tag{1.29}$$

for $X, Y \in \{E, B\}$ where in practice this is a sum over quantized Fourier modes binned azimuthally. It is often convenient to define a rescaled version of C_ℓ:

$$D_\ell = \ell(\ell+1)/2\pi\; C_\ell. \tag{1.30}$$

It is possible to construct six unique spectra from temperature, E mode and B mode polarization called TT, TE, TB, EE, EB and BB. The two even-odd parity combinations of modes are generally assumed to be zero due to parity (under a global mirror image the

spectrum $EB \to -EB$ and $TB \to -TB$ therefore a non-zero value of these spectra implies a global parity violation in the universe) meaning the primary CMB anisotropies are uniquely defined by four sets of numbers.

The E-mode polarization pattern in the CMB is sourced by both scalar (density) and tensor (gravitational wave) perturbations in the early universe. In contrast, primary B mode polarization is only sourced by tensor perturbations providing a clean channel to potentially detect inflationary gravitational waves.

The precision with which a power spectrum can be measured is fundamentally limited by sample variance, or the fact that the power spectrum is estimated using a finite number of modes. This takes the form

$$\Delta C_{\ell,\mathrm{min}} = \sqrt{\frac{2}{(2\ell+1)f_{\mathrm{sky}}}}\, C_\ell. \tag{1.31}$$

The uncertainty on the power spectrum is proportional to the power spectrum itself. Here f_{sky} is the fractional area on the sky where the signal can be reliably measured and is generically less than 1 due to Galactic foregrounds. The lack of additional power due to scalar perturbations means that B-modes can place a tighter limit on r than the brighter temperature and E-mode polarization.

1.5 Gravitational lensing

In reality the observed CMB is not a perfect Gaussian field due to the impact of gravitational lensing. A detailed and thorough derivation of the physics of gravitational lensing can be found in [19] and a more accessible description can be found in [20]. Gravitational lensing remaps the apparent position of the CMB anisotropies according to a deflection field $\vec{d}$

$$\{I, Q, U\}(\vec{x}) \to \{I, Q, U\}(\vec{x} + \vec{d}) \tag{1.32}$$

The deflection field is expected to have zero curl at first order and can be written as the gradient of a potential $\vec{d} = \vec{\nabla}\phi$. The potential ϕ is given by the weighted integral of density along the line of sight to the surface of last scattering. The value of the lensing field $\vec{d}$ is typically a few arcminutes, $\mathrm{rms}(d) \approx 2.6$ amin with coherent structure on the scale of a few degrees.

At high enough sensitivity the B-modes produced by gravitational lensing become an important foreground that must be accounted for in r constraints. The level at which this can be removed in practice is an outstanding research problem.

1.6 The current state of CMB measurements

A composite plot the the four non-zero CMB spectra and the lensing potential spectrum can be found in Figure 1.4.

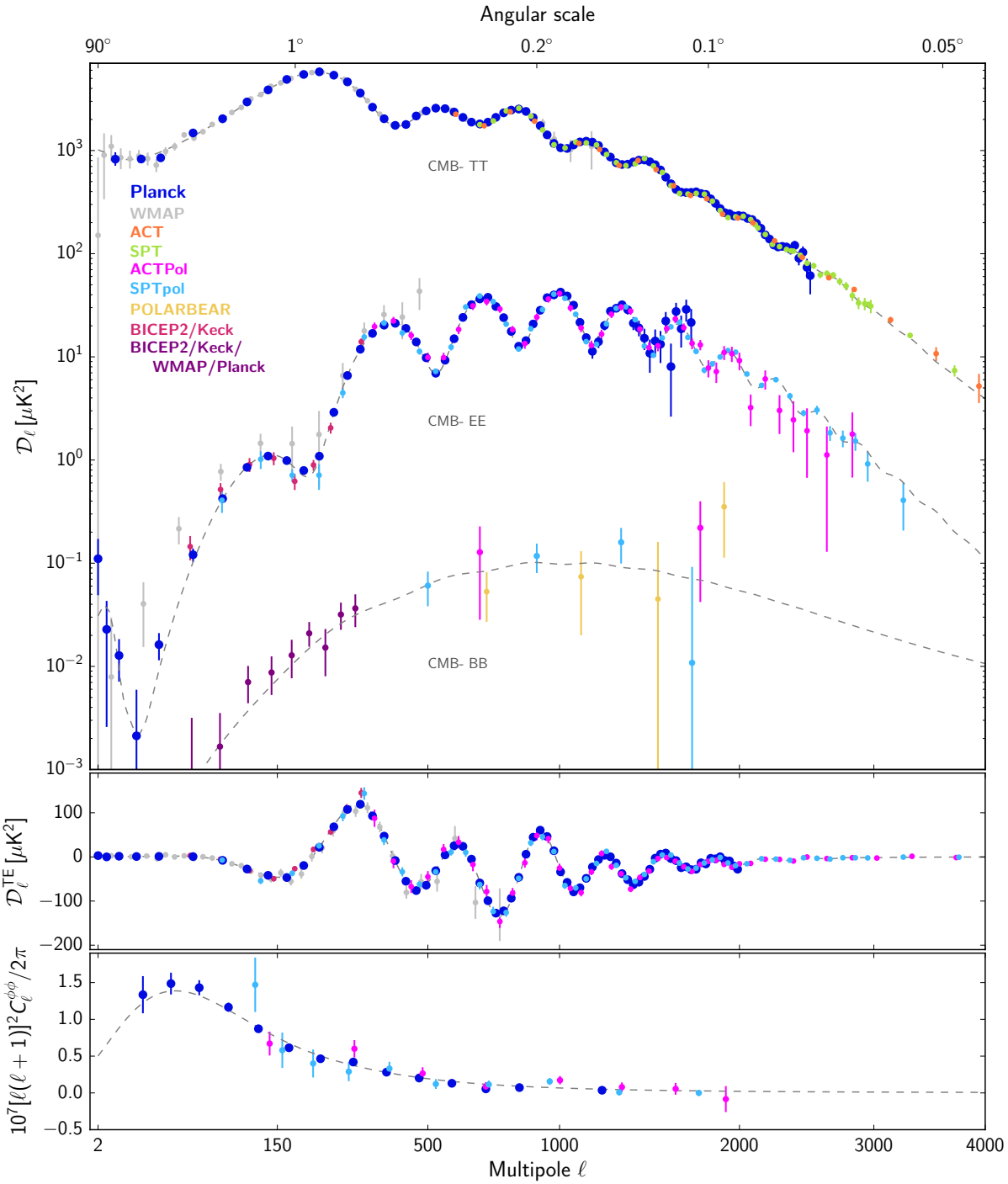

Figure 1.4: Composite image of all measured CMB power spectra. This thesis presents a new measurement of the B-mode spectrum at low ℓ. Image credit: Planck team.

The temperature anisotropies of the CMB were first measured by the differential microwave radiometer on the COBE satellite [21]. The first acoustic peak in temperature was seen by the the balloon-based experiments MAXIMA and BOOMERanG over the course of several flights which established the flatness of the universe [22] via the location of the first CMB acoustic peak and confirmed the recently discovered acceleration in the expansion of the universe from Type 1a supernovae [11, 12]. Several years later WMAP observed the first and second acoustic peaks in the CMB temperature power spectrum and further tightened constraints on the ΛCDM cosmological parameters [23].

The CMB E-mode spectrum was first observed by the DASI experiment [24] located at the South Pole. The current best constraints on the E-mode spectrum come from the Planck collaboration at low-ℓ [3]. The best constraints on the high-ℓ E-mode spectrum come from ACT [25] and SPT [26] .

This B-mode signal has been measured in several independent means. Several indirect methods have been used wherein a template for the gravitational lensing is constructed from an independent tracer such as the cosmic infrared background (CIB) [27] or using the CMB anisotropies themselves [28]. This can be used to estimate the B-mode power either independently or in cross correlation with maps of the CMB polarization.

A measurement of the B-mode power spectrum from CMB polarization alone was first reported by the POLARBEAR collaboration in [27]. Subsequent direct measurements of B-mode polarization have been reported by POLARBEAR [29], BICEP2 [30], *Keck Array* [31], SPTpol [32], and ACTPOL [25].

To robustly constrain the tensor to scalar ratio r experiments must cross correlate CMB data with higher and lower frequencies to control for galactic foreground contamination. Such cross correlation analyses have been presented by the BICEP2 and *Keck Array* collaboration [33, 34] and the ABS collaboration [35]. This thesis will present such an analysis using three seasons of POLARBEAR data.

Chapter 2

The POLARBEAR Instrument

This chapter describes the POLARBEAR instrument as well as the observation strategy used in this work.

2.1 The POLARBEAR telescope and receiver

The POLARBEAR experiment is installed on the Huan Tran Telescope (HTT) at 5,190 m on the side of Cerro Toco in the Atacama desert of northern Chile. The dry high-altitude site provides excellent observing conditions in the millimeter wavelengths for most of the year. The mid-latitude location provides access to appriximately 80% of the sky and can be used to create robust parallactic angle coverage and cross linking in CMB maps. This will be described in Section 2.4. More details about the Huan Tran Telescope and the POLARBEAR receiver can be found in [36] and [37]. A brief overview is provided here for completeness.

The HTT is an off-axis Gregorian-Dragone design. The off-axis design avoids occluding the optical path with support members that would generate spurious instrumental polarization from unpolarized incident light. The Huan Tran telescope design satisfies the Mizugutchi-Dragone (MD) condition that minimizes cross polarization and aberration. The MD condition is described in [38, 39] and the specific design of the Huan Tran Telescope is described in [40]. The primary mirror consists of a monotlithic 2.5 m precision machined aluminum mirror surrounded by a guard ring that extends out to 3.5 m diameter. The 2.5 m mirror forms 3.5 amin full width at half max (FWHM) beam on the sky allowing the instrument to measure angular scales down to $\ell \approx 3000$.

The POLARBEAR experiment is a cryogenic millimeter wave receiver installed in the boom of the HTT. The receiver consists of three interrelated subsystems: the lenses and optical components used to focus incident light and reduce thermal load from out-of-band radiation known collectively as the optics tube, the cryogenic array of polarization-sensitive detectors that transform the incident light into electrical signals known as the focal plane, and the electronics that amplify and digitize these signals to form time ordered data (TOD) referred to as the readout. A diagram of the receiver and its location in the HTT is shown

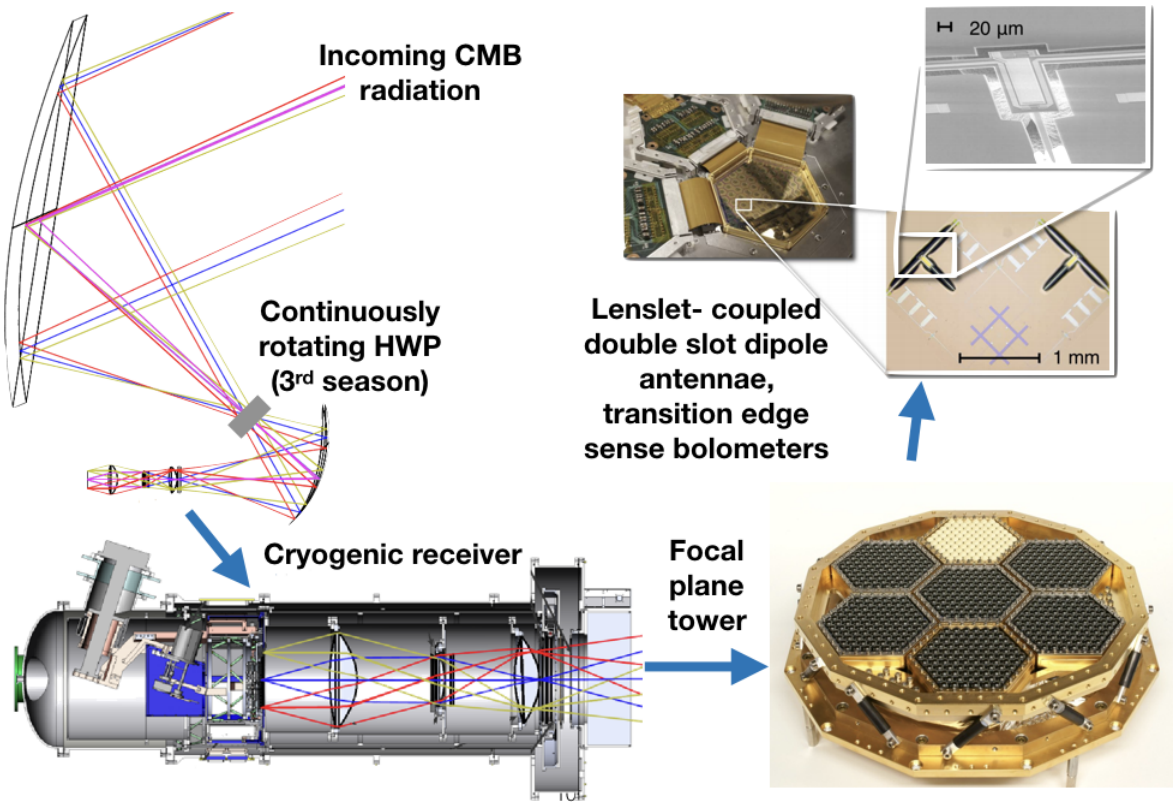

Figure 2.1: Schematic diagram of the POLARBEAR receiver including optical path, focal plant tower and microfabricated antennae and TES bolometers.

in Figure 2.1.

The optics tube consists of several components to focus the sky signal on to the focal plane, minimize excess optical power on the detectors due to elements in the optical path, and minimize thermal load on the cryogenic components from out-of-band radiation. Closest to the secondary, a foam window is used to maintain vacuum and cryogenic temperatures inside the optics tube while being transparent to microwave radiation. Immediately behind this is a series of IR blocking filters to reduce thermal load from high frequencies and an 80 K stepped cryogenic half-wave plate (CHWP). The CHWP is designed to produce an additional supression of beam systematics in the final power spectrum in addition to what is produced naturally by sky rotation by rotating the detector polarization angles on the sky. This is similar but not equivalent to the "deck angle" rotation employed by the Simons Observatory small aperture telescopes and the BICEP / *Keck Array* experiments in that the detector polarization angles are rotated but the orientation of the focal plane on the sky remains constant. The CHWP was moved frequently during the first two seasons, however was not moved for the data set that this work is based on. Behind the CHWP and IR filters there are three anti-reflection coated reimaging lenses and a beam forming Lyot stop.

The focal plane consists of an array of 637 polarization sensitive pixels split between seven wafer assemblies held at 270 mK by a Simon Chase (`http://www.chasecryogenics.com/`) "He10" fridge backed by a pulse tube cooler. Under normal conditions the temperature of the focal plane can be maintained for $30-40$ hours before the cryogens in the "He10" fridge must be recycled. Each pixel consists of an anti-reflection coated silicon lenslet focusing incoming light onto a double-slot dipole antenna. Signals from the antenna are routed through band defining filters on the detector wafer and deposited on a thermally isolated island containing a transition edge sense (TES) bolometer.

The bolometers are an AC voltage biased. The voltage bias creates negative electrothermal feedback that compensates for changing optical load with an opposite change in power dissipated resistively thereby suspending the bolometer in the superconducting transition.

Individually reading out the array of 1274 bolometers would place a prohibitive heat load on the cryogenic stages due to wire count. As a result, we use a frequency domain multiplexing scheme to minimize the number of cables required between the ambient temperature and cryogenic stages. More details on the implementation can be found in [41]. Each bolometer is wired in series to an LC resonator at a specific frequency. Varying the bolometer resistance modulates the height of the RLC resonant peak which is amplified by a superconducting quantum interference device (SQUID). The inductors and capacitors are packaged directly behind the detector wafers to minimize unused space on the focal plane. Eight channels are read out on a single set of cables.

The signals from the SQUID amplifiers are amplified, demodulated, and digitized at a sample rate of 190 Hz. This is significantly downsampled for the final science analysis.

In addition to the optical channels, 238 channels consisting of resistors and bolometers not connected to antennae ("dark bolometers") are read out for diagnostic purposes. The signal in these dark bolometers is generally dominated by electrical crosstalk from the optical bolometers.

The POLARBEAR experiment deployed to Cedar Flat in the Inyo Mountains of southern California for an engineering run in 2010. In 2011 the experiment was moved to its current location in the Atacama Desert. First light in Chile occured on 10 January 2012.

2.2 Small patch observations

For the first two seasons of operations, the POLARBEAR experiment observed three $3^\circ \times 3^\circ$ patches of sky focusing on the sub-degree scale B-mode power spectrum and lensing science. The three patches are located in low-foreground regions of the sky referred to as RA4.5, RA12, and RA23 after their right ascension coordinates. These three patches reached effective map depths of 7, 6, and 5 μK-amin respectively after two seasons of observations.

After the first season, POLARBEAR published results showing the first direct detection of B-mode power in the CMB auto spectrum [42], a measurement of the lensing power spectrum [43] from four point estimators, and a measurement of CMB lensing in cross correlation with the cosmic infrared background [27].

Additionally, we have used this data set to constrain primordial magnetic fields and anisotropic cosmic birefringence [44], model the atmospheric fluctuations above the POLARBEAR site [45] and develop a new mapmaking algorithm [46] that corrects the bias introduced by TOD filtering on a mode by mode basis.

After the second season of observations POLARBEAR published a deeper B-mode power spectrum estimate [47] as well as cross correlation analyses between the POLARBEAR lensing estimate and the Hyper Suprime Camera on the Subaru telescope [48] and the Herschel-ATLAS galaxy survey [49]. A four point analysis and a demonstration of internal CMB delensing are in preparation.

These data differ one critical way from the main analysis of this thesis. The polarization signal is recovered by directly differencing the two bolometers in a pixel pair (called "top" and "bottom" based on the on-chip interconnects):

$$d_t(t) \sim \langle {E_x}^2 \rangle = \frac{1}{2}(I+Q) \quad d_b(t) \sim \langle {E_y}^2 \rangle = \frac{1}{2}(I-Q) \tag{2.1}$$

$$d_p(t) = d_t(t) - d_b(t) \sim Q \tag{2.2}$$

In this paradigm the measured polarization signal can be contaminated by detector mismatch within the pair, including differential pointing, differential gain, differential ellipticity, differential non-linearity, etc. A detailed review of these effects can be found in [50] and a mitigation strategy has been demonstrated in [51] based on fitting for and deprojecting leakage from beam mismatch. POLARBEAR analyses have found these effects to be subdominant to our statistical errors, however the scale of contamination depends on many parameters of the measurement including the details of the instrument design and observing strategy.

In February 2014, around the time of a claim [30] of a detection of degree-scale B-mode power in the CMB corresponding to primordial gravitational waves with $r \approx 0.2$, POLARBEAR switched observation modes to pursue the degree-scale B-mode power spectrum. This entailed two major changes to the observation strategy that will be described in subsequent sections: adding an ambient temperature continuously rotating half-wave plate (CRHWP) and moving to scans on a broader patch of sky.

2.3 The ambient temperature half-wave plate

The POLARBEAR collaboration installed the CRHWP in the HTT in April of 2014. The CRHWP consists of an anti-reflection coated birefringent single crystal sapphire plate. The CRHWP is installed at the focus of the primary mirror due to limitations on sapphire crystal sizes available. More details about the installation and performance of the CRHWP can be found in [52]. Science observations with the CRHWP began on 14 May 2014, however data before 25 July 2014 was not used in the final results due to a change in the CRHWP angle reconstruction.

2.4 The PB700 scan strategy

Observations in the final configuration used for these results began on 25 July 2014 and continued until 7 January 2017. The data set is broken up into three seasons referred to as Season 3, 4, and 5 spanning 14 July 2014 —1 March 2015, 2 March 2015 —31 December 2015, and 1 January 2016 —30 December 2016, respectively. The seasons are separated by periods of instrument downtime due to external conditions and mechanical problems.

The POLARBEAR large patch scan was designed to overlap with BICEP/Keck observations [30] and targets a 700 square degree area centered on (RA, Dec)=$(+0^{\mathrm{h}}12^{\mathrm{m}}0^{\mathrm{s}}, -59°18')$. The scan strategy differs significantly from previous observations. Rather than specifically tracking a point as it moves across the sky, the schedule follows a fixed routine locked to local sidereal time (LST). The patch is located far below the ecliptic equator meaning that we do not need to modify the schedule to avoid the sun or moon coming close to the telescope boresight.

The scan strategy consists of three sets of constant elevation scans (CESs) repeated every sidereal day. We scan for a 4 hour 45 minute block as the CMB patch rises above the horizon, a 3 hour 53 minute block at high elevation as the patch transits, and a 4 hour 45 minute block as the CMB patch sets. The rising and setting scan occur at a boresight elevation of 30° and 35.°2 respectively. The difference between the two scans is purely historical. The elevation of the high elevation scan is stepped through ten offsets from 45.°5 to 65.°5 to provide even coverage of the patch. The range of the offsets is set by the patch width in declination and the spacing between offsets is set by the angular footprint of the focal plane on the sky ($\sim 2.°4$). As a result of the ten distinct high elevation scans, a complete map of the field is produced once every ten days. Several of these ten day cycles are combined in post-processing due to low weight or incomplete coverage after data selection. This combination results in 38 approximately even splits of the data set. These splits form the basis for the cross spectra used in the power spectrum estimation described in Section 4.5. The total map weight is shown in Figure 2.2. The overall gradient in depth approaching the bottom edge of the patch is a natural consequence of the geometry of Chilean scans. Near the southern celestial pole the sky moves slowly meaning the detector weight is concentrated in a smaller space in the right ascension direction. The deepest portion of the patch reaches 16 μK-arcmin before correction for data filtering and the beam window function.

Each observation block is broken into hour-long CESs after which the detectors are retuned and a quick relative gain calibration is performed. This calibration is described in more detail in 3. The length of the uninterrupted CESs is a critical parameter of the observation strategy. This length is bounded from below by the need to orthogonalize signals fixed on the sky with structure fixed in the ground frame. Heuristically, the sky must move by $\sim \theta$ during the course of a CES observation to differentiate ground fixed and sky fixed modes with angular scale θ. An hour corresponds roughly to the knee at which sky signals with $\ell \approx 100$ can be differentiated from the ground. The length of the CESs is bounded above by effeciency losses due to latched or saturated bolometers caused by slowly varying atmospheric and cryogenic conditions.

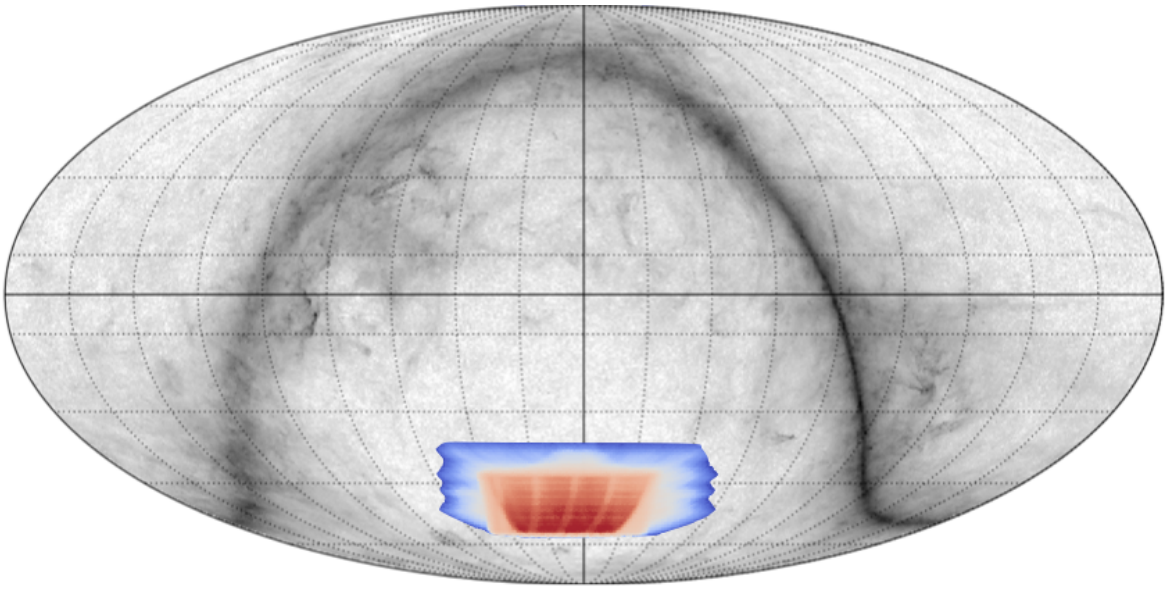

Figure 2.2: Map coverage illustrating the scan pattern where red corresponds to the deepest core and blue corresponds to the low weight edges). The deepest part of the map reaches 16 μK-arcmin in polarization. The vertical stripes are an artifact of breaks in the low elevation scans to retune the detectors and prform the relative gain calibration. The horizontal stripes are an artifact of the elevation offsets used in the transit scan. The patch is overlaid on the Planck 353 GHz intensity map to show the structure of Galactic emission.

There is no reason the telescope cannot be repointed between hour long CESs, however this degree of freedom is not used in this scan strategy. The strategy can be improved by reducing wasted time in the high elevation scans as the telescope covers low weight regions.

During scans, the telescope is slewed at a constant velocity of $0.^{\circ}4$ s^{-1} with a throw of 20° and 35° on the sky for the low elevation and high elevation scans, respectively. This results in approximately 70 subscans (defined as one left going or right going motion of the telescope) in each hour long CES. The scan speed is set by the requirement that modes with angular scale $\ell \leq 3000$ (the practical upper limit given the POLARBEAR beam size) map to a temporal bandwidth of 4 Hz (set by twice the CRHWP speed for reasons that will be discussed at length later). There is some evidence that increasing the scan speed will result in low frequency noise in the time domain mapping to lower ℓ values in the maps resulting in improved sensitivity to inflationary angular scales. This will be discussed in 5.

Data are discarded from two blocks of time due to mechanical problems with the weatherproof enclosure of the CRHWP and the eruption of a nearby volcano on 30 October 2015. Additionally, the thermal source used for relative gain calibration was replaced several times due to mechanical problems including water ingress.

When the science patch is not available, we recycle the "He10" fridge cryogens and preform beam, pointing and polarization angle calibrations. This is described in further detail in

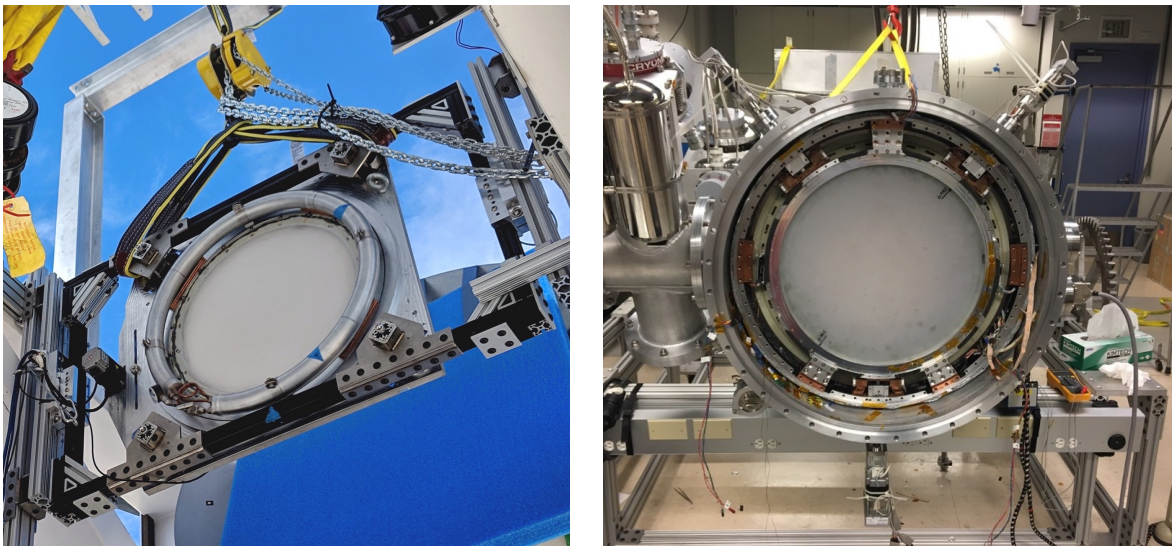

Figure 2.3: The POLARBEAR-2a and POLARBEAR-2b CRHWPs. Picture credit: Shawn Beckman (left) Charles Hill (right).

Chapter 3. For most of the data set, the fridge was cycled every 24 sidereal hours; however starting in October of 2015, the fridge cycle was done every 48 sidereal hours to provide time to scan the small patch referred to as RA12. The resulting observing efficiency on this patch was low and the map depth from this time period is not competitive with the first two seasons of observations.

POLARBEAR-2 and the Simons Array

The POLARBEAR collaboration is building on the results of POLARBEAR with three new telescopes collectively named the Simons Array. POLARBEAR-2a and POLARBEAR-2b are dichroic receivers observing at 90 GHz and 150 GHz simultaneously using lenslet-coupled sinuous antennae [53]. The sinuous antennae are used in place of the double-slot dipoles in POLARBEAR for their broad frequency bandwidth due to the scale invariance of the sinuous design. POLARBEAR-2c will serve as a high frequency foreground monitor observing at 220 GHz and 270 GHz. Each receiver will have 7,588 bolometers split between its two frequency bands. The detectors are read out using a similar frequency domain multiplexing system as POLARBEAR with a higher multiplexing factor (40 versus 8 for POLARBEAR).

Like POLARBEAR, the Simons Array telescopes will all use a CRHWP for control of low frequency noise. The POLARBEAR-2a CRHWP will be located at the focus of the secondary mirror and at ambient temperature. The POLARBEAR-2b and POLARBEAR-2c CRHWPs will be installed in the receiver cryostat and spun on a superconducting magnetic bearing. The CRHWPs for the Simons Array are thicker than the POLARBEAR CRHWP due to their broadband design. Moving the CRHWP to cryogenic temperatures will significantly mitigate

Figure 2.4: The POLARBEAR2 and Simons Array telescopes installed in Chile. The telescopes are, going front to back, POLARBEAR-2a, POLARBEAR soon to be retrofit to become POLARBEAR-2c, and POLARBEAR-2b.

excess optical loading and therefore noise on the bolometers.

Scan strategies for future instruments

The subject of the optimal observation strategy from Chile is an open problem that is currently being explored [54]. At the South Pole the zenith and the southern celestial pole (nearly) exactly align meaning the sky rotates in azimuth only. The sun never reaches above 22° above the horizon meaning a high-elevation patch is free from sun intrusion. The situation for Chilean experiments is somewhat more complicated. As a general heuristic, it is straightforward to create a scan strategy that fulfills any two of the following three objectives:

1. Spend the majority of observations at high elevation to avoid excess atmospheric loading and mechanical complications with ground shields
2. Focus sensitivity on a small patch of sky
3. Acheive a high calendar efficiency, i.e. fill close to 24 hours every day with observations

In the PB700 scan strategy we chose to optimize for only the final two goals. The Simons Observatory small aperture telescopes are much more tightly constrained by observing ele-

vation requirements than POLARBEAR meaning the resulting scan strategies look somewhat different. Proposed scan strategies for the Simons Observatory are designed to be robust to the Sun and moon entering the science patches, however some efficiency hits are unavoidable due to the geometry of the problem.

It should also be noted that the optimal sky area for r searches is by no means a straightforward calculation. Here I will present a qualitative argument while differing a detailed discussion of power spectrum uncertanties to Chapter 4. The uncertainty on a measured power spectrum can be written following

$$\Delta C_\ell \approx \sqrt{\frac{2}{(2\ell+1)\Delta\ell f_{\rm sky}}}\left(C_\ell + \frac{N_\ell}{B_\ell^2}\right) \tag{2.3}$$

where N_ℓ is the noise power spectrum, B_ℓ is the Fourier transform of the beam window function, and $f_{\rm sky}$ is the fraction of the sky observed. This equation is approximate in that it does not account for the impact of TOD filtering, mode mixing, or the fact that the effective number of degrees of freedom (equivalently the effective $f_{\rm sky}$) differs between signal and noise for anisotropic map depths.

For a fixed instrument and integration time, the noise bias and the $f_{\rm sky}$ are inversely proportional neglecting efficiency prefactors that will be partially determined by scan strategy,

$$N_\ell \propto f_{\rm sky}. \tag{2.4}$$

By inspection of the Knox formula, the optimal uncertainties are acheived when $C_\ell \sim N_\ell/B_\ell^2$, or when an experiment reaches signal-to-noise of ~ 1 on individual modes. Applied to an r constraint this means that the sky area should be maximized such that the noise power spectrum N_ℓ is subdominant to the lensing B-mode spectrum or the level of residuals after delensing, C_ℓ. In other words, more effective delensing and foreground control drives experiments toward smaller sky patches to constrain r. The optimal strategy is an active area of research.

It can also be argued that the Knox formula intuition does not capture the complete picture as larger sky areas sampling independent foreground realizations can build an additional layer of immunity to complicated features of dust or synchrotron emission.

Chapter 3

Calibration and Data Processing

This chapter describes the steps taken to generate the inputs to our data analysis pipelines. As the data are unpacked we record dropped data packets that are later flagged in the data selection. At this stage we reconstruct the CRHWP angle and interpolate this to match the bolometer readout time stamps. Some level of care needs to be applied to the CRHWP angle reconstruction as errors couple directly into the polarization measurement via the CRHWP synchronous signal. This is descriped in 4.3.

3.1 Beam window functions

Following the previous POLARBEAR small patch science analyses, the instrument beam (i.e. the point spread function) and the associated window function B_ℓ (the azimuthally averaged Fourier transform of the beam) are measured using dedicated raster observations of Jupiter. We take Jupiter observations with the HWP rotating nominally at 2 Hz at a scan speed of $0.^\circ 2$ s^{-1} on the sky. This allows us to reconstruct the beam using the temperature channel as well as check for temperature to polarization leakage systematics as described in [55]. A description of the polarization response to Jupiter can be found in [56]. The HWP synchronous structure is subtracted by masking off a $25'$ disk centered on Jupiter and fitting a first order polynomial to the time dependent amplitude of each HWP harmonic $n \in \{1...7\}$. The time ordered data (TOD) is downsampled to 64 Hz (in contrast to the science data, which is sampled at 8 Hz) to avoid aliasing between the TOD sample rate and the map pixel size and supression of power at high ℓ due to the window function of the TOD sample rate. After the CRHWP synchronous structure is subtracted the TOD are projected into $0.'5$ pixels on the sky. The beam window function is taken to be the average of the azimuthally averaged Fourier transform after deconvolving the (time-depedent) Jupiter disk and correcting for the $0.'5$ pixel window function. Some care needs to be taken when combining detectors together as naively resampling the maps will result in an additional pixel window function term. Each Jupiter observation results in an independent measurement of the beam window function B_ℓ which are then averaged in power spectrum space to form the final measured beam window

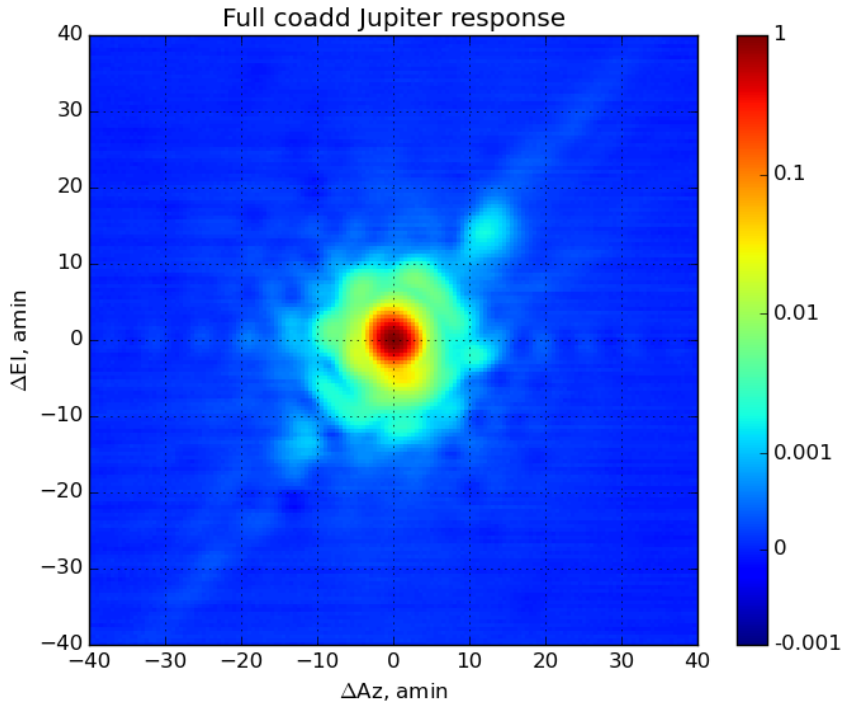

Figure 3.1: Jupiter response coadded across all observations. The beam window function is computed from the azimuthally averaged Fourier Transform of the individual observations that are coadded to make this map.

function. A map of the normalized Jupiter response can be seen in Figure 3.1

We find a beam window function that is similar to, but marginally wider than, the small patch data with a median Gaussian 3.′6 full width at half maximum (FWHM). This is possibly due to imperfect focusing of the telescope since the addition of the sapphire HWP lengthens the optical path between the primary and the secondary mirrors or the diffraction of light off the CRHWP aperture. We see no weather dependence or variation between seasons in the Gaussian beam width. This gives us some confidence that the beam measurements are not contaminated by detectors saturating on Jupiter under high optical loading.

Boresight and detector pointing error adds an additional suppression of high-ℓ power in the maps that is not included in the beam window function. As a result it is often convenient to work in terms of an effective beam window function with this term included. As described in Section 3.4, the pointing model predicts residual pointing errors of 0.′8 that adds in quadrature to the beam width. In Section 6.1 we fit an ℓ-dependence to the overall gain amplitude corresponding to the widening of the effective beam due to pointing error and find no statistical preference for an additional widening of the beam, however the error bars

on this fit are somewhat large as there is no high ℓ lever arm to constrain the adjustment to the beam width. As a result we convolve the beam function with a Gaussian corresponding to the best fit pointing model error from the E-mode spectrum and include the uncertainty in absolute gain and the effective beam width adjustment as a multiplicative calibration error.

An additional source of systematic uncertainty in the beam comes from detector crosstalk. We measure the detector beam window function using temperature data but compute polarization power spectra. As described in [57], crosstalk acts differently in temperature and polarization in the presence of a CRHWP resulting in an effective beam mismatch. This is produced by a supression of crosstalk in the polarization beams by the difference between detector polarization angles. This is described in detail in Section 8.5. We find this effect to be subdominant to the statistical uncertainty for all spectra.

3.2 Relative gains

Following the small patch analyses, we use a three step gain calibration to turn our TOD into physical temperature units. We measure time dependent gain calibration between detectors using a chopped thermal source before and after each four hour block of observations. This analysis is described in more detail in [58], however a description is provided here for completeness. We then preform a flat-fielding operation by constructing a template for the simulator brightness using the same Jupiter observations used to create the beam window function. Finally, we construct a CMB map and scale the overall amplitude of the polarization E-mode fluctuations to match Planck 2018. The final absolute gain calibration is described in Section 6.1. As The Planck overall gain is in turn set by the modulation of the solar dipole by the motion of the satellite around the sun [3].

At several points during the observations the thermal source used in the relative calibration was replaced for mechanical reasons. The conversion from the thermal source amplitude to temperature on the sky is performed separately for each source. The first / second half null tests and the season by season tests described in Chapter 7 act as a cross check for problems in this analysis. We simulate the systematic error introduced by uncertainty on the measured gain acting on both the CMB signal and the ground synchronous structure and find the contamination to be negligible. This is described in Section 8.2 and Section 8.6.

3.3 Detector time constants

Following previous POLARBEAR analyses the detector time constants are measured using the chopped thermal source. The frequency of the chopper sweeps from 4 to 44 Hz incrementally. The time constants are reconstructed by fitting a single pole model to the amplitude versus frequency. The time constant measurement is important for understanding the detector polarization angle calibration correct because a timing error between the detector signals

and the CRHWP encoder appears as a polarization angle error. This effect is described in Section 4.3.

3.4 Detector and boresight pointing

The telescope pointing reconstruction is performed in a very similar manner to the small patch analyses. A detailed discussion of this analysis is provided in [59] and an overview is presented here for completeness. The telescope is used for dedicated raster observations of bright point sources selected from catalogs [60, 61] prior to each science observation. The observed position is computed based on the telescopeâĂŹs azimuth and elevation encoder values compared to the expected positions. The resulting azimuth and elevation offsets $\Delta\mathrm{Az}(\mathrm{Az},\mathrm{El}), \Delta\mathrm{El}(\mathrm{Az},\mathrm{El})$ are fit to an eight parameter model including terms for uneven heating of the telescope, misalignment of the telescope axes, and structural flexure. We find an RMS pointing model residual (i.e. the difference between the fitted planet positions and the positions predicted by the pointing model) of $0.'8$. Fitting the ten parameter model used for the second season small patch does not result in significantly improved pointing model residuals compared to the fiducial 8 parameter model.

We also construct pointing solutions that include the Crab Nebula (Tau A) and Jupiter scans performed for polarization angle and beam calibrations in the same way, however this data is not used in the fiducial boresight pointing solution. In Section 8.4 we show that the difference between these pointing solutions is negligible for the ℓ range considered in this analysis.

The detector beam offsets are derived from array raster scans over Jupiter. We find that the reconstructed offsets are consistent with previous results at the level of several tens of arcseconds. We explicitly cut several detectors whose fitted beam offset differs from the small patch data by more than one arcminute. This cut has a negligible impact on the overall data selection efficiency.

3.5 Polarization angles and efficiencies

The detector polarization angles and efficiencies are derived from dedicated raster scans of Tau A. A detailed description of the polarization angle and efficiency results are provided in [62], however a description of the most important results is provided here as well. Tau A is a polarized supernovae remnant located at (RA, Dec) = $(+5^{\mathrm{h}}34^{\mathrm{m}}32^{\mathrm{s}}, +22^{\circ}52')$, meaning it can only be observed by mid-latitude or northern hemisphere experiments. Tau A is close to the ecliptic plane meaning it cannot be observed for some of the year when the sun passes nearby. The raster scan data is taken at $0.^{\circ}2$ s^{-1} scan speed on the sky with the CRHWP rotating nominally. We deconvolve the detector time constants measured from a chopped thermal source calibration immediately before and after the Tau A raster scan. After correcting for detector time constants, we find no significant correlation between the measured polarization

angle and the precipitable water vapor (PWV) measured at the nearby Atacama Pathfinder Experiment (APEX)[1] site. As explained in Section 4.3 the time constant deconvolution is necessary to accurately reconstruct the polarization angle because a time shift between the bolometers and the CRHWP encoder appears as a polarization angle error. The polarization TOD is fit to a beam convolved polarization map of Tau A from a measurement taken with the IRAM 30 m telescope [63]. We find a statistically consistent polarization angles compared to previous results and find no significant variation between seasons. We find the difference in measured polarization angle between detectors in a pair to be $90\overset{\circ}{.}5 \pm 1\overset{\circ}{.}2$ which is consistent with the design value of 90°. In Section 8.3 we simulate two different ways that detector polarization angle can create systematic contamination in the measured CMB power spectra. Individual detector polarization angle mixes E-modes into B-modes and global polarization angle error creates a non-zero EB spectrum and mixing even after absolute angle calibration due to the fact that the mapmaking pipeline is not invariant under global polarization angle rotation. We find both forms of systematic contamination to be negligible at our sensitivities.

In addition, the Tau A scans are used to estimate the polarization efficiency of the telescope optics and receiver. The addition of the CRHWP degrades the polarization efficiency of the instrument due to three physical effects.

These three effects are the non-ideality of the CRHWP, the breaking of the Mizuguchi-Dragone (MD) condition [38, 39] and non-zero bolometer time constants. The modulation efficiency of the CRHWP is estimated from coherent source lab measurements and the design antenna bandpasses [36]. The polarization efficiency term due to the MD breaking is estimated from a GRASP[2] physical optics simulation described in [64] that has been rescaled to match the physical size of the POLARBEAR focal plane. The detector time constant acts as a time domain low pass filter on the timestreams which has a response less than unity at the center of the polarization band. We find the measured polarization efficiency from the Tau A calibration to be consistent with the predictions but with a larger statistical error as expected. The CRHWP and MD breaking polarization efficiency terms are intrinsic to the detectors and telescope geometry and are corrected by rescaling the timestreams and noise weights with the estimated polarization efficiencies. The detector time constants depend on the detector bias point and optical loading. As a result, this polarization efficiency term is corrected by deconvolving the measured time constant from the chopped thermal source calibration before and after each four hour set of scans.

We self calibrate the overall polarization angle by fitting $C_\ell^{EB} = 0$ following [65]. The overall polarization efficiency is degenerate with the absolute gain of the polarization maps and is set by matching the POLARBEAR E-mode spectrum to the Planck E-mode spectrum. This analysis is described in more detail in Chapter 6.

[1] http://www.apex-telescope.org/

[2] https://www.ticra.com/software/grasp

Chapter 4

Data Analysis

In this chapter we describe the formalism and processing steps used to turn the raw bolometer TOD into maps and subsequently power spectra paying particular attention to ways in which the pipeline differs from the previous POLARBEAR analyses.

4.1 Overview of the analysis pipeline

At a high level, the analysis pipeline consists of three interconnected components. The first component is data selection. Any data containing pathological anomolies is marked so that it does not contaminate the results of the mapmaking operation. The second component is the mapmaker itself, which takes the data passing all data selection criteria and produces an estimate of the CMB anisotropies corresponding to that data. The mapmaking operation must account for the noise properties as well as non-idealities of the data by filtering and weighting the TOD before projecting it onto the sky. In most pipelines this results in a biased estimate of the underlying CMB anisotropies. The final component is power spectrum estimation, in which the map is used to estimate the underlying CMB power spectrum. The power spectrum estimation is done in two steps. The first step is (effectively) a two dimensional Fourier transform of the map resulting in what is termed a pseudo spectrum. In the second step, a series of linear operations is performed to correct for the biases introduced in the mapmaking operation and produce an estimate of the true CMB power spectrum.

4.2 Data selection

The data selection framework used in this analysis consists of four rounds of increasingly selective criteria to characterize low frequency noise and mitigate possible systematic contamination. The stages can be roughly described as 1) masking glitches and effects confined to narrow time boundaries in the TOD, 2) cutting data based on individual detector noise properties over the course of an observation, 3) cutting CESs based on array common mode time domain noise properties, and 4) cutting CESs based on map domain noise properties.

Stage of data selection	Efficiency
Stage 1: Glitch cuts and off bolometers	14.8 %
Stage 2: Individual bolometer PSD cuts	76.6 %
Stages 3 and 4: Common mode PSD and map cuts	79.6 %

Table 4.1: Data selection efficiency for this analysis. These numbers represent the fraction of bolometer time kept by each stage of the data selection.

The data selection is tightly coupled to the mapmaking pipeline as the mapmaking TOD filters are used at several points in the data selection pipeline and the noise properties derived in the data selection are used as inputs in the mapmaking operation.

In all stages of data selection and mapmaking, the fundamental unit of data considered is the detector subscan (referring to one left going or right going motion of the telescope). Data where the telescope is accelerating (referred to as turnarounds) are rejected completely. A table of efficiencies is shown in Table 4.1. After data selection 2985 CESs have data that is used in the mapmaking operation.

The first stage of data selection consists of two steps, searching for fast glitches localized to individual bolometers and searching for common mode low frequency glitches. This analysis is described in more detail in [66] and [56], however a summary is provided here for completeness. In the first step a time domain glitch criteria similar to previous analyses is applied to the pre-demodulated timestreams to find and remove high frequency features. The TOD are convolved with a high-pass kernel designed to pick up sharp temporal spikes in the data while nulling the HWP synchronous signal at multiples of 2 Hz. Subscans where the maximum deviation of the convolved TOD is greater than ten times the standard deviation is discarded. The initial glitch finding operation is performed on the full sample rate data to improve sensitivity to fast glitches. The full sample rate data is then demodulated following in Section 4.3. The $0f$, $2f$ and $4f$ TOD (where nf corresponds to the demodulation about the n^{th} harmonic of the HWP frequency, i.e. $0f$ is the intensity signal and $4f$ is the polarization signal) are convolved with an additional series of high pass kernels and subscans are cut following the same ratio of maximum deviation to standard deviation.

After the fast glitch flagging, we search for common mode low frequency glitches. In [66], it is shown that these glitches correspond to polarized emission from clouds in the upper atmosphere. The data selection criteria used in this paper are identical to the cloud detection criteria defined there. Detectors are selected by preforming a principle component analysis of the focal plane and removing channels whose intensity timestreams are not dominated by the large atmospheric common mode. The $Q + iU$ timestreams from each detector are rotated into the instrument frame by multiplication with $e^{i2\theta_{\text{det}}}$. These TOD are coadded to form a full focal plane common mode signal which is rotated again into minimum and maximum variance eigenmodes. Subscans where the ratio of the standard deviations of the

two modes is greater than ten are cut.

In the second stage, we estimate the individual detector noise properties after demodulation and cut based on detector noise statistics. Each demodulated timestream is high-pass filtered by a first-order subscan polynomial filter, ground-fixed signals and temperature to polarization leakage are subtracted and turnarounds and subscans flagged by the glitch cuts are filled in using matched white noise. The power spectral density (PSD) of the resulting "cleaned" TOD is fit to a model consisting of white noise and a $1/f^2$ low frequency noise term. We do not allow the power law exponent of the low frequency noise to float in the individual detector PSD fits because there is not a sufficient lever arm to resolve the spectral shape of the low frequency component. The fit is cut off at 25 mHz where the action of the first order subscan polynomial becomes significant (note the scan frequency $f_{\rm scan} \approx 10$ mHz). Detectors with anomalously high white noise floors, high low frequency noise, or poor fits to the model are discarded. The fit quality is estimated using the most extreme and average χ^2 of the real PSD to the fit model within subsets of the frequency range 25 mHz to 1.2 Hz. No cuts are applied to the bandwidth above 1.2 Hz as this is removed by a low pass filter in the mapmaking pipeline. Common mode Fourier domain glitches are noted when more than 50 detectors see a 8σ excess in the same frequency bin. These lines are notch filtered in subsequent steps of the pipeline. This detection threshold is tuned by hand examining two dimensional plots of the individual detector PSD versus detector number and frequency.

In the third stage, the common mode timestream is re-computed using the fitted inverse individual detector noise weights and the additional data cuts and Fourier notch filters defined in the second stage. We compute the common mode PSD by inverse variance weight averaging the individual detector timestreams. We fit the common mode PSD to the form $A_0(1 + (f_{\rm knee}/f)^\alpha)$ for Q and U separately. Here Q is taken to be aligned with the instrumental polarization produced by the finite conductivity of the primary mirror. The detector white noise is supressed by the focal plane averaging, however the coherent low frequency component is not meaning the knee frequencies are somewhat higher. As a result there is a sufficient lever arm to resolve the power law α in the common mode PSD.

Observations where the common mode knee frequency $f_{\rm knee}$ in instrument frame Q (U) is greater than 150 mHz (100 mHz) or where the common mode noise floor is anomalously high are rejected. We find median knee frequencies of 45 mHz (24 mHz) in the common mode Q (U) PSD. A discussion of the difference between Q and U low-frequency noise is discussed in Section 5.2.

In the fourth stage, the detector weights computed in the second stage and the common mode PSD defined in the third stage are used to create individual observation maps following the standard TOD filtering outlined in Section 4.4 with the modification that the telescope frame $Q + iU$ is treated as a scalar field and not rotated into right ascension and declination coordinates. The maps are downsampled to degree pixels and a map χ^2 is computed by comparing the noise fluctuations in the individual observation maps to the expectation from

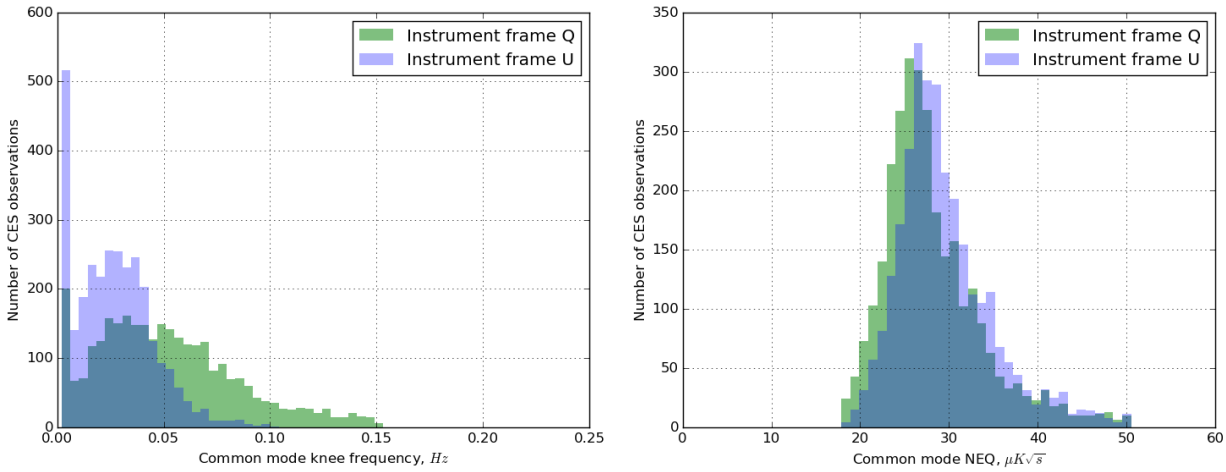

Figure 4.1: Distribution of common mode white noise floor and knee frequency for instrument frame Q and U. The white noise floor in U is slightly higher due to noise in the CRHWP angle reconstruction. The low frequency noise in Q is significantly higher than U for reasons discussed in Section 5.2

the individual detector noise weights. Maps with an anomalously low or high χ^2 are rejected. This cut strongly overlaps with the common mode PSD criteria and is used as a cross check for low frequency anomolies that may not be visible in the common mode PSD shape.

Finally, observations with fewer than 100 active bolometers are cut from the data set. This has a negligible impact on the overall data selection efficiency.

4.3 Demodulation and TOD pre-processing

This analysis follows what is shown in previous work [52, 56, 66], however a brief overview is provided here for completeness. The raw bolometer TOD can be modeled following:

$$d_m(t) = I(t) + \varepsilon \mathrm{Re}\{[Q + iU](t)\, e^{-i(4\chi + 2\theta_{\mathrm{det}})}\} + A(\chi, t) + \mathcal{N}_m \tag{4.1}$$

where $\chi \approx \omega t$ is the CRHWP angle, $e^{-i4\chi}$ encodes the polarization modulation of the CRHWP, ε is a polarization efficiency, θ_{det} is the geometric detector angle, $\mathcal{N}(t)$ detector noise and $A(\chi, t)$ is a slowly varying CRHWP synchronous structure. A detailed explanation of this structure can be found in [56]. In general time-varying CRHWP synchronous structure is degenerate with on sky polarization so the model of the time dependence of $A(\chi, t)$ must be confined to a small number of degrees of freedom.

Prior to demodulation we subtract the CRHWP-synchronous signal $A(\chi, t)$ using an iterative method similar to [67]. Any gaps in the bolometer TOD are filled and the CRHWP angle is reconstructed from the encoder. The CRHWP synchronous structure is estimated

following [68] and is decomposed into harmonics. Gaps in the TOD are filled with the CRHWP synchronous structure. At each harmonic $n \in \{1, 2, \dots 7\}$, the TOD is bandpass filtered and demodulated to form a time dependent amplitude for that harmonic of the CRHWP synchronous structure. A linear drift is fit to the amplitude of each harmonic. The sum over of these templates is subtracted from each TOD and the process is iterated again. After the CRHWP structure has been subtracted, the polarization signal is reconstructed by multiplying the data by twice the conjugate of the modulation function $e^{i4\chi}$ and low pass filtered to recover the polarization signal,

$$d_d(t) = \varepsilon[Q(t) + iU(t)]e^{-2i\theta_{\rm det}} + \mathcal{N}_d. \tag{4.2}$$

. The $4f$ CRHWP synchronous structure is then restored. The demodulated data is downsampled to $f_{\rm sample} = 8$ Hz to conserve memory in subsequent stages of the pipeline. Note that the noise in the demodulated timestreams $\mathcal{N}_d$ is complex and both the real and imaginary components have twice the variance of the modulated detector white noise $\mathcal{N}_m$ due to the factor of two necessary to recover Q and U correctly. The CRHWP allows the simultaneous measurement of both Q and U from each bolometer, however there is no net noise benefit compared to the pair differencing case. The noise $\mathcal{N}_d$ can be well described as white noise plus a single low frequency component common to all detectors. The noise model is described in Chapter 5.

The demodulation algorithm assumes perfect separation of intensity and polarization signals in temporal frequency, or in other words the CRHWP frequency is much higher than the scan speed divided by the beam size. In Section 8.7 we quantify the impact of imperfect separation in the real data and find the effect to be negligible. This demodulated data is used as the input to the subsequent data characterization and mapmaking pipelines. Due to the large number of Fourier Transform operations required in the CRHWP subtraction routine, including the demodulation in our main simulation pipeline would have been computationally prohibitive.

4.4 MASTER mapmaking

In this analysis, we use a MASTER "filter and bin" mapmaker [69] where the TOD is filtered to suppress low frequency noise and projected onto the sky using the inverse noise variance weights.

The mapmaking pipeline takes the demodulated data described in Section 4.3 and applies an additional stack of time domain filters. The most important and subtle filtering operation in the TOD filtering pipeline is the temperature to polarization leakage subtraction. As described in [52], the finite conductivity of the primary mirror produces a polarized signal from the unpolarized atmospheric emission. This leads to temperature to polarization leakage through two physical mechanisms, directly by varying atmospheric brightness and via the non-linearity of the detectors. The ordering of the filtering operations is somewhat important

to avoid bias in the estimated temperature to polarization leakage coefficients by spurious modes in the temperature or polarization TOD.

The first filtering operation works in the Fourier domain and removes signal above 1.2 Hz and notch filters Fourier domain glitches flagged in the data selection pipeline. A notch width of 10 mHz is used on every bolometer on the focal plane when a Fourier domain glitch is flagged in the data selection. An identical set of low pass and notch filters are applied to the simulation data. The sample rate window function associated with the 8 Hz TOD sample rate is negligible for the ℓ ranges considered. We run simulations with an upsampled input map scanning operation and simulate the 8 Hz downsampling and find the difference relative to the scanning the input map at 8 Hz to be negligible.

The second filtering operation removes a second order polynomial from the hour long observation. This mode is expected to be dominated by thermal fluctuations on the focal plane and cryogenics. Masked data is not used in the determination of the polynomial coefficients.

The third filter subtracts a ground-fixed template in telescope frame I, Q, and U from each detector for each observation. It is suspected that this signal is due to telescope sidelobes far from the main beam seeing the surrounding terrain, however we have not been able to explicitly confirm this theory.

This can be studied by projecting the data into sun centered coordinates (either the science data or dedicated scans with a very large throw), however the results from this analysis for POLARBEAR have been inconclusive. We observe some shift in the low-elevation ground synchronous structure at the same time as the installation of the two additional Simons Array telescopes.

Unlike previous analyses, the same template is used for both left-going and right-going subscans. We bin each detector timestream in 15 arcminute bins by boresight azimuth and project this mode out of the data. We conservatively assume no correlation between observations even though the ground fixed signal that we observe is stable between observations. We have tested varying the bin size and subtracting out a smoothed version of theground fixed template and find no significant difference in the final measured power spectrum.

The ground fixed structure subtraction filter assumes a model where any ground pickup is constant during an hour observation. In Section 8.6 we place an upper limit on the error introduced by possible time variability in the ground synchronous structure.

Once these modes have been projected out of the data we perform a principle component analysis (PCA) similar to [52] to remove temperature-to-polarization leakage due to detector non-linearity and instrumental polarization from the off-axis telescope design. We see a weak frequency dependence in the temperature leakage coefficients below the telescope scan frequency in the IQ and IU cross spectra averaged over many detectors and observations. As a result, the leakage coefficients for each bolometer observation are determined after a first order polynomial subtraction is applied to the TOD. An additional low pass filter at 400 mHz is applied to each subscan to avoid excess noise in the coefficients and bias from Fourier lines at higher frequencies. the leakage coefficient for the entire observation is determined from the mean IQU covariance matrix from each subscan kept by data selection. We find the es-

timated leakage coefficients to be stable over the course of the hour long observations. Once the coefficients are determined, the leakage is subtracted from the polarization TOD without the low-pass filter applied. The subscan polynomial degree of freedom is removed alltogether in the subsequent TOD filter. Since the leakage coefficient determination is heavily dominated by atmospheric fluctuations we do not expect this process to be significantly biased by cosmological signal. In Section 8.2 we simulate the error expected in the B-mode power spectrum due to multiplicative detector non-linearity and find the effect to be negligible. As a result, we do not simulate this leakage or the PCA filter in the mapmaking pipeline.

Following this a first order polynomial is subtracted from each subscan in polarization to mitigate low frequency noise. A ninth order polynomial is subtracted from each subscan in temperature, however the temperature maps are never used in the low-ℓ analysis.

Finally, a common mode high-pass filter is applied to the data to suppress the low frequency common mode seen in all detectors. This means that a low-pass filtered version of the array common mode is subtracted from each detector. The spectral shape of the filter applied to the array common mode is the inverse of the fit power spectral density of the stacked timestream derived in the data selection pipeline. The same filter is applied to simulated data. As described in Chapter 5 we do not see significant low frequency noise beyond a single focal plane common mode.

We project the TOD into $8'$ pixels on the sky using a Lambert Cylindrical equal area projection. The large pixels are used to reduce disk I/O when running the simulations. This becomes critical in the null tests where the number of individual maps is very large. The high-ℓ analyses have reimplemented the mapmaking and coadding steps to circumvent this problem. The Lambert Cylindrical projection is chosen because the flat sky $E \rightarrow B$ leakage is negligibly small. The resulting maps for the real data and a sample noise realization are shown in Figure 4.4.

4.5 Power spectrum estimation

The power spectrum estimation pipeline closely follows the MASTER pipeline implemented for the small patch analyses with several minor changes to improve numerical accuracy at low-ℓ.

The dataset is grouped into 38 bundles of approximately uniform weight and sky coverage. These bundles are created from the ten day cycles produced by the scan strategy with several ten day cycles combined in post-processing due to low weight or non-uniform coverage. We form pseudo power spectra by taking cross spectra between these bundles to remove the noise bias,

$$\tilde{C}^{XY} = \frac{1}{\sum_{i \neq j} w_i w_j} \sum_{i \neq j} w_i w_j \mathbf{m}_i^X \mathbf{m}_j^{Y*} \tag{4.3}$$

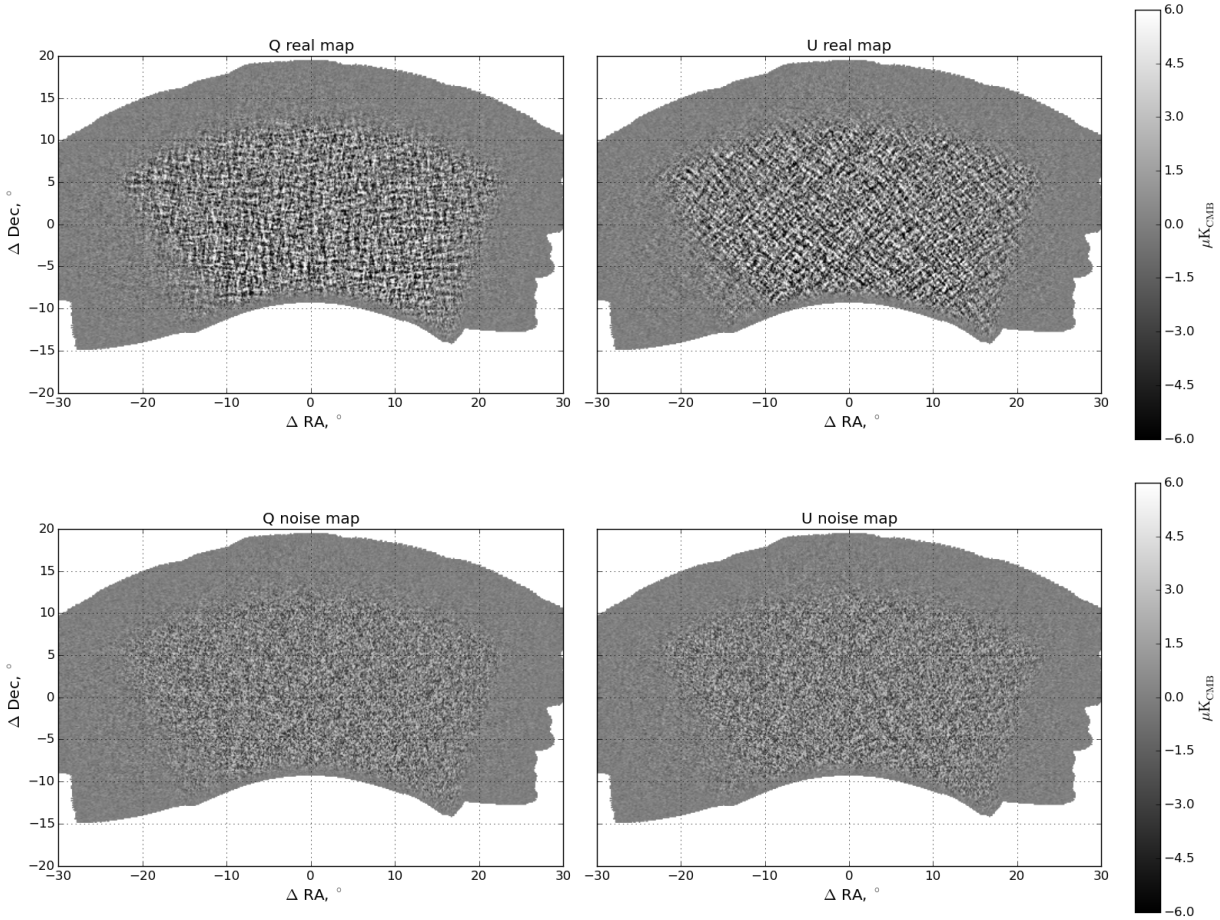

Figure 4.2: Real POLARBEAR Q and U maps (top) and a sample noise realization (bottom) produced using the "signflip" coadd pipeline. The E-mode structure is clearly visible in the real maps as the vertical and diagonal checkerboard pattern in the Q and U maps. The "signflip" noise realizations are used to estimate the band power covariance of the the final power spectrum and the noise bias used in the foreground estimation pipeline.

where $\mathbf{m}$ and w are the apodized Fourier transform and weight of each map bundle, respectively. The pseudo spectrum is averaged into bins of $\Delta\ell = 2$. We use a pure B-mode estimator based on [70] and [71]. We modify the ℓ-dependent pure B-mode normalization relative to the small patch power spectrum estimator to give a closer correspondence between the pure B-mode and pseudo B-mode spectra. The apodization mask used in the pseudo spectrum is significantly more aggressively smoothed than the small patch analysis. We apply an 8° cosine square edge taper because the pure-B mode estimators require that both the apodization function and its first derivative vanish on the patch boundary. We also apply an 8° Hamming window to the pixel weight map. In general the optimum shape for an apodization function depends on the ℓ value being measured [71]. The very agressive smoothing of the weight function somewhat improves the numerical stability of the MASTER estimator by reducing the off-diagonal structure in the mode coupling matrix as explained in Section 4.7. We do not mask point sources in the power spectrum estimation to avoid sharp features in the apodization mask or significant loss of sky area. We do not see evidence for bright polarized point sources in higher resolution versions of our maps. As described in Section 10.5, we expect the contamination from unresolved polarized point sources to be negligible for this ℓ range.

The noise pseudo spectrum $\tilde{N}^{XY}$ is taken to be the pseudo spectrum of sum of the apodized map bundles $\tilde{A}^{XY}$ minus the cross pseudo spectrum $\tilde{C}^{XY}$. It is important to note that the sum of the apodized map bundles is not the same as the apodized sum of the map bundles. This means that our definition of the noise bias differs slightly from other experiments such as BICEP2 and *Keck Array*. We define an alternate power spectrum estimation pipeline in Section 4.6 for cases where it is more convenient to work with the full data map.

The pseudo spectrum is taken to be a linear function of the true underlying power spectrum on the sky,

$$\tilde{C}_\ell = \sum_{\ell'} \mathbf{K}_{\ell\ell'} C_{\ell'}. \tag{4.4}$$

The transformation is given by

$$\mathbf{K}_{\ell\ell'} = \mathbf{M}_{\ell\ell'} F_{\ell'} B^2_{\ell'}. \tag{4.5}$$

The mode mixing mixing matrix $\mathbf{M}_{\ell\ell'}$ describes the mixing of ℓ modes due to finite sky coverage and is estimated directly by computing the pseudo spectrum of narrow band ($\Delta\ell = 2$) noise realizations. The filter transfer function is found via an iterative procedure following previous POLARBEAR analyses

$$F^n_\ell = F^{n-1}_\ell + \frac{\tilde{C}_\ell - \sum_{\ell'} \mathbf{M}_{\ell\ell'} F^{n-1}_{\ell'} C_{\ell'} B^2_{\ell'}}{C_\ell B^2_\ell};\ F^0_\ell = 1. \tag{4.6}$$

In contrast to previous POLARBEAR analyses we cut the iterative series off at $n = 3$ to avoid over-fitting fluctuations in the simulated pseudo spectra. This numerical instability is

a consequence of the fact that isolating F_ℓ in Equations 4.4 and 4.5 requires inverting the (poorly conditioned) mode mixing matrix. Truncating the series results in a detectable but negligible bias in the lowest bin of the reconstructed power spectrum. Previous analyses have simply smoothed the filter transfer function F_ℓ, however this introduces a larger bias in the low-ℓ bins where the filter transfer function is rapidly falling off. The filter transfer function is calculated using simulated ΛCDM EE-only and BB-only skies drawn from the Planck 2018 best fit ΛCDM cosmology [10] with $1'$ pixels. We verify that the numerical value of the filter transfer function does not depend on the underlying cosmology used in the simulations by computing the same transfer functions using power law $D_\ell \propto \ell^{\ \alpha\in\{2,0,-2\}}$ input spectra.

We estimate the power spectrum in coarser bins of width $\Delta\ell = 50$. The binned estimate for the true power spectrum can be written using the binning and interpolation operators $\mathbf{P}$ and $\mathbf{Q}$,

$$\hat{C}_b = \sum_{b'\ell} \mathbf{K}^{-1}_{bb'} \mathbf{P}_{b'\ell} \tilde{C}_\ell \tag{4.7}$$

$$\mathbf{K}_{bb'} = \sum_{\ell\ell'} \mathbf{P}_{b\ell} \mathbf{M}_{\ell\ell'} F_{\ell'} B^2_{\ell'} \mathbf{Q}_{\ell' b'}. \tag{4.8}$$

The dependence of the binned spectrum on the underlying spectrum is given by the band power window functions $\mathbf{w}_{b\ell}$.

$$\hat{C}_b = \sum_{\ell} \mathbf{w}_{b\ell} C_\ell \tag{4.9}$$

$$\mathbf{w}_{b\ell} = \sum_{b'\ell'} \mathbf{K}^{-1}_{bb'} \mathbf{P}_{b'\ell'} \mathbf{K}_{\ell'\ell} \tag{4.10}$$

These band power window functions and filter transfer function are shown in Figure 4.3. The shape lowest bandpower is due to sensitivity degradation at low-ℓ. We have validated the end-to-end pipeline with both healpix curved sky and flat sky inputs.

The statistical uncertainty on the reconstructed power spectrum is taken to be the standard deviation of the Monte Carlo (MC) simulations. We also compute analytic uncertainties in the same way as the first season following:

$$\Delta\hat{C}^{BB}_b = \sqrt{\frac{2}{\nu_b}} \left(C^{BB}_b + \hat{N}^{BB}_b \right) \tag{4.11}$$

where ν_b is the effective number of degrees per bandpower,

$$\nu_b = (2\ell_b + 1)\Delta\ell f_{\mathrm{sky,eff}} \tag{4.12}$$

It should be noted that this formula misses a somewhat subtle point. The effective f_{sky} (equivalently the effective number of degrees of freedom per ℓ) depends on the ratio of signal-to-noise in the map. In the signal dominated limit

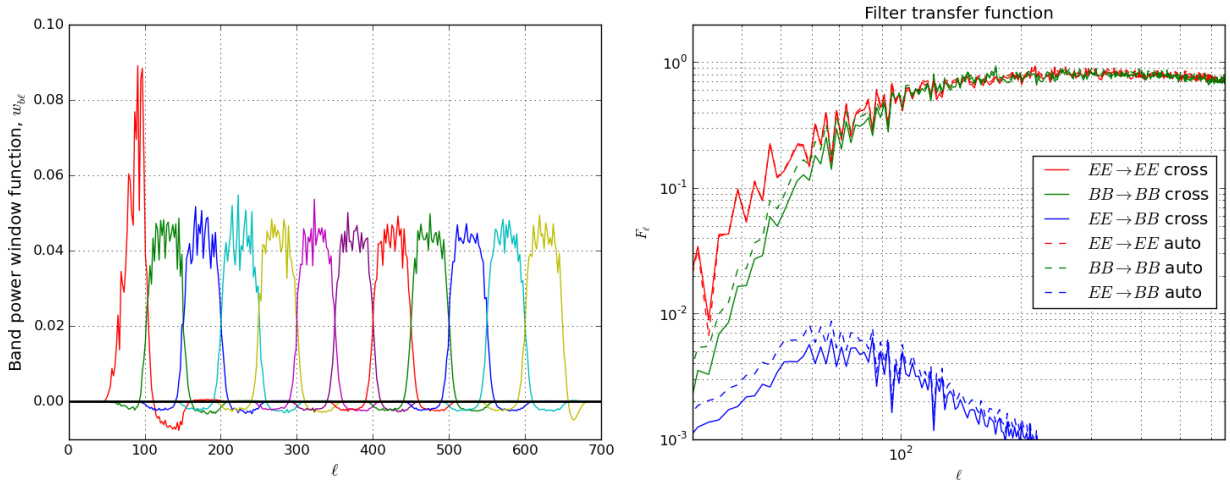

Figure 4.3: BB band power window functions (left), filter transfer function (right). The shape of the lowest bandpower is due to the sensitivity degradation at low-ℓ due to timestream filtering. The filter transfer function is shown for both the fiducial cross spectrum pipeline and the alternate auto spectrum pipeline described in Section 4.6.

$$f_{\mathrm{sky,\,(signal)}} = f_{\mathrm{sky,tot}} \frac{w_2^2}{w_4}, \tag{4.13}$$

whereas in the noise dominated limit

$$f_{\mathrm{sky,\,(noise)}} = f_{\mathrm{sky,tot}} \frac{w^2}{w_2}. \tag{4.14}$$

Here w_i is the i^{th} moment of the weight function. The difference can be understood as follows. The apodization function is based on an inverse pixel variance weight w. The standard deviation of the noise fluctuations in each pixel therefore goes as $w^{-1/2}$. Therefore, the apodized noise map looks like apodized signal with the substitution $w \to w^{1/2}$. In practice the correct effective f_{sky} will lie somewhere between these two limits. It should also be noted that the supression of low ℓ modes by TOD filtering also supresses the effective f_{sky} in an ℓ-dependent manner as described in Chapter 5.

In addition to supressing power at low-ℓ, the TOD filtering mixes E-mode power into the B-mode spectrum. This is subtracted in pseudo spectrum space following previous POLARBEAR analyses:

$$\tilde{C}_\ell^{E\to B} = \frac{F_\ell^{E\to B}}{F_\ell^{E\to E}} \tilde{C}_\ell^{E} \tag{4.15}$$

This reconstructs the correct central value of C_ℓ^{BB} however does not remove the excess variance in the B-mode spectrum. We find that the level of B-mode power introduced

by timestream filtering is comparable to the expected lensing B-mode signal in our lowest band power. Since this is significantly below the noise bias the excess B-mode variance is negligible, however we nonetheless account for this effect in our statistical uncertainty by subtracting the measured E-mode spectrum in each realization. A discussion of how to treat this in a more sophisticated manner is provided in Section 4.7.

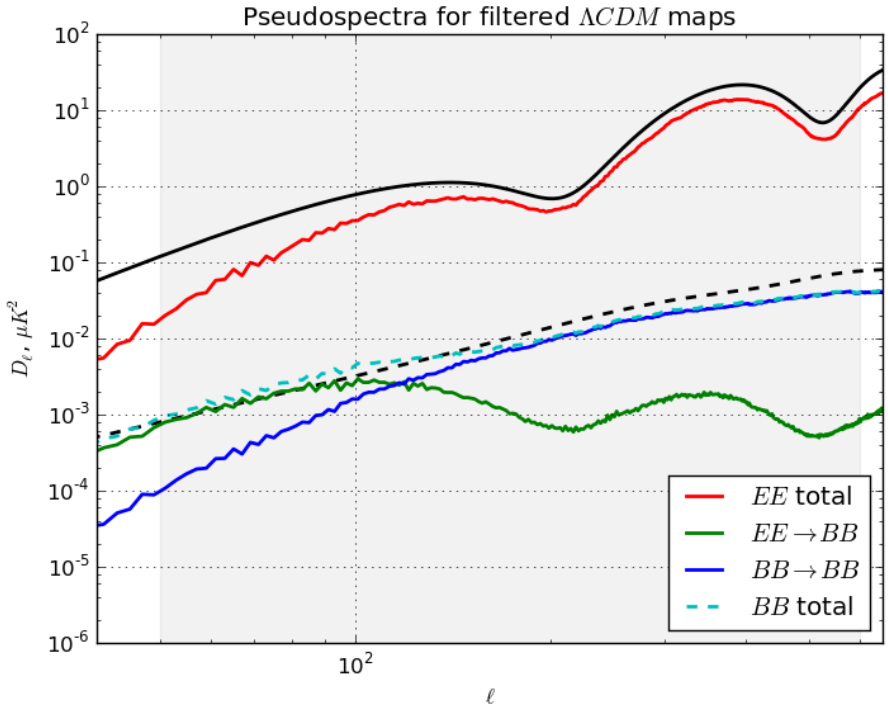

Figure 4.4: Pseudo spectra illustrating $E \rightarrow B$ leakage due to TOD filtering. The leaked E modes from the TOD filtering pipeline will limit the sensitivity of the r constraint at a map depth of a few μK-arcmin.

4.6 Internal cross spectrum and auto spectrum estimators

In Section 10.1, we consider the cross correlation of our data with the Planck 2018 maps for foreground estimation. In this pipeline we use the auto spectrum of the fully coadded map in place of the cross spectra between map bundles and subtract the noise bias using simulations. The power spectrum estimation follows the fiducial pipeline exactly with the substitution:

$$\tilde{C}^{XY} = \mathbf{m}^X \mathbf{m}^{Y*} \tag{4.16}$$

where $\mathbf{m}$ is the Fourier transform of the apodized fully coadded map. We recompute the filter transfer function F_ℓ for this pipeline and find numerical values that differ at the level of a few percent from the fiducial filter transfer function. We find that the two estimators yield statistically compatible results with the real data and the "signflip" noise realizations.

4.7 Moving beyond the naive MASTER pipeline

The MASTER pipeline formalism [69] has become one of the standard techniques in CMB data analysis. Nonetheless, there are several aspects of the method that are suboptimal for deep surveys attempting to reconstruct large angular scale polarization. The power spectrum estimation formalism assumes that the pseudo spectrum is a linear function of the true underlying spectrum following:

$$\tilde{C}_\ell = \sum_{\ell'} \mathbf{M}_{\ell\ell'} F_{\ell'} B_{\ell'}^2 C_{\ell'} \tag{4.17}$$

When considering E and B modes a the filter transfer function F_ℓ becomes a 2×2 matrix where the $B \to E$ mixing block is generally neglected. The elements of this matrix are constrained by scanning E-only and B-only simulations and looking at the output pseudo spectra for each case.

However, upon closer inspection, there are several problems ranging from practical issues of numerical stability to fundamental limits of the method.

- Isolating and solving for the filter transfer function F_ℓ (assuming $\tilde{C}_\ell$ is a noisy measurement from simulations) requires inverting the mode mixing matrix $\mathbf{M}_{\ell\ell'}$ which is generally poorly conditioned. One solution is to invert the order of the operations, $\mathbf{M}_{\ell\ell'} F_{\ell'} \to F_\ell \mathbf{M}_{\ell\ell'}$ which removes this numerical stability issue.

Problems surface when the leakage from E-modes to B-modes becomes significant.

- The formalism assumes that this can be totally captured by a scalar filter transfer function $F_\ell^{E\to B}$, however in general the leakage will mix ℓ modes in addition to mixing E into B diagonally in power spectrum space. The mode mixing matrix and filter transfer function could treated as a single atomic operation $F_{\ell\ell'}^{X\to Y}$ for $X, Y \in \{E, B\}$, however this dramatically increases the number of simulations necessary as the input maps must cover every ℓ' value individually.

- The subtraction of $E \to B$ leakage in power spectrum results in the corect central value of $\hat{C}_\ell$, however it does not treat the excess variance in the B-mode channel from leaked E-modes. This additional variance, could become the primary limitation for future instruments producing deeper CMB maps.

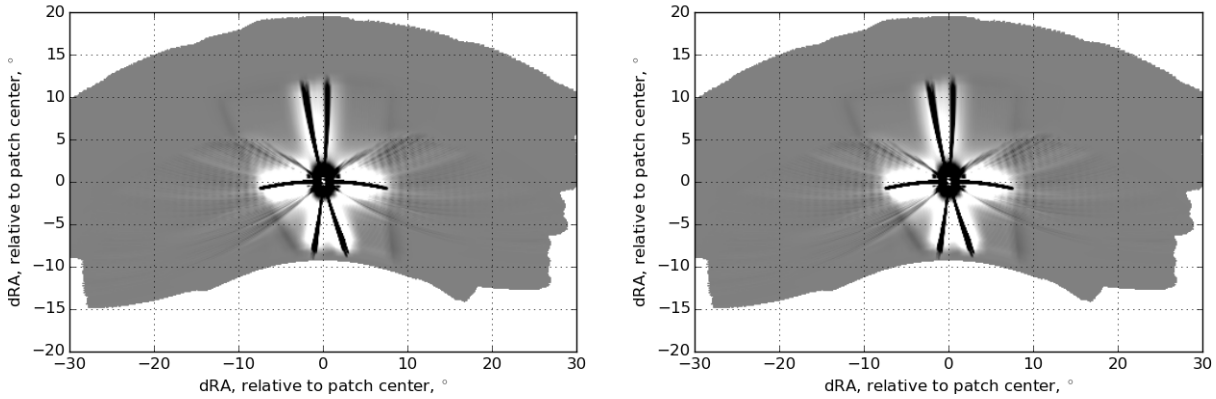

Figure 4.5: Output from the TOD filtering pipeline for an input Q delta function map. The vertical stripe is the subscan polynomial and the horizontal stripe is the ground template filter. In the BICEP and *Keck Array* formalism this is a column of the observing matrix $\mathbf{R}$.

There are two roads that one could take to address these problems. The first is to make the mapmaker smarter and attempt to undo the action of the filter transfer function on a mode-by-mode basis. This has been demonstrated in [46] for the POLARBEAR small patch data in the pair differencing case. The second approach is to undo the mixing at the power spectrum stage as demonstrated in [72]. This is the basis for the BICEP and *Keck Array* power spectrum estimation. In this approach, the process of the observing pipeline is written as a single matrix $\mathbf{R}$ and incorporated into the B-mode purification described in [73]. A column of the matrix $\mathbf{R}$ for POLARBEAR data is shown in Figure 4.5. This can be compared to Figure 10 in [72]. Chilean experiments will generally have much less sparse observing matrices than South Pole experiments due to the more complicated scan strategies.

In principle, given a suitably deep E-mode map, one can undo the realization-dependent $E \rightarrow B$ leakage by simply deprojecting the leaked E-modes from the B-mode map. This method will not generally be robust to systematics and noise in the E-mode template map and would need to be validated by simulations.

Chapter 5

Low-Frequency Noise

In this chapter we describe the models developed for the low frequency noise that we observe in the TOD and its impact on our power spectrum errors.

5.1 Noise modeling

We find the excess variance in the data at low frequencies to be modeled well by a single array common mode $1/f^{\alpha}$. We run the end-to-end analysis pipeline in two configurations; one using a TOD noise model and the other using random sign coaddition of individual observation maps to generate "signflip" noise realizations. The fact that we are able to demonstrate good agreement between the models indicates that higher order modes on the focal plane are negligible in polarization.

In the TOD noise model, we generate uncorrelated white noise on an individual detector basis using the noise weights derived in Section 4.2. The common mode low frequency noise synthesized in telescope coordinates for Q and U separately and is matched to the amplitude and power law index α fit from the real data. This common mode is then rotated into the polarization angle of each detector and added to the uncorrelated white noise. This simulated TOD is then used as the input for the subsequent mapmaking steps.

In the "signflip" configuration, the noise realizations are generated by randomly assigning a +1 or -1 factor to each observation during the coaddition of individual CESs. This is done such that the total data weight is even for both signs. Each map has a total polarization weight computed during the data selection pipeline. The list of maps is radomly permuted and the cumulative sum up to half of the total weight is multiplied by -1. The same sign flip pattern is used when all null test splits are coadded simultaneously ensuring that the correlations between the splits are accounted for correctly. Assuming that there is no noise correlation between CESs this creates noise realizations with the exact correlation structure of the real data.

We find good agreement between the "signflip" noise realizations and the TOD noise realizations using our cross spectrum estimator described in Section 4.5. The noise bias

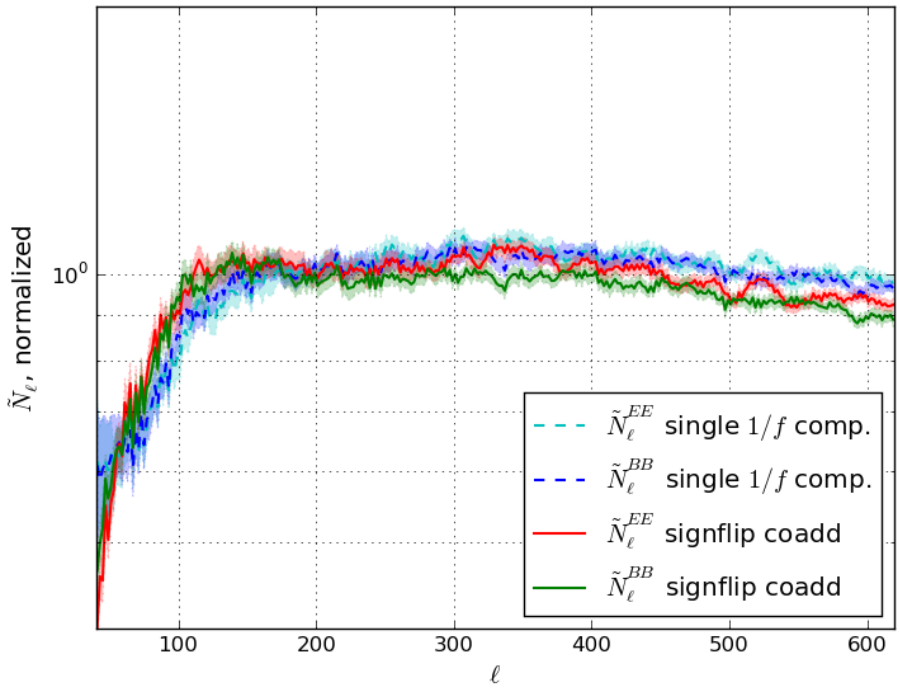

Figure 5.1: Noise bias comparison for the full data set from the TOD noise model and the signflip coaddition pipeline. We see broadly consistent results between the two noise models. The fiducial power spectra use the "signflip" noise model. These spectra do not reflect the TOD filtering and beam window function correction described in Section 4.5. The "signflip" curves are shown with these corrections in Figure 5.2. The pseudo spectra are corrected by the row sum of the mode mixing matrix to match the true ratio of E and B modes and normalized.

derived from both formalisms is shown in Figure 5.1. The full coadd and all jackknife splits described in Chapter 7 agree well except for one null test. In the "top versus bottom bolometers" split, we observe excess variance and an anti-correlation between the two halves of the data that cannot be reproduced by the simple TOD noise model. Temperature noise aliasing into the polarization frequencies in the TOD can create such a noise anti-correlation. This effect becomes more pronounced in the high-ℓ analyses.

We use the random sign coaddition pipeline to generate the noise realizations used in our fiducial jackknife null tests and error bar estimation.

5.2 Tracing the origin of low frequency noise

The Q and U knee frequency distributions differ because common mode Q and U noise are produced by different physical mechanisms. Q low frequency noise can be produced by $0f$ noise copied into the polarization TOD by the temperature-to-polarization leakage subtraction described in Section 4.4 or by spurious detector gain drifts acting on the CRHWP synchronous structure. In contrast, U is out of phase with both the CRHWP synchronous structure and temperature-to-polarization leakage, meaning that low frequency U noise requires a phase drift between the TOD and the reconstructed CRHWP angle. This can be produced by detector time constant drift.

The source of the Q common mode low frequency noise is not entirely understood, however there are several viable theories. Since Q is aligned with both the instrumental polarization and the temperature-to-polarization leakage coefficients, the noise can be either be produced by an additive (non-optical $0f$ signals copied into the polarization timestream by the leakage subtraction) or multiplicative (acting on the $4f$ CRHWP synchronous structure) mechanisms. This can be illustrated by a toy data model for the temperature to leakage subtraction similar to [52]. Assume an atmospheric brightness I, CRHWP $4f$ synchronous structure A_4, optical temperature to polarization leakage λ_4^{opt} and a non-linear detector response $g(d_{0f}) = (1 + \epsilon + g_1(d_{0f})$. The $0f$ and $4f$ TOD can be written as

$$d_{0f} = g(I + \delta_{opt})\big(I + \delta_{opt}\big) + \delta_{elec}, \tag{5.1}$$

$$d_{4f} = g(I + \delta_{opt})(Q + iU + \lambda_4^{opt} I + A_4). \tag{5.2}$$

Here instrumental non-idealities are decomposed into multiplicative gain error ϵ, additive optical signal δ_{opt}, and additive readout signal δ_{elec}. These could be effects like small signal gain drift, optics tube temperature drift, and additive readout $1/f$ respectively. Expanding these equations illustrates temperature polarization leakage,

$$d_{4f} = Q + iU + \lambda_4^{opt} I + 2A_4 g_1(I + \delta_{opt}) + A_4\epsilon. \tag{5.3}$$

The temperature to polarization leakage is removed by deprojecting d_{0f} from d_{4f}. The ϵ, δ_{opt}, δ_{elec} modes therefore couple into the polarization timestreams following

$$d_{4f,\ \text{leakage subtracted}} = Q + iU - \lambda_4^{opt}\delta_{opt} - (\lambda_4^{opt} + 2A_4 g_1)\delta_{elec} + A_4\epsilon, \tag{5.4}$$

neglecting higher order terms.

We have seen preliminary indications that the low frequency noise in the TOD originates in a time domain process by alternating the telescope scanning speed between 0.4 s^{-1} and 1.2 s^{-1} for hour long CESes. The knee frequency in the time domain remains constant between the two sets of observations. Had the origin of the low frequency noise been a result of a physical process on the sky, the knee frequency in the time domain should have shifted with the scanning speed. Conversely, this means that the impact of this low frequency noise

in the map domain can be mitigated by scanning the telescope faster thereby mapping time domain frequencies to lower ℓ values.

There is some weak evidence that the origin of the low frequency noise is due to thermal drift in the warm readout electronics. There are two plausible physical origins. The digital to analog (analog to digital) converters used to synthesize the bias lines (digitize the SQUID outputs) have a response that depends slightly on the ambient temperature. The measured amplitude of the low frequency noise is consistent with this temperature dependence acting on the ambient temperature in the read out enclosure. The second plausible explanation involves the clock used to synthesize the bias lines. The clock frequency also has a weak dependence on the ambient temperature. This causes the real frequecy of the bias lines to drift modulating the LRC resonant peak and creating fluctuations that appear in the post leakage subtraction timestreams.

We have not been able to establish a correlation between the recorded focal plane temperature and the residual low frequency noise after leakage subtraction.

5.3 Quantifying low-ℓ statistical performance

To accurately describe the low-ℓ statistical performance of POLARBEAR it is necessary to account for the effect of the TOD filtering and the beam window function in the measured noise bias. This represents the noise constribution to the statistical error bars on C_ℓ. We do this following [34] by referring the noise pseudo spectrum $\tilde{N}_\ell$ to a to a true power spectrum on the sky following Equation 4.7. We write the effective number of degrees of freedom per band power as an ℓ-dependent sky area. These two numbers represent the noise contribution to the power spectrum statistical uncertainties. Figure 5.2 show the results of this analysis.

It should be noted that the alternate auto spectrum estimator gives a marginally larger number of degrees of freedom than the cross spectrum estimator. This is likely due to imperfect mode overlap between the ten day cycles due to different map coverage and filtering. This larger number of degrees of freedom results in slightly smaller error bars on the estimated power spectrum.

5.4 Mitigation strategies for future experiments

This can be mitigated in future experiments by two main strategies: either regulating the temperature of all relevant instrument components or scanning faster on the sky. The scan speed 0.4° s^{-1} used in this analysis was chosen to cleanly separate the polarization signal ($\ell \leq 300$) from the low frequency atmospheric noise and $2f$. For POLARBEAR-2 and the Simons Array we intend to pursue both strategies. Some additional low-ℓ sensitivity can also be acheived by making the CESs longer to better orthogonalize sky and ground fixed signals.

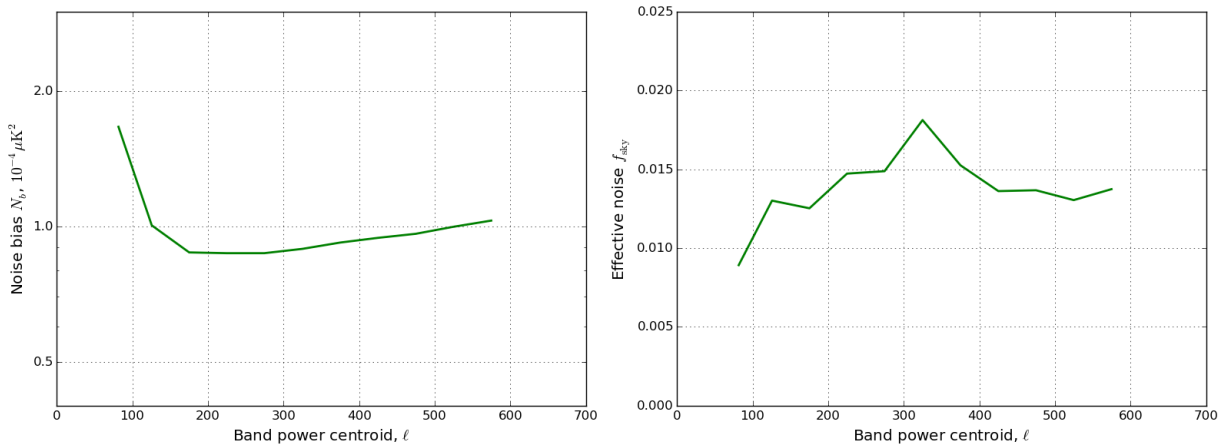

Figure 5.2: Noise bias referred to underlying sky units and number of degrees of freedom written as an effective $f_{\rm sky}$. The degradation in N_b at higher ℓ is primarily due to the beam window function and the degradation at low frequency is due to low frequency noise and timestream filtering. These curves are derived from the auto spectrum of the signflip noise realizations computed using the fiducial power spectrum pipeline. The alternate auto spectrum pipeline gives similar N_b with a marginally larger effective $f_{\rm sky}$. This plot can be directly compared to Figure 3. in [34].

Chapter 6

Absolute Calibration

This chapter describes the map domain calibration steps that we use to calibrate the overall amplitude and polarization angle of our data.

6.1 Absolute gain calibration

We perform an overall gain calibration by cross correlating our data to the Planck satellite. We use the Planck 2018 PR3 143 GHz full mission maps[3] and process them through our filtering and mapmaking pipeline. We compute debiased spectra for both the POLARBEAR internal cross spectra using the fiducial power spectrum estimate) and the fully coadded POLARBEAR maps crossed with the scanned Planck maps using the alternate auto spectrum pipeline. We fit an overall gain calibration factor based on the ratio of the E-mode spectra:

$$\hat{g}_b = \hat{C}_b^{EE,\mathrm{PB}} \;/\; \hat{C}_b^{EE,\mathrm{PB}\times\mathrm{Planck}} \tag{6.1}$$

The uncertainty on this ratio is computed by direct MC holding the underlying sky realization fixed. We use 96 realizations of the Planck FFP10 noise model [74] to approximate the Planck map noise. We fit this calibration to an ℓ-dependent gain model accounting for a smearing of the beam profile following

$$g(\ell) = g_0 \times \exp\big[-\frac{\ell(\ell+1)}{2} \times \sigma^2\big], \tag{6.2}$$

$$\hat{g}_b = \sum_\ell \mathbf{w}_{b\ell} g_\ell. \tag{6.3}$$

We find an overall gain calibration factor of 1.08 ± 0.04 in amplitude and an effective beam smearing of $\sigma^2 = 1.14 \pm 5.58$ amin^2. Since the absolute gain calibration shows no statistical preference for a non-zero pointing model error we simply convolve the beam with the best fit value for the beam smearing. We compute an alternate gain calibration fitting

[3] `https://pla.esac.esa.int`

the POLARBEAR spectrum to the ΛCDM theory spectrum and find agreement at the percent level across our ℓ range.

After applying this absolute calibration we compare E-mode spectrum to Planck and form a null spectrum.

$$\hat{C}_{b,\mathrm{null}} = \hat{C}_b^{EE,\mathrm{PB}} - \hat{C}_b^{EE,\mathrm{PB}\times\mathrm{Planck}} \tag{6.4}$$

The uncertainty on this null spectrum is computed by direct MC simulation. We find this null spectrum to be consistent with zero with $\chi^2/\nu = 7.0/9$ corresponding to a probability-to-exceed (PTE) of 64%. When we compare our measured E-mode spectrum to the best fit ΛCDM theory, we observe a marginally significant discrepancy in our highest two ℓ bins. This appears to be due to an anisotropic feature seen in the two-dimensional power spectrum at approximately the size scale and orientation of the detector wafers. These fluctuations have no significant counterpart in the jackknife null tests described in Chapter 7. These fluctuations appear to not depend on any of the operations in the TOD filtering and mapmaking pipeline that have characteristic scales on the sky or frequencies in the time domain. The overall gain and beam calibration does not significantly shift if these two bins are removed from the analysis. We find that there is no significant shift in the B-mode spectrum when these regions of the Fourier plane are masked in the pseudo spectrum. We show our measured E-mode spectrum as well as the residuals compared to Planck and the ΛCDM theory in Figure 6.1.

6.2 Absolute polarization angle calibration

After applying the overall gain calibration we self calibrate the overall instrument polarization angle following [65]. We apply an overall polarization angle correction $\Delta\psi$ such that the measured C_ℓ^{EB} power is minimized.

$$-2\ln(\mathcal{L}) = \sum_b \left[\frac{\hat{C}_b^{EB} - \frac{1}{2}\sin(4\Delta\psi)\sum_\ell \mathbf{w}_{b\ell} C_\ell^{EE}}{\Delta\hat{C}_b^{EB}} \right]^2 \tag{6.5}$$

We find an overall calibration $\Delta\psi = -0.61^\circ \pm 0.22^\circ$. After applying this calibration we find that $\hat{C}_b^{EB}$ is consistent with zero with a total χ^2 PTE of 77%. Our absolute angle calibration is compatible with the two season small patch analysis which reported $\Delta\psi = -0.^\circ 79 \pm 0.^\circ 16$. This calibration is shown in Figure 6.2.

It should be noted that the correction to the B-mode spectrum is proportional to the E-mode spectrum and the square of the polatization angle error. For this analysis the uncertainties due to the absolute polarization angle calibration are negligible compared to the statistical errors.

The self-calibrated polarization angle correction is applied in the map domain. The overall gain computed by matching the EE spectrum to Planck differs slightly from the MC simulations used to establish the band power errors and covariances. To account for this,

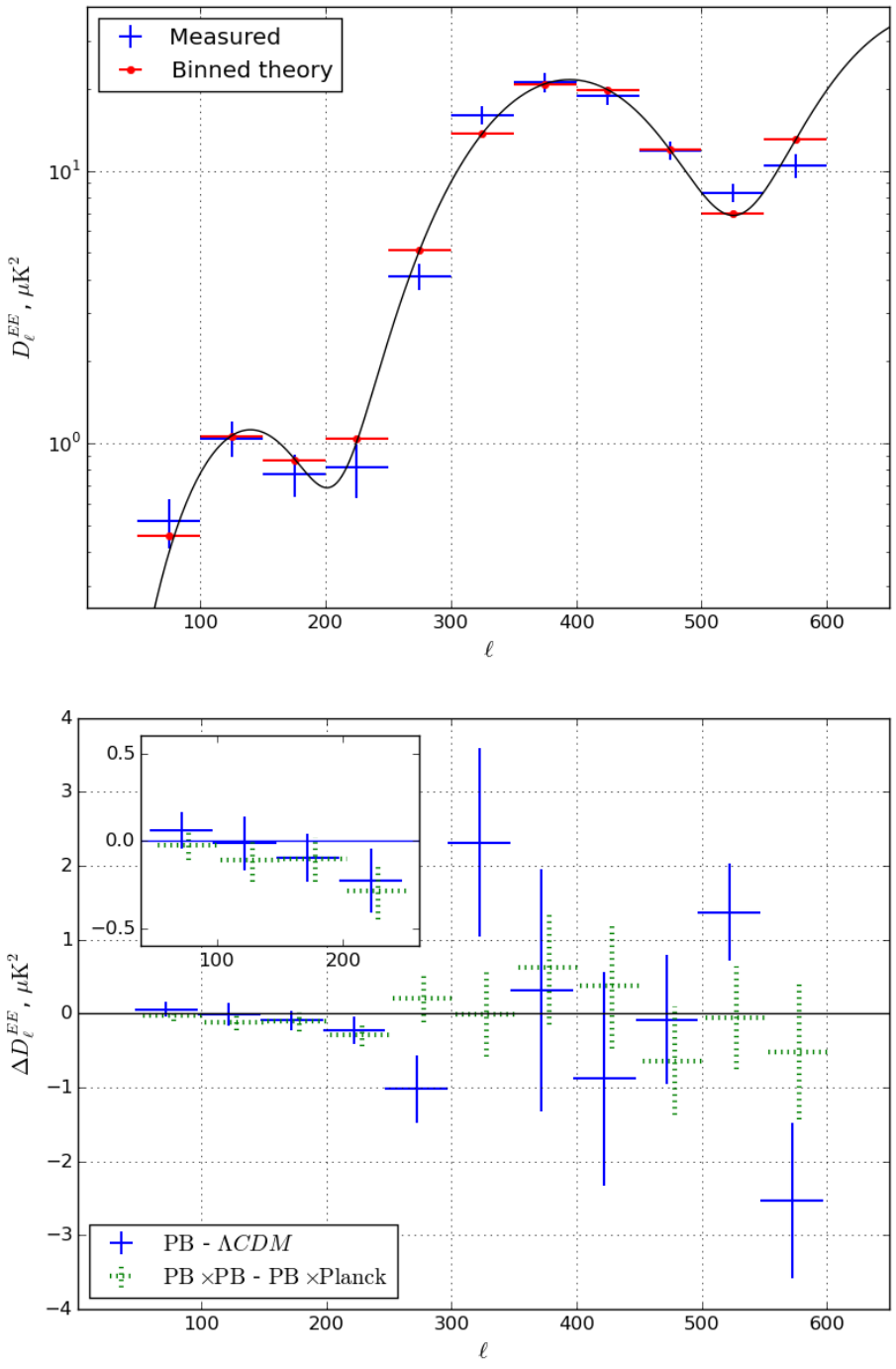

Figure 6.1: The E-mode bandpowers after absolute gain calibration compared to the best fit Planck 2018 ΛCDM cosmology are shown in the left panel. The E-mode spectrum is used as an overall gain and beam width calibration. The residuals compared to the binned theory and the null quantity formed by subtracting the debiased cross spectrum with filtered Planck 2018 143 GHz maps are shown in the right panel. The lowest four bandpowers are shown in the inset.

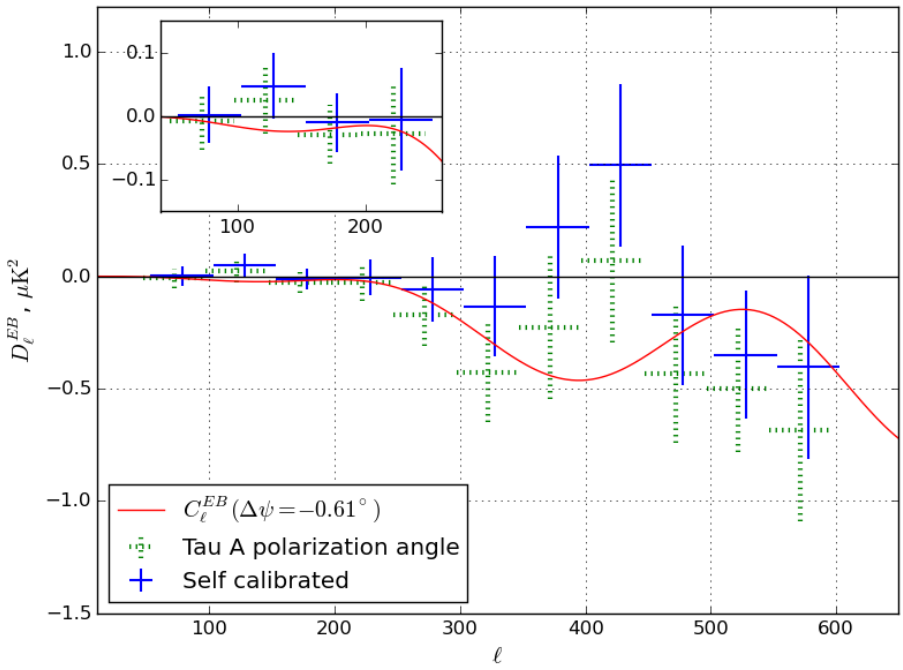

Figure 6.2: EB power spectrum before and after polarization angle self-calibration. We find the angle derived from setting $C_\ell^{EB} = 0$ to be statistically consistent with PB17. We find our measured EB spectrum to be consistent with zero after an overall polarization angle is subtracted with $\chi^2/\nu = 6.56/10$ corresponding a 77% PTE. The lowest four bandpowers are shown in the inset.

we assume that the total variance in each band power is the sum of the signal variance and the noise variance as derived from signal-only and noise-only simulations, respectively. The noise variance is rescaled to the best fit absolute gain calibration. We quantify a calibration uncertainty in the measured power spectrum using the uncertainty in the overall gain calibration g_0, pointing model error σ^2, and polarization angle self calibration $\Delta\psi$. The correlation between g_0 and σ^2 is modeled as a simple Gaussian covariance.

Chapter 7

Null tests

This chapter describes the null test framework and results for the low-ℓ analysis. The null tests are an essential internal consistency check that is sensitive to a wide range of forms of systematic contamination. The null tests are usually developed in parallel with the data selection and TOD filtering pipeline described in Chapter 4.

7.1 The null test framework

We perform a set of null tests to establish the internal consistency of the dataset and search for possible systematic contamination in the final power spectra. In general, it is not possible to construct difference maps between halves of the data with zero signal due to anisotropic scanning and filtering effects. This effect becomes particularly pronounced at low-ℓ. As a result, we follow the formalism developed originally by the QUIET collaboration [75, 76] and used in previous PB analyses. We include the filtering and mode mixing explicitly in the construction of the null spectrum:

$$\hat{C}_\ell^{\rm null} = \hat{C}_\ell^A + \hat{C}_\ell^B - 2\hat{C}_\ell^{AB}, \tag{7.1}$$

where $\hat{C}_\ell^A$ and $\hat{C}_\ell^B$ ($\hat{C}_\ell^{AB}$) are the debiased autospectrum for each half of the split (the cross spectrum between the splits). The spectra are computed using the same cross spectrum formalism and map bundles used in the main pipeline.

The same null spectra computed both using the cross spectrum formalism and the map difference formalism in Figure 7.1. The map difference case shows imperfect signal cancellation which makes the null spectrum somewhat sensitive to the underlying signal spectrum.

The filter transfer function and mode mixing matrix are computed in the same way as the fiducial power spectrum pipeline using 92-EE only and 92-BB only Planck 2018 ΛCDM input maps for each test. Only map regions present in both halves of the split are used to

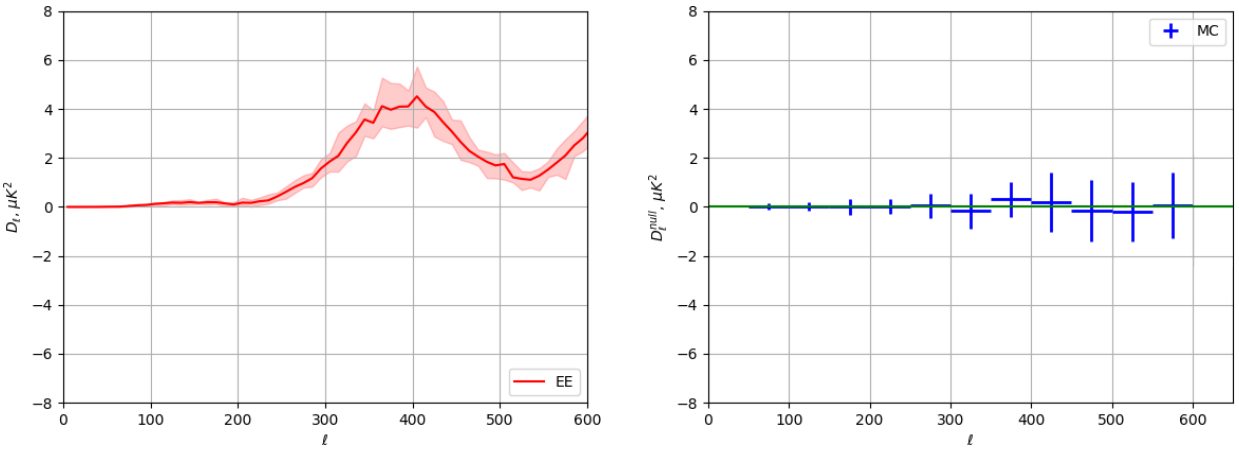

Figure 7.1: The same (EE) null spectrum computed with the map difference formalism (left) and the cross spectrum formalism (right). The imperfect signal cancellation can be seen in the map difference spectrum by the characteristic E-mode acoustic peaks.

form the pseudospectrum and mode mixing matrix meaning that a separate mode mixing calculation is done for each null test split. The null spectra are computed using the same ℓ binning as the final power spectrum. EE, EB, and BB null spectra are compared to 192 $EE + BB$ signal and noise simulations. These simulations are built by filtering input signal realizations and adding the "signflip" noise realizations in the map domain. We find that this number of simulations is adequate for percent-level statistical uncertainties on the null spectrum PTE values and filter transfer functions across our full ℓ range. The number of signal-only simulations necessary to estimate the filter transfer function was computed by calculating a filter transfer function for several simulated skies individually and then applying the central limit theorem to estimate the uncertainty on the average. The number of signal and noise simulations was determined to accurately differentiate a PTE of 5% from 0% by directly simulating the binomial distribution. There is an additional requirement on the number of signal and noise simulations necessary to acheive sufficient statistical precision on the MC error bar estimates.

For our fiducial null test statistics, we use noise realizations generated with the "signflip" pipeline. There is no significant difference from the PTE values computed with the TOD noise model with the exception of the "top versus bottom" null test that explicitly separates detector pairs. This is due to the presence of an additional anticorrelated noise term when detector pairs are separated that is not included in the TOD noise model described in Chapter 5.

7.2 Choosing null test splits

We split the data along 18 largely uncorrelated axes designed to probe a wide range of possible sources of systematic contamination. Where possible the data set is split into halves with equal weight.

- "First half versus second half": the dataset is split into two equal-weight halves chronologically to probe for time dependent miscalibration or changes in the instrument.
- "Rising versus middle and setting", "middle versus rising and setting", "setting versus rising and middle": the three different CES types are split in all possible combinations to detect elevation-dependent miscalibration or residual ground synchronous signal.
- "Left-going versus right-going subscans": the dataset is split in half according to the direction of motion of the telescope to test for microphonic or magnetic pickup in the data.
- "High gain versus low gain observations": the dataset is split into observations with above and below average mean detector gain coefficients (in K / ADC) to search for problems with the gain calibration.
- "High PWV versus low PWV": the dataset is split by PWV as measured by the nearby APEX radiometer to check for loading or weather dependent effects. Data where PWV measurements are not available are included in the "high PWV" half of the split.
- "Common mode Q knee frequency", "common mode U knee frequency": the dataset is split into observations with high and low knee frequencies in the telescope frame Q and U common mode signal to check for problems in the treatment of low frequency contamination. The Q knee frequency split overlaps with the cloud detection criteria from [66]. Both splits are uncorrelated with the PWV split. This suggests that the residual low frequency noise described in Chapter 5 is not atmospheric in origin.
- "Mean temperature-to-polarization leakage by channel": split the dataset into detectors that see small and large temperature leakage coefficients to test the subtraction and search for residual contamination.
- "$2f$ amplitude by channel", "$4f$ amplitude by channel": split the data by CRHWP signal amplitude to check for problems removing the CRHWP structure or systematic contamination coupling into the data through the CRHWP synchronous structure.
- "Q versus U pixels": each detector wafer is fabricated with two sets of polarization angles. We split the data into the two pixel types to check for problems in the device fabrication.
- "Sun above or below the horizon", "Moon above or below the horizon": we split observations based on whether or not the sun or moon is up to check for sidelobe contamination.

- "Top half versus bottom half", "left half versus right half": we split detectors by the boresight axis of the telescope to check for optical distortion and sidelobe contamination.
- "Top versus bottom bolometers": with a CRHWP each bolometer TOD is an independent polarization measurement. We explicitly separate detector pairs to check for aliasing systematics or device mismatch.

We have also considered season-by-season data splits, however these are not included in the final suite because they are highly correlated with the first half versus second half split. Additionally, we have examined average $2f$ and $4f$ amplitudes, as well as average temperature to polarization leakage by observation but do not include these due to redundancy with the weather and gain splits. We consider sun and moon boresight distance splits but do not included them due to overlap with the sun and moon being above the horizon. None of the excluded splits indicated significant problems and removing redundant tests improves sensitivity to outliers in the splits used. The correlation coefficients between the null tests are shown in Figure 7.2.

7.3 Defining null test statistics

For each bin in each null spectrum we compute the statistic $\chi_{\rm null} \equiv \hat{C}_b^{\rm null}/\sigma(\hat{C}_b^{\rm null})$ where $\sigma(\hat{C}_b^{\rm null})$ is the standard deviation of the MC null spectra. We use both $\chi_{\rm null}$ and $\chi^2_{\rm null}$ because the former is sensitive to systematic biases and the latter is the more sensitive to outliers. Figure 7.3 shows the $\chi_{\rm null}$ and $\chi^2_{\rm null}$ distributions compared to the expectation from MC simulations. It should be noted that the distribution of the band powers is not expected to be exactly Gaussian as the null spectrum is defined as a difference of reduced χ^2 distributions. To probe for systematic contamination and consistency of the data with the simulations we compute five statistics on the $\chi_{\rm null}$ values.

1. "Average χ overall": the mean value of $\chi_{\rm null}$ for all tests and bins
2. "Most extreme χ^2 by bin": the most extreme $\chi^2_{\rm null}$ when summing spectra over tests
3. "Most extreme χ^2 by test": the most extreme $\chi^2_{\rm null}$ when summing spectra over bins
4. "Most extreme χ^2 overall": the most extreme $\chi^2_{\rm null}$ for all bins and tests
5. "Total χ^2 overall": the sum of χ^2_{null} for all spectra

For each statistic we compute a PTE by comparing the real data to same statistic computed with the MC realizations. In this way the correlation structure between the bins and the tests is taken into account. It is possible to perform this analysis by assuming that the null spectrum band powers are Gaussian distributed with a covariance matrix estimated from

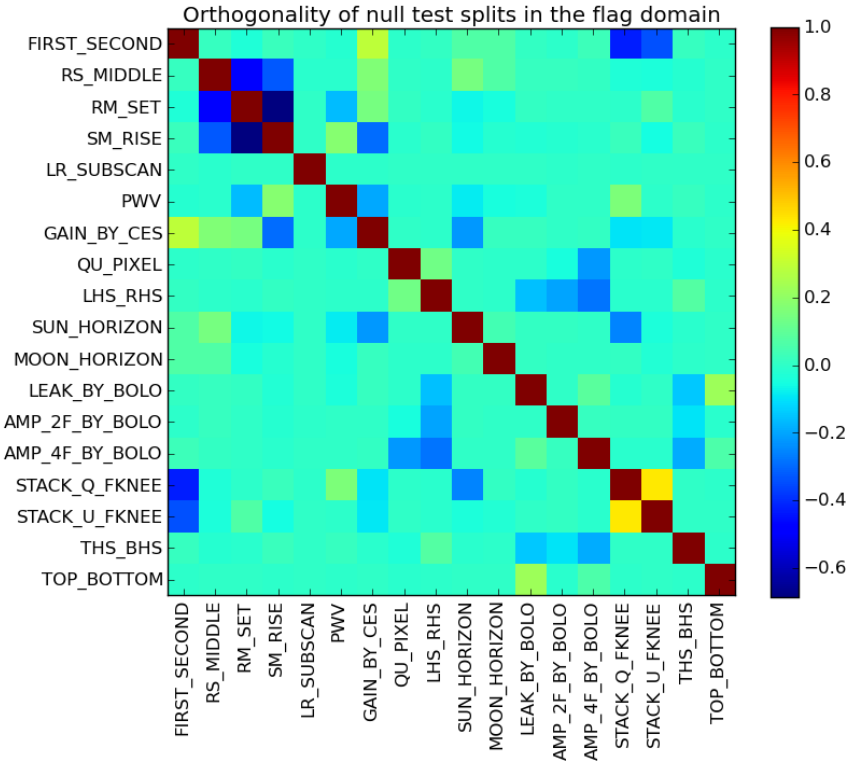

Figure 7.2: Correlation coefficients between the null test splits defined in the data flag domain. The strongest correlation between the splits included in the final analysis comes from the CES type splits.

the simulations. The null statistic PTE values can then be computed by sampling from this multivariate Gaussian distribution. While this is not used in our result, this approach can be used as a diagnostic in early iterations of the null test pipeline when it is not efficient to run large numbers of simulations.

The PTE of the total $\chi^2_{\rm null}$ summed over ℓ bins for each test and summed over tests for each bin is shown in Table 7.1. These numbers are computed directly from the MC simulation set so the PTE values are quantized.

We define an overall statistic $P_{\rm low}$ that is the lowest of the five PTE values. We require that the PTE of $P_{\rm low}$ be greater than 5%. The numerical value for these statistics can be seen in Table 7.2. All polarization spectra (EE, EB and BB) independently pass this test.

We also require that the PTE of the $\chi^2_{\rm null}$ values by test, by bin and overall be consistent with a uniform distribution using a KS test to test for systematic mismatch between the real and simulated uncertainties. Figure 7.4 shows the PTE distribution for all bins and tests. We find the PTE distributions to be consistent with uniform.

7.4 Null test results

All of the polarization spectra pass null tests pass with no significant outliers in the bins, spectra, or overall.

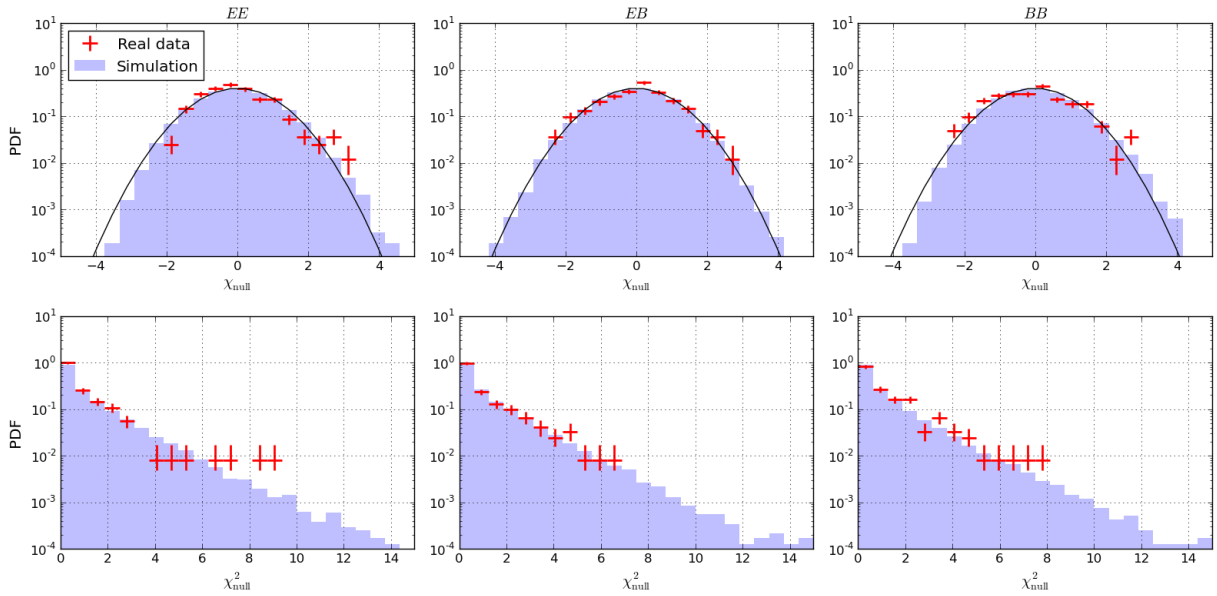

Figure 7.3: One dimensional $\chi_{\rm null} = C_{\rm null}/\sigma_{\rm null,MC}$ distribution from the fiducial set of jackknife splits. No statistically significant outliers are seen in these statistics. Error bars on the real data points represent 68% Poisson confidence intervals. The solid line in the upper panels represents a unit variance Gaussian distribution.

	EE χ^2 **PTE**	EB χ^2 **PTE**	BB χ^2 **PTE**
Null test summed over ℓ bins			
First half versus second half	86.5 %	43.2 %	79.7 %
Rising versus middle and setting	85.4 %	70.8 %	6.8 %
Middle versus rising and setting	63.0 %	63.0 %	39.1 %
Setting versus rising and middle	50.5 %	53.1 %	19.3 %
Left versus right-going subscans	36.5 %	26.0 %	6.2 %
High gain versus low gain CESs	45.3 %	83.3 %	3.1 %
High PWV versus low PWV	50.5 %	33.9 %	28.6 %
Common mode Q f_{knee}	57.8 %	36.5 %	26.6 %
Common mode U f_{knee}	91.7 %	54.7 %	79.7 %
Temperature leakage by detector	78.6 %	54.2 %	56.8 %
$2f$ amplitude by bolometer	5.7 %	32.8 %	83.9 %
$4f$ amplitude by bolometer	35.4 %	18.2 %	33.3 %
Q versus U pixels	72.4 %	64.6 %	28.1 %
Sun above or below the horizon	76.6 %	91.1 %	32.2 %
Moon above or below the horizon	76.0 %	77.6 %	57.3 %
Top half versus bottom half	79.7 %	35.4 %	27.1 %
Left half versus right half	53.6 %	33.9 %	76.0 %
Top versus bottom bolometers	36.5 %	55.7 %	35.4 %
ℓ bin summed over null tests			
$50 < \ell \leq 100$	31.8 %	58.3 %	44.8 %
$100 < \ell \leq 150$	64.1 %	14.1 %	24.5 %
$150 < \ell \leq 200$	61.5 %	46.9 %	96.9 %
$200 < \ell \leq 250$	71.4 %	74.0 %	28.6 %
$250 < \ell \leq 300$	83.9 %	7.3 %	26.6 %
$300 < \ell \leq 350$	50.5 %	92.7 %	6.8 %
$350 < \ell \leq 400$	64.1 %	97.9 %	92.2 %
$400 < \ell \leq 450$	44.3 %	84.4 %	5.2 %
$450 < \ell \leq 500$	96.9 %	63.5 %	3.1 %
$500 < \ell \leq 550$	68.8 %	84.5 %	49.0 %
$550 < \ell \leq 600$	49.5 %	16.1 %	49.5 %

Table 7.1: PTE values for the total χ^2 of each null spectrum summed over ℓ bins and each ℓ bin summed over null spectra. None of the null spectra indicate significant problems. These PTE values are computed directly from the 192 signal+noise simulations.

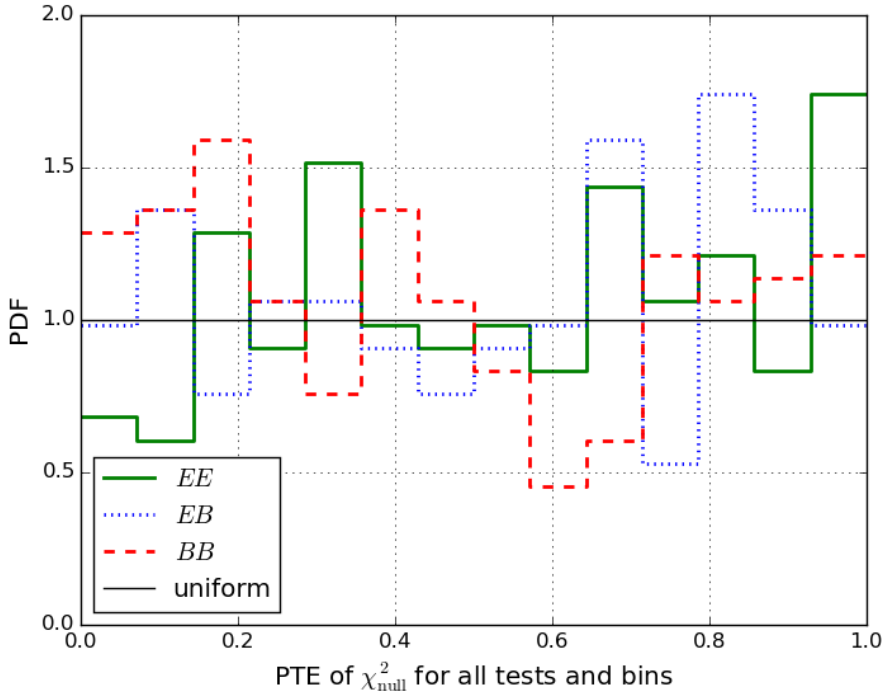

Figure 7.4: Distribution of PTE values for each bin in each test. The distribution for all three spectra are consistent with uniform.

Null statistic	*EE* PTE	*EB* PTE	*BB* PTE
Average χ overall	73.4 %	80.7 %	9.9 %
Most extreme χ^2 by bin	96.9 %	43.8 %	31.7 %
Most extreme χ^2 by test	70.3 %	98.4 %	57.3 %
Most extreme χ^2 overall	48.4 %	84.9 %	66.1 %
Total χ^2 overall	90.6 %	78.7 %	12.5 %
Lowest statistic	85.4 %	86.4 %	33.9 %
KS test on all bins	10.1 %	60.4 %	15.9 %
KS test on all spectra	6.4 %	31.8 %	10.5 %
KS test overall	35.9 %	27.5 %	14.6 %

Table 7.2: PTE values for each of the high level null test statistics.

Chapter 8

Simulating Systematic Contamination

Systematic error simulations serve as an important cross check to the null tests. A well designed set of null tests will be sensitive to a large number of potential problems. However, there are several fundamental limitations of the null test paradigm.

- Null tests only provide a binary piece of information: they pass or they do not. This means that either $\Delta C_{\ell,\mathrm{syst}} \lesssim \Delta C_{\ell,\mathrm{stat}}$ (null tests pass) or $\Delta C_{\ell,\mathrm{syst}} \gtrsim \Delta C_{\ell,\mathrm{stat}}$ (null tests fail). A more nuanced understanding can be useful.
- The null tests are fundamentally limited by the trials factor imposed by the number of null splits. A typical experiment will define ∼10-20 null splits. This results in a significant trials factor when searching for outliers. A 3σ fluctuation is not surprising out of ∼200 band powers across all splits. This means that the null tests may not be sensitive to systematic errors that are similar to the statistical errors unless they appear coherently between splits or ℓ bins.

Systematic error simulations can address these a bit more directly and estimate the contribution to the power spectrum uncertainties beyond the statistical errors. The systematic simulations can provide information on problems that may not appear in the null tests at current sensitivities but will become problems for future instruments. Finally, the systematic simulations can constrain certain effects that cannot be seen in the null tests. One such example is the mismatch between temperature and polarization beams produced by detector crosstalk in a CRHWP experiment described in Section 8.5.

There are two general philosophies about estimating systematic errors that are used in the field. They can be described as treating the systematic simulations as an error in the limit of no detector noise, i.e. the systematic contamination is injected in the time or map domain into signal-only simulations and the difference to a reference set of simulations is counted as a systematic error. This is done for the previous POLARBEAR science analyses and is the main approach taken for this analysis. The second method is to treat the systematic contamination as an error propagation problem and inject a model of the systematic into the real TOD. The systematic error is then taken to be the amount that the systematic injection

changes the resulting output spectrum. In this way the systematic contamination acts on both the signal and the noise in the real TOD. This is how a number of systematic effects are simulated in the ABS results paper [35].

To make this discussion concrete, imagine the case of a noisy measurement of the detector gains. The former approach will answer the question "What is the best measurement that can be done with this level of precision on the detector gains?" whereas the latter approach will answer the question "How much does imperfect knowledge of the detector gains add to the power spectrum errors for *this dataset*?" In general the latter approach will quote a larger amount of systematic contamination.

8.1 Pipeline overview

The systematic error estimate uses a modified version of the simulation pipeline developed for the jackknife null tests and the power spectrum estimation. For most systematic effects, a signal-only ΛCDM sky is scanned to form signal-only TOD. These TOD are then distorted following a model of the given effect and then filtered and projected onto the sky using the fiducial mapmaker. We compute pseudo spectra from these distorted maps and refer them to the underlying sky using the fiducial power spectrum estimation pipeline. Since several systematics are suppressed by the absolute gain and polarization angle calibration, we apply these overall calibrations to each simulation. We do not model the ℓ dependent gain model applied to the real data and only fit the overall gain g_0. This will conservatively overstate several effects including boresight pointing uncertainty. In parallel, the same mapmaking and power spectrum estimation is performed without distorting the TOD to form a reference simulation. The systematic error is taken to be the absolute difference between the contaminated and reference power spectra.

8.2 Gain miscalibration, time constant drift, and detector non-linearity

We simulate the error introduced by finite uncertainty on the relative gain calbration of each detector acting on the underlying CMB signal. We estimate the statistical uncertainty in each bolometer relative gain calibration 4.7% due to the amplitude of the chopped thermal source and detector noise.

The primary impact of detector non-linearity is the additive temperature to polarization leakage, however there is a smaller multiplicative term from the gain variation acting on the CMB signal. As shown in [52] the majority of the $4f$ amplitude drift is due to detector non-linearity. We simulate this using a downsampled version of the normalized $4f$ amplitude (phase) as a tracer of the detector small signal gain (time constant) and inject the non-linear

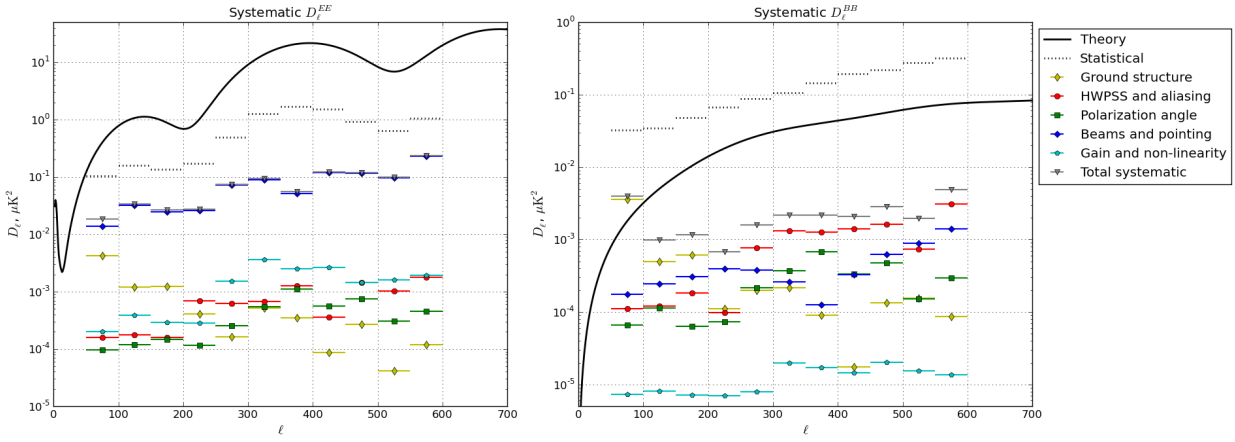

Figure 8.1: Systematic contributions from all simulated effects grouped thematically. The dominant effect in EE is the misestimation of the effective polarization beam due to detector crosstalk while the dominant systematic in BB is the uncertainty in the ground structure subtraction. It should be noted that this is a conservative estimate driven by significant model uncertainties. Future experiments will be able to suppress this effect significantly through careful study and control of ground synchronous structure. The total systematic error is formed assuming all systematics add linearly in power.

response (time dependent polarization angle error) into the simulation timestreams. The resulting contamination is expected to be negligible.

8.3 Polarization angle error

We estimate the impact on the reconstructed power spectrum assuming that the calibrated detector polarization angle errors are Gaussian distributed around the true values with standard deviation 1.°2. This uncertainty is taken from the scatter of the difference in polarization angles measured for the two detectors within a pair. This polarization angle uncertainty is comparable to the value used in the POLARBEAR small patch analyses. This systematic effect is strongly suppressed by the absolute polarization angle calibration. We also estimate the effect of an overall polarization angle miscalibration by rotating the polarization angle of the input sky 0.°5 RMS based on the quoted systematic uncertainty in the Tau A polarization angle from [63]. The residual error from an overall polarization angle shift is not identically zero after polarization angle self calibration because the common mode deweighting filter has different spectral shapes for ground coordinate Q and U and is therefore not invariant under a global polarization angle rotation.

8.4 Boresight pointing error

We quantify the systematic impact of the imperfect knowledge of the boresight pointing. We consider several candidate pointing solutions as described in 3.4. We perform the input map scanning with the fiducial pointing model and project the TOD to the sky with an alternate pointing solution.

We find the largest discrepancy from the fiducial pointing solutionresults from the inclusion of Jupiter data in the pointing model fit. This is potentially due to fact that the Jupiter data points cover a significantly different range of aximuth and elevation compared to the other radio pointing scans. We conservatively quote that residual in our systematic error estimate. This is one of the largest systematic uncertainties in our E-mode spectrum, however the effect is significantly less than our statistical error over this ℓ range and is negligibly small in the B-mode spectrum. The ℓ dependent gain calibration will suppress this effect by fitting out the beam smearing due to pointing model error, however this additional supression is not included in our systematic error estimate.

8.5 Detector crosstalk

We observe an electrical coupling between detectors read out on the same cables. We assume that this crosstalk is constant through the entire dataset and linear. We estimate the amplitude of this effect using the observations of Jupiter used for the gain and beam calibration. Crosstalk appears in the individual detector Jupiter maps as an apparent negative copy of the beam shape several tens of arcminutes away from the main beam. In previous POLARBEAR papers we used an estimate of this effect based on lab tests and a naive model wherein only the nearest neighbors in multiplexing frequency on the same read out cables crosstalked to each other. In this analysis we directly estimate the crosstalk mixing matrix from the Jupiter scans and allow for arbitrary crosstalk between detectors located on the same read out cables. By visual examination of the maps we do not see crosstalk between detectors located on different read out cables. We estimate the amplitude of these images using a matched filter and construct a matrix $\mathbf{L}$ representing the transformation of real signal in bolometer j to observed signal,

$$d_{j,\mathrm{observed}} = d_{j,\mathrm{real}} + \sum_{i \neq j} \mathbf{L}_{ij} d_{i,\mathrm{real}} \tag{8.1}$$

We fit for the components of $\mathbf{L}$ for detectors read out on the same cables using a matched filter on the individual detector maps. The median non-zero off-diagonal element of the matrix $\mathbf{L}$ is 1% and the median row sum representing the ratio of cross talked power to power in the main beam is approximately 4%. We estimate the systematic error from detector cross talk as the sum of two effects. We first quantify error introduced in the beam calibration. This is due to the fact that crosstalk is strongly suppressed in polarization due to the polarization angles of each detector [57] in CRHWP experiments. As a result

the temperature and polarization see different effective beam profiles. We also estimate the distortion of the polarization signal due to this effect by injecting the effect at the TOD level in signal-only simulations. We find the beam miscalibration term to be the dominant systematic in our E-mode spectrum. It is possible to strongly suppress this effect by inverting the mixing matrix $\mathbf{L}$ in the data processing pipeline as done in [26], however we do not perform this step as the expected contamination is already below our statistical error.

Finally, it should be noted that crosstalk is generally more problematic in pair differencing experiments because it mixes $T \rightarrow B$ whereas in a CRHWP experiment crosstalk only mixes $E \rightarrow B$. This is a natural consequence of the fact that in a CRHWP experiment intensity and polarization are separated in time domain frequency.

8.6 Ground synchronous structure

We observe a ground-fixed structure in the time ordered data that is on the order of 100 μK after subscan polynomial filtering. The vast majority of this structure is subtracted to by binning each detector TOD in azimuth and subtracting that mode for each CES observation. This structure is possibly due to optical far sidelobes hitting the surrounding terrain, however we have never been able to specifically confirm this. Any slow variation of this structure within a CES will appear as a red spectrum contamination in the power spectra. Given that the size of the structure (without subtraction) is substantially larger than our expected signal at low-ℓ it is important to carefully consider imperfect subtraction. We simulate possible variation in this ground-fixed structure within each CES observation and estimate the impact of the residual on the final B-mode power spectrum. We find this to be the dominant source of possible systematic contamination in our lowest ℓ bins of the B-mode spectrum. This systematic may be a critical issue for future experiments.

One physically motivated model for this effect is the detector non-linearity modulating stable ground pickup. We simulate this using the low-pass filtered $4f$ amplitude as a gain tracer. This time dependent gain will modulate the ground synchronous structure producing imperfect subtraction. This mode *should* exist in the data, however it may not be the dominant form of contamination due to ground structure. In principle it is possible to project this out by performing a linear least squares fit for the ground synchronous structure in each azimuth bin as a function of the $4f$ amplitude. In practice it may be more productive to work on improving the telescope shielding if this model becomes important.

In addition to the detector gain model, we simulate several linear drift models of instability in the ground template. This is intended to be a very general parameterization of ground fixed structure drift. We assume that the ground synchronous signal is being modulated by some function of time during the observations. In the limit that this amplitude drift can be described as red spectrum noise or a slow drift the linear mode will dominate. It should be noted that this model is agnostic to what is causing the apparent ground structure amplitude to drift. This model can be parameterized by the statistics of the drift slope within an ob-

servation, i.e. the difference in apparent ground structure brightness between the beginning and the end of a CES.

We place an upper limit on this models using the TOD directly. For each bolometer and observation type (rising, middle, and setting) we fit $Q + iU$ for each subscan as a tenth order Legendre polynomial series. We then average these coefficients across all observations to build a set of polarization templates for the ground synchronous structure. The TOD is then fit to this template for each subscan and averaged across detectors to estimate an amplitude as a function of subscan number within an observation. The slope of this amplitude is then estimated for each observation using a linear least squares fit. We do not see any correlation of the ground amplitude or the slope of the amplitude with local solar or sidereal time and place an upper limit of 1% drift correlated with solar time. We simulate coherent temperature drift in the ground synchronous signal (i.e. the ground synchronous structure getting brighter in every scan) at the percent level as an approximation for this effect.

We also expect that the ground structure amplitude will drift within an observation uncorrelated with solar or sidereal time. We place a conservative upper limit by considering all of the of the variance in the ground structure amplitude slope. In an ideal experiment with prefectly stable ground synchronous structure the TOD noise will produce non-zero apparent amplitude drift. In other words, this systematic error estimate counts some detector noise and should be thought of as an upper limit. This signal looks primarily like a red spectrum noise in the map domain and is somewhat suppressed by the cross spectrum estimator. We estimate the residual seen in our fiducial cross spectrum estimator. It should be noted that this represents the maximum contamination from this model that is consistent with the data. The majority of the combined ground synchronous structure systematic error estimate comes from this mode.

We also validate that the null tests are indeed sensitive to these models of drift in the observe ground signal amplitude. Statistically significant contamination due to imperfect ground template subtraction results in null test failures confined to the lowest ℓ bin of the CES type (rising, middle, setting) and half focal plane (left versus right and top versus bottom) splits. A constraint on the maximum drift compatible with the data can also be derived from the fact that no null test failures are observed, however this is significantly less sensitive than the template approach. The null tests, however, are significantly more model independent in that the contamination need not exactly follow the models described here. Since no null test failure is observed we can be confident that this systematic is indeed subdominant to our statistical errors.

8.7 HWP signal aliasing

An additional source of variance in the polarization data is produced by the imperfect separation of temperature and polarization in time domain frequency. While small, the (beam-convolved) temperature signal on the sky will have power that aliases into the polarization band centered on the $4f$ line. Additionally, there is non-zero leakage of the temperature

signal into the sidebands of the CRHWP $2f$. We simulate these effects by scanning a temperature-only beam convolved sky and injecting the aliased signal at the 0.6% level via the $2f$ and directly via the $0f$ into the polarization TOD. We find the contamination in both the EE and BB spectra to be negligible.

8.8 HWP imperfections

We observe a small air bubble in the anti-reflection coating on our CRHWP. We find the CRHWP synchronous structure associated with this spot to be stable with time. We simulate this component of the CRHWP synchronous structure combined with detector non-linearity, time constant drift, and gain error. We find the excess variance in the power spectra to be negligible.

8.9 Combined systematic error estimates

There are several viable ways to combine the systematic errors from different effects. These can be described as followed.

- Paranoid: Systematic effects are correlated on a mode-by-mode basis, meaning the combination follows $(\Delta C_{\ell,\mathrm{syst}})^{1/2} = \sum_{\mathrm{effects}} (\Delta C_\ell)^{1/2}$
- Conservative: Systematic effects all add power but are not correlated on a mode-by-mode basis, meaning $\Delta C_{\ell,\mathrm{syst}} = \sum_{\mathrm{effects}} \Delta C_\ell$
- Uncorrelated: Systematic effects are all variance in the power spectrum estimate and therefore add in quadrature, $\Delta C^2_{\ell,\mathrm{syst}} = \sum_{\mathrm{effects}} \Delta C^2_\ell$
- Simulated jointly: All systematic errors are included in one set of simulations. This is how the Planck FFP10 simulations are done, see Appendix A of [74].

To form an overall systematic error estimate we follow the conservative approach and linearly add the power spectrum contamination from each set of simulations. This is how the combination was done for the previous POLARBEAR analyses. In practice we expect that each source of error will be largely uncorrelated meaning this is a conservative upper limit. The total systematic error estimate as well as the contributions from individual effects for EE and BB are shown in Figure 8.1.

Chapter 9

Results

9.1 The POLARBEAR auto spectrum

The POLARBEAR B-mode power spectrum is shown in Figure 9.1. We observe a modest excess above the ΛCDM lensing expectation in our lowest two ℓ bins. We find the statistical error be dominant in all ℓ bins.

We compute an estimate of the overall amplitude of our observed B-mode signal relative to previous work. We assume that the underlying sky consists of a lensing CMB component corresponding to the Planck 2018 ΛCDM lensing B-mode spectrum and a foreground component modeled by a power law $D_{\ell,\mathrm{dust}} = 9 \times 10^{-3}\ (\ell/80)^{-0.6}\ \mu\mathrm{K}^2$ taken from the BICEP2 and *Keck Array* measurement of the same patch of sky [34]. We find a reduced χ^2 of 11.6/11 compared to this model indicating good agreement. Naively fitting for an overall B-mode amplitude for this model we find $A_{BB} = 1.8 \pm 0.8$ disfavoring the null BB hypothesis at 2.2σ. This estimate neglects the slightly non-Gaussian shape of the band power distributions, however that is accounted for in our cosmological parameter constraints shown in subsequent sections.

The absolute calibration used in the simulations differs slightly from the final absolute calibration of the real data. This is accounted for in the band power errors by taking the total variance to be the sum of the noise variance and the signal variance. The noise variance is rescaled to match the final calibration. The difference between this approach and naively rescaling the simulation error bars by the absolute gain calibration is negligible due to the fact that the CMB sample variance contribution is small.

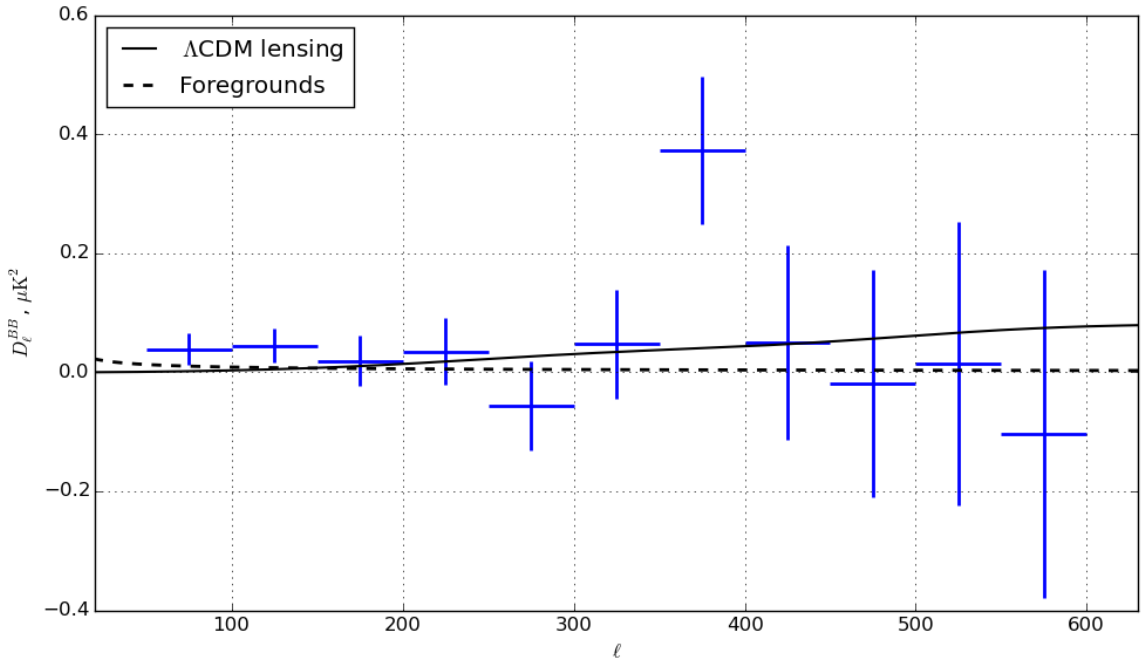

Figure 9.1: Measured B-mode spectrum using the fiducial cross spectrum pipeline. The error bars shown reflect only the statistical uncertainties. The foreground model is the best-fit power law model from [34].

Chapter 10

Cross correlation with Planck data and foregrounds

10.1 Cross spectra with Planck HFI maps

We compute cross spectra with three Planck 2018 HFI maps to quantify the contribution of galactic dust to our B-mode auto spectrum. We compute the ten unique auto and cross spectra between four frequency channels:

- POLARBEAR map
- Planck 143 GHz frequency map
- Planck 217 GHz frequency map
- Planck 353 GHz frequency map

We process the Planck PR3 full mission frequency maps through the POLARBEAR observing pipeline to create Planck maps as seen by POLARBEAR. This is done to simplify debiasing the pseudo spectrum. In principle it is possible to skip this step and use the Planck maps reprojected into the POLARBEAR pixelization. This would require computing a filter transfer function for the cross spectrum between a filtered map and an unfiltered map for the POLARBEAR cross Planck spectra and the filter transfer function for an unfiltered map for the Planck internal spectra. It should be noted that the filter transfer function implicitly accounts for the pixel window function and normalization of the pseudo spectrum and is therefore not expected to be identically one for an unfiltered map.

We also process 96 noise realizations from the Planck FFP10 noise simulation set for each frequency to establish the Planck noise bias. The POLARBEAR noise bias is estimated using 192 "signflip" noise realizations. We opted to use the full simulation set of 192 noise realizations for the POLARBEAR noise bias since generating these noise simulations is computationally cheap.

The three Planck auto spectra are formed using the alternate full auto spectrum pipeline described in Section 4.6. We compute the measured debiased power spectrum $\hat{C}_b$ by subtracting the mean noise bias computed with the 96 FFP10 simulations from the auto spectrum of the real map. This is done to avoid relying on same-frequency cross spectra in the Planck 2018 PR3 maps which are known to be contaminated by systematics at the lowest ℓ values [74]. it is possible to build robustness to these systematics by considering multiple Planck splits including the even ring / odd ring and half mission splits. This quickly becomes computationally difficult in our pipeline given the number of simulations required to simulate each Planck frequency and split. The observing matrix formalism implemented by the BICEP2 and *Keck Array* collaboration makes running very large numbers of simulations significantly faster [72, 34] than a standard simulation pipeline.

In the fiducial parameter likelihood we use the results of the fiducial cross spectrum estimator for the POLARBEAR data, however the POLARBEAR auto spectrum can be likewise computed by subtracting the auto spectrum of the "signflip" noise realizations from the auto spectrum of the real data. We find this estimate to be compatible with the fiducial cross spectrum estimate by comparing the numerical difference between the two power spectra to the difference between the two spectra in our MC simulation set. This comparison gives $\chi^2/\nu = 8.5/11$ corresponding to a PTE of 67%. We find a marginally larger effective number of degrees of freedom per band power and therefore marginally smaller statistical errors in the full auto spectrum pipeline compared to the fiducial power spectrum estimator.

The six off-diagonal spectra are formed directly from the cross spectra of the fully coadded maps assuming that systematics and noise are uncorrelated between frequencies and experiments. Planck does not expect to see systematics or noise correlations between frequencies.

We use the cross spectrum pipeline to simulate 12 CMB realizations with input $r \in \{0.0, 0.1, 0.2\}$ and a single PySM dust realization [77] scaled to match the measured dust emission on an overlapping patch of sky. PySM somewhat overestimates the dust emission on our patch of sky so we rescale the input map by a factor of 3.8 (in power spectrum space) to bring it into approximate agreement with the best fit model from [34].

10.2 Cross spectra with Planck LFI maps

The power spectrum estimation formalism follows the formalism used to compute the cross spectra with high frequency Planck data. The auto spectrum of the Planck 30 GHz full mission map [79] as seen by POLARBEAR is computed and the noise bias is subtracted using the Planck FFP10 noise realizations. We validate our pipeline using a set of CMB simulations with $r = 0.0$ added to a PySM map of Galactic synchrotron emission as a fiducial signal model for the 30 GHz channel. Our simulations assume that dust foregrounds are negligible at 30 GHz and that synchrotron foregrounds are negligible at 150 GHz. Due to the Planck beams at 30 GHz we only consider the first five band powers corresponding to $\ell \leq 300$.

10.3 Cross spectrum error bars

We use a quasi-analytic approach to estimate the uncertainty in the cross and auto spectra with Planck data. We use the approximation that every spectrum has the same effective number of degrees of freedom per band power b denoted ν_b. We estimate this from the fractional uncertainty in the auto spectrum of the Planck noise maps,

$$\nu_b = 2\left(\frac{\hat{A}_b}{\sigma(\hat{A}_b)}\right)^2. \tag{10.1}$$

It should be noted that different maps are expected to have somewhat different ν_b. This difference comes from two main effects. At low-ℓ, the effective number of degrees of freedom for a signal-only map approaches zero due to $E \to B$ leakage subtraction. When the $E \to B$ leakage becomes an $O(1)$ effect the variance on the power spectrum receives a large contribution from the subtracted E-mode spectrum that adds to the intrinsic sample variance of the B-mode spectrum. The effective number of degrees of freedom for the POLARBEAR noise is somewhat larger than the effective number of degrees of freedom for the Planck noise because the Planck noise follows the signal effective $f_{\rm sky}$ whereas the POLARBEAR noise follows the noise effective $f_{\rm sky}$ described in Section 4.5.

For the auto spectra we estimate the uncertainty of the measured power spectrum $\hat{C}_b$ using the best fit signal power spectrum C_b and mean noise bias N_b,

$$\Delta\hat{C}_b = \sqrt{\frac{2}{\nu_b}}(C_b + N_b). \tag{10.2}$$

Equivalently, the uncertainty in the measured cross spectrum can be written in the form:

$$\Delta\hat{C}_b^{AB} = \sqrt{\frac{1}{\nu_b}\left((C_{b,A} + N_{b,A})(C_{b,B} + N_{b,B}) + C_{b,AB}^{\,2}\right)}. \tag{10.3}$$

It should be noted that these uncertainties do not directly enter the likelihood model and are plotted for visualization purposes only. We compare these error bars to the error bars derived from our MC simulation set and find reasonable agreement with most of the scatter due to the difference in expected ν_b for the different maps. The CMB sample variance is negligible for all spectra. We use the same fixed ν_b approximation for both the HFI and LFI spectra. All of these spectra are shown in Figure 10.1.

10.4 Synchrotron contamination at 150 GHz

We compute an upper limit on polarized B-mode Galactic synchrotron emission in our field at 150 GHz. We model the synchrotron emission as a power law in ℓ and frequency. Specifically, we assume that the power spectrum at a given frequency takes the form

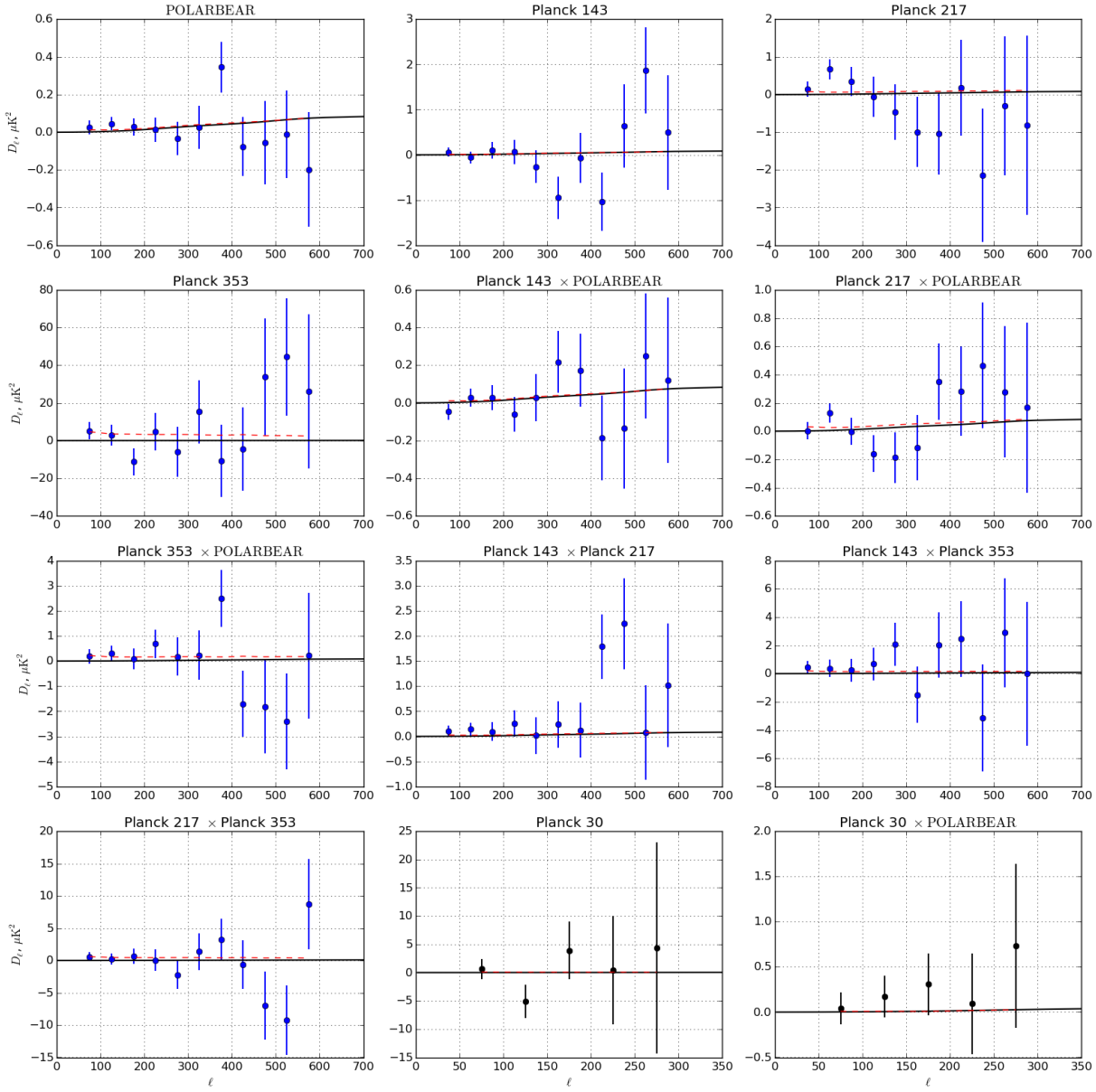

Figure 10.1: All cross and auto spectra measured with comparison with Planck maps. The auto and cross spectra with the Planck 30 GHz maps are indicated with black curves and are not used the fiducial r likelihood. Error bars show the fixed ν_b approximation assuming the simulations represent the underlying spectrum. The cross spectrum from our rescaled PySM model is shown in the red dashed curves. The POLARBEAR spectrum shown uses the alternate auto spectrum pipeline.

$$D_{\ell,\mathrm{sync}} = A_{\mathrm{sync}}\left(\frac{\ell}{\ell_0}\right)^{\alpha_{\mathrm{sync}}}\left(\frac{\nu}{\nu_0}\right)^{2\beta_{\mathrm{sync}}}, \tag{10.4}$$

in brightness units where the 2 is due to the fact that D_ℓ is quadratic in signal amplitude. We assumed fixed values for the power law indices $\alpha_{\mathrm{sync}} = -1.18$ taken from the highest Galactic latitudes in a recent measurement by S-PASS in conjunction with WMAP and Planck data [80]. We assume a value of $\beta_{\mathrm{sync}} = -3.2$ from the same analysis which is consistent with the prior used in [34]. Following previous work we choose pivots $\ell_0 = 80$ and $\nu_0 = 23$ GHz. We construct a one parameter likelihood following [81], relating the amplitude A_{sync} to the auto spectrum of the Planck 30 GHz map assuming a fixed CMB component with $A_{\mathrm{lens}} = 1$.

We find the likelihood of A_{sync} peaks at zero with a 95% upper limit of $A_{\mathrm{sync,23\ GHz}} \leq 21\mu K^2$. Using the fixed prior on α_{sync} and β_{sync}, this amplitude corresponds to a 95% upper limit on the synchrotron contamination at 150 GHz and $\ell = 80$ of $3.8 \times 10^{-4}\mu K^2$. We do not include synchrotron contamination in our fiducial r likelihood model as the contamination is deeply subdominant to dust foregrounds at 150 GHz.

We find the cross spectrum between Planck 30 GHz and POLARBEAR to be consistent with null. We do not directly use this spectrum in our estimate of synchrotron contamination as this spectrum adds little constraining power on the spectral index β_{sync}.

10.5 Contamination from polarized point sources

Polarized point sources contribute a Poisson noise term to the level of B-mode power in our maps. The level of this contamination is expected to be negligible for our experimental sensitivity on r. An analysis in [78] finds that the expected contamination from point sources at 150 GHz is expected to be $r \simeq 0.02$. As a result we do not perform point source masking in the mapmaking and power spectrum estimation operations.

10.6 Likelihood model and parameter constraints

We fit the B-mode power spectrum from our data and cross correlation with Planck high frequency data to a CMB and single dust component model using a likelihood similar to [81] and [82]. A detailed explanation of this analysis will be shown in the forthcoming POLARBEAR results paper but a high level overview is provided here. For each bandpower, we write a $n_{\mathrm{freq}} \times n_{\mathrm{freq}}$ matrix of the measured cross spectra $\hat{\mathbf{C}}_b$ where $n_{\mathrm{freq}} = 4$ is the number of frequency channels. The likelihood $\mathcal{L}$ of a true spectrum $\mathbf{C}_b$ given measured $\hat{\mathbf{C}}_b$ is:

$$-2\ln\mathcal{L} = \sum_b \nu_b \Big\{ \mathrm{Tr}[\hat{\mathbf{C}}_b \mathbf{C}_b^{-1}] - \ln|\hat{\mathbf{C}}_b \mathbf{C}_b^{-1}| - n_{\mathrm{freq}} \Big\}. \tag{10.5}$$

We model the underlying $\mathbf{C}_b$ as a sum of CMB, dust and noise components,

$$\mathbf{C}_b = \mathbf{C}_b^{\rm CMB} + \mathbf{C}_b^{\rm dust} + \mathbf{N}_b. \tag{10.6}$$

Every element of the CMB cross spectrum matrix $\mathbf{C}_b^{\rm CMB}$ is equal within a bandpower because all spectra are computed in CMB temperature units. The CMB receives contributions from lensing and tensor B-mode signals,

$$\mathbf{C}_b^{\rm CMB} = r\mathbf{C}_b^{\rm tens} + A_{\rm lens}\mathbf{C}_b^{\rm lens}. \tag{10.7}$$

Here $A_{\rm lens}$ is the amplitude of the lensing B-mode signal.

The dust spectral energy distribution is treated as a modified black body in frequency and a power law in ℓ following [83] and subsequent work. We define a vector with $n_{\rm freq}$ entries

$$f(\beta_{\rm dust}, T_{\rm dust}) \propto \nu^{\beta_{\rm dust}-2} B(\nu, T_{\rm dust}) \tag{10.8}$$

where $\beta_{\rm dust}$ is the dust power law index and $B(\nu, T_{\rm dust})$ is the black body distribution at frequency ν and temperature $T_{\rm dust}$. The vector f is integrated over the instrument bandpasses and converted into CMB temperature units. The dust component of $\mathbf{C}_b$ can be written as

$$\mathbf{C}_b^{\rm dust} = A_{\rm dust}(f \otimes f)\left(\frac{\ell}{\ell_0}\right)^{\alpha_{\rm dust}}, \tag{10.9}$$

assuming a pivot value of $\ell_0 = 80$ and setting the normalization such that f is unity at 353 GHz.

The noise component $\mathbf{N}_b$ is entirely diagonal as the noise between frequency bands and experiments is expected to be uncorrelated. The value of the diagonal elements is taken from the "signflip" (FFP10) noise realizations for the POLARBEAR (Planck) frequency channels as described previously.

In total, our fiducial likelihood contains six parameters, r, $A_{\rm lens}$, $\alpha_{\rm dust}$, $\beta_{\rm dust}$, $T_{\rm dust}$, and $A_{\rm dust}$. The likelihood results will be released in the upcoming POLARBEAR results paper.

Chapter 11

Conclusions

We present a measurement of the CMB B-mode power spectrum from the multipole range $50 \leq \ell \leq 600$ using three seasons of POLARBEAR data taken with a continuously rotating HWP. We observe a 670 effective square degree patch located near the southern celestial pole that significantly overlaps with observations by South Pole experiments. Our data achieves a maximum naive map depth (before correction for the filter transfer function) of 16 μK-arcmin.

The use of a CRHWP for polarization modulation provides a powerful mitigation of low frequency noise. We show that the noise in our maps is consistent with a single source of low frequency noise in the time domain and find little sensitivity degradation above our lowest bandpower centered at $\ell = 80$. We provide some theories about the physical origin of this noise and propose mitigation strategies for future instruments.

We establish that our data are cleaned of systematics through a set of null tests and direct simulation of known systematics. We find that all expected sources of systematic contamination are below are statistical uncertainties and suggest ways in which they can be further controlled in upcoming experiments.

We observe a modest excess above the ΛCDM lensing signal in our lowest ℓ bins that is consistent with previously published foreground levels. We compute the cross spectrum of our data with the publicly available Planck 2018 high frequency maps and show that our low ℓ signal correlates with polarized emission from galactic dust at higher frequencies.

This thesis presents a further demonstration of degree-scale B-mode science from a mid-latitude site. We build on the work of the ABS experiment and show the deepest CMB maps yet produced with continuous polarization modulation. Future experiments including the Simons Array [53] and Simons Observatory [4] will build on these results with substantially improved statistical power.

Bibliography

[1] Kevork N. Abazajian et al. "CMB-S4 Science Book, First Edition". In: *arXiv e-prints* (Oct. 2016). arXiv: 1610.02743 [astro-ph.CO].

[2] C. L. Bennett et al. "Nine-year Wilkinson Microwave Anisotropy Probe (WMAP) Observations: Final Maps and Results". In: *The Astrophysical Journal* 208, 20 (Oct. 2013), p. 20. DOI: 10.1088/0067-0049/208/2/20. arXiv: 1212.5225.

[3] Planck Collaboration et al. "Planck 2018 results. I. Overview and the cosmological legacy of Planck". In: *arXiv e-prints* (July 2018). arXiv: 1807.06205 [astro-ph.CO].

[4] Peter Ade et al. "The Simons Observatory: science goals and forecasts". In: *Journal of Cosmology and Astro-Particle Physics* 2019.2, 056 (Feb. 2019), p. 056. DOI: 10.1088/1475-7516/2019/02/056. arXiv: 1808.07445 [astro-ph.CO].

[5] A. A. Penzias and R. W. Wilson. "A Measurement of Excess Antenna Temperature at 4080 Mc/s." In: *The Astrophysical Journal* 142 (July 1965), pp. 419–421. DOI: 10.1086/148307.

[6] R. H. Dicke et al. "Cosmic Black-Body Radiation." In: *The Astrophysical Journal* 142 (July 1965), pp. 414–419. DOI: 10.1086/148306.

[7] J. C. Mather et al. "Calibrator Design for the COBE Far-Infrared Absolute Spectrophotometer (FIRAS)". In: *The Astrophysical Journal* 512 (Feb. 1999), pp. 511–520. DOI: 10.1086/306805. eprint: astro-ph/9810373.

[8] Robert M Wald. *General relativity*. Chicago, IL: Chicago Univ. Press, 1984. URL: https://cds.cern.ch/record/106274.

[9] Steven Weinberg. *Gravitation and Cosmology: Principles and Applications of the General Theory of Relativity*. New York, NY: Wiley, 1972. URL: https://cds.cern.ch/record/100595.

[10] Planck Collaboration et al. "Planck 2018 results. VI. Cosmological parameters". In: *arXiv e-prints* (July 2018). arXiv: 1807.06209 [astro-ph.CO].

[11] Adam G. Riess et al. "Observational Evidence from Supernovae for an Accelerating Universe and a Cosmological Constant". In: *The Astronomical Journal* 116.3 (Sept. 1998), pp. 1009–1038. DOI: 10.1086/300499. arXiv: astro-ph/9805201 [astro-ph].

[12] S. Perlmutter et al. "Measurements of Ω and Λ from 42 High-Redshift Supernovae". In: *The Astrophysical Journal* 517.2 (June 1999), pp. 565–586. DOI: 10.1086/307221. arXiv: astro-ph/9812133 [astro-ph].

[13] Adam G. Riess et al. "Large Magellanic Cloud Cepheid Standards Provide a 1% Foundation for the Determination of the Hubble Constant and Stronger Evidence for Physics beyond ΛCDM". In: *The Astrophysical Journal* 876.1, 85 (May 2019), p. 85. DOI: 10.3847/1538-4357/ab1422. arXiv: 1903.07603 [astro-ph.CO].

[14] M. Tanabashi et al. "Review of Particle Physics". In: *Phys. Rev. D* 98 (3 Aug. 2018), p. 030001. DOI: 10.1103/PhysRevD.98.030001. URL: https://link.aps.org/doi/10.1103/PhysRevD.98.030001.

[15] Alan H. Guth. "The Inflationary Universe: A Possible Solution to the Horizon and Flatness Problems". In: *Phys. Rev.* D23 (1981). [Adv. Ser. Astrophys. Cosmol.3,139(1987)], pp. 347–356. DOI: 10.1103/PhysRevD.23.347.

[16] Andrei D. Linde. "A New Inflationary Universe Scenario: A Possible Solution of the Horizon, Flatness, Homogeneity, Isotropy and Primordial Monopole Problems". In: *Phys. Lett.* 108B (1982). [Adv. Ser. Astrophys. Cosmol.3,149(1987)], pp. 389–393. DOI: 10.1016/0370-2693(82)91219-9.

[17] Matias Zaldarriaga and Uroš Seljak. "All-sky analysis of polarization in the microwave background". In: *Physical Review D* 55.4 (Feb. 1997), pp. 1830–1840. DOI: 10.1103/PhysRevD.55.1830. arXiv: astro-ph/9609170 [astro-ph].

[18] Marc Kamionkowski and Ely D. Kovetz. "The Quest for B Modes from Inflationary Gravitational Waves". In: *Annual Review of Astronomy and Astrophysics* 54 (Sept. 2016), pp. 227–269. DOI: 10.1146/annurev-astro-081915-023433. arXiv: 1510.06042 [astro-ph.CO].

[19] Antony Lewis and Anthony Challinor. "Weak gravitational lensing of the CMB". In: *Physics Reports* 429.1 (June 2006), pp. 1–65. DOI: 10.1016/j.physrep.2006.03.002. arXiv: astro-ph/0601594 [astro-ph].

[20] Wayne Hu and Takemi Okamoto. "Mass Reconstruction with Cosmic Microwave Background Polarization". In: *The Astrophysical Journal* 574.2 (Aug. 2002), pp. 566–574. DOI: 10.1086/341110. arXiv: astro-ph/0111606 [astro-ph].

[21] C. L. Bennett et al. "Four-Year COBE DMR Cosmic Microwave Background Observations: Maps and Basic Results". In: *The Astrophysical Journal* 464 (June 1996), p. L1. DOI: 10.1086/310075. arXiv: astro-ph/9601067 [astro-ph].

[22] J. R. Bond et al. "CMB Analysis of Boomerang & Maxima & the Cosmic Parameters {Omega_tot,Omega_b ĥ2,Omega_cdm ĥ2,Omega_Lambda,n_s}". In: *arXiv e-prints* (Nov. 2000). arXiv: astro-ph/0011378 [astro-ph].

[23] D. N. Spergel et al. "First-Year Wilkinson Microwave Anisotropy Probe (WMAP) Observations: Determination of Cosmological Parameters". In: *ApJS* 148 (Sept. 2003), pp. 175–194. DOI: 10.1086/377226. eprint: arXiv:astro-ph/0302209.

[24] J. M. Kovac et al. "Detection of polarization in the cosmic microwave background using DASI". In: *Nature* 420.6917 (Dec. 2002), pp. 772–787. DOI: 10.1038/nature01269. arXiv: astro-ph/0209478 [astro-ph].

[25] T. Louis et al. "The Atacama Cosmology Telescope: Two-Season ACTPol Spectra and Parameters". In: *ArXiv e-prints* (Oct. 2016). arXiv: 1610.02360.

[26] J. W. Henning et al. "Measurements of the Temperature and E-mode Polarization of the CMB from 500 Square Degrees of SPTpol Data". In: *The Astrophysical Journal* 852.2, 97 (Jan. 2018), p. 97. DOI: 10.3847/1538-4357/aa9ff4. arXiv: 1707.09353 [astro-ph.CO].

[27] The POLARBEAR Collaboration: P. A. R. Ade et al. "Evidence for Gravitational Lensing of the Cosmic Microwave Background Polarization from Cross-Correlation with the Cosmic Infrared Background". In: *Physical Review Letters* 112.13, 131302 (Apr. 2014), p. 131302. DOI: 10.1103/PhysRevLett.112.131302. arXiv: 1312.6645.

[28] D. Hanson et al. "Detection of B-Mode Polarization in the Cosmic Microwave Background with Data from the South Pole Telescope". In: *Physical Review Letters* 111.14, 141301 (Oct. 2013), p. 141301. DOI: 10.1103/PhysRevLett.111.141301. arXiv: 1307.5830 [astro-ph.CO].

[29] The POLARBEAR Collaboration: P. A. R. Ade et al. "A Measurement of the Cosmic Microwave Background B-Mode Polarization Power Spectrum at Sub-Degree Scales from 2 years of POLARBEAR Data". In: *Astrophys. J.* 848.2 (2017), p. 121. DOI: 10.3847/1538-4357/aa8e9f. arXiv: 1705.02907 [astro-ph.CO].

[30] The BICEP2 Collaboration: P. A. R. Ade et al. "Detection of B-Mode Polarization at Degree Angular Scales by BICEP2". In: *Physical Review Letters* 112.24, 241101 (June 2014), p. 241101. DOI: 10.1103/PhysRevLett.112.241101. arXiv: 1403.3985.

[31] The BICEP2 and Keck Array Collaborations: P. A. R. Ade et al. "BICEP2/Keck Array V: Measurements of B-mode Polarization at Degree Angular Scales and 150 GHz by the Keck Array". In: *The Astrophysical Journal* 811, 126 (Oct. 2015), p. 126. DOI: 10.1088/0004-637X/811/2/126. arXiv: 1502.00643.

[32] R. Keisler et al. "Measurements of Sub-degree B-mode Polarization in the Cosmic Microwave Background from 100 Square Degrees of SPTpol Data". In: *The Astrophysical Journal* 807, 151 (July 2015), p. 151. DOI: 10.1088/0004-637X/807/2/151. arXiv: 1503.02315.

[33] The BICEP2/Keck and Planck Collaborations: P. A. R. Ade et al. "Joint Analysis of BICEP2/Keck Array and Planck Data". In: *Physical Review Letters* 114.10, 101301 (Mar. 2015), p. 101301. DOI: 10.1103/PhysRevLett.114.101301. arXiv: 1502.00612.

[34] BICEP2 Collaboration and Keck Array Collaboration: Ade, P. A. R. et al. "Constraints on Primordial Gravitational Waves Using Planck, WMAP, and New BICEP2/Keck Observations through the 2015 Season". In: *Physical Review Letters* 121.22, 221301 (Nov. 2018), p. 221301. DOI: 10.1103/PhysRevLett.121.221301. arXiv: 1810.05216.

[35] Akito Kusaka et al. "Results from the Atacama B-mode Search (ABS) experiment". In: *Journal of Cosmology and Astro-Particle Physics* 2018, 005 (Sept. 2018), p. 005. DOI: 10.1088/1475-7516/2018/09/005. arXiv: 1801.01218 [astro-ph.CO].

[36] K. Arnold et al. "The bolometric focal plane array of the POLARBEAR CMB experiment". In: *Society of Photo-Optical Instrumentation Engineers (SPIE) Conference Series*. Vol. 8452. Society of Photo-Optical Instrumentation Engineers (SPIE) Conference Series. Sept. 2012. DOI: 10.1117/12.927057. arXiv: 1210.7877 [astro-ph.IM].

[37] Z. D. Kermish et al. "The POLARBEAR experiment". In: *Society of Photo-Optical Instrumentation Engineers (SPIE) Conference Series*. Vol. 8452. Society of Photo-Optical Instrumentation Engineers (SPIE) Conference Series. Sept. 2012. DOI: 10.1117/12.926354. arXiv: 1210.7768 [astro-ph.IM].

[38] Y. Mizugutch, M. Akagawa, and H. Yokoi. "Offset Dual Reflector Antenna". In: *ISA Proceedings* (1976), pp. 2–5.

[39] C. Dragone. "Offset multireflector antennas with perfect pattern symmetry and polarization discriminationa". In: *The Bell System Technical Journal* (1978), pp. 2663–2684.

[40] Huan Tran et al. "Comparison of the crossed and the Gregorian Mizuguchi-Dragone for wide-field millimeter-wave astronomy". In: *Appl. Opt.* 47.2 (Jan. 2008), pp. 103–109. DOI: 10.1364/AO.47.000103. URL: http://ao.osa.org/abstract.cfm?URI=ao-47-2-103.

[41] M. A. Dobbs et al. "Frequency multiplexed superconducting quantum interference device readout of large bolometer arrays for cosmic microwave background measurements". In: *Review of Scientific Instruments* 83.7, 073113-073113-24 (July 2012), pages. DOI: 10.1063/1.4737629. arXiv: 1112.4215 [astro-ph.IM].

[42] The POLARBEAR Collaboration: P. A. R. Ade et al. "A Measurement of the Cosmic Microwave Background B-mode Polarization Power Spectrum at Sub-degree Scales with POLARBEAR". In: *The Astrophysical Journal* 794, 171 (Oct. 2014), p. 171. arXiv: 1403.2369.

[43] The POLARBEAR Collaboration: P. A. R. Ade et al. "Measurement of the Cosmic Microwave Background Polarization Lensing Power Spectrum with the POLARBEAR experiment". In: *Physical Review Letters* 113 (2 July 2014), p. 021301. DOI: 10.1103/PhysRevLett.113.021301. arXiv: 1312.6646.

[44] Peter A. R. Ade et al. "POLARBEAR constraints on cosmic birefringence and primordial magnetic fields". In: *Physical Review D* 92.12, 123509 (Dec. 2015), p. 123509. DOI: 10.1103/PhysRevD.92.123509. arXiv: 1509.02461 [astro-ph.CO].

[45] J. Errard et al. "Modeling Atmospheric Emission for CMB Ground-based Observations". In: *The Astrophysical Journal* 809.1, 63 (Aug. 2015), p. 63. DOI: 10.1088/0004-637X/809/1/63. arXiv: 1501.07911 [astro-ph.IM].

[46] D. Poletti et al. "Making maps of Cosmic Microwave Background polarization for B-mode studies: the POLARBEAR example". In: *Astronomy and Astrophysics* 600, A60 (Aug. 2016), A60. arXiv: 1608.01624 [astro-ph.IM].

[47] POLARBEAR Collaboration et al. "A Measurement of the Cosmic Microwave Background B-mode Polarization Power Spectrum at Subdegree Scales from Two Years of POLARBEAR Data". In: *The Astrophysical Journal* 848.2, 121 (Oct. 2017), p. 121. DOI: 10.3847/1538-4357/aa8e9f. arXiv: 1705.02907 [astro-ph.CO].

[48] Toshiya Namikawa et al. "Evidence for the Cross-correlation between Cosmic Microwave Background Polarization Lensing from POLARBEAR and Cosmic Shear from Subaru Hyper Suprime-Cam". In: *arXiv e-prints* (Apr. 2019). arXiv: 1904.02116 [astro-ph.CO].

[49] M. Aguilar Faundez et al. "Cross-correlation of POLARBEAR CMB Polarization Lensing with High-z Sub-mm Herschel-ATLAS galaxies". In: *arXiv e-prints* (Mar. 2019). arXiv: 1903.07046 [astro-ph.CO].

[50] N.J. Miller, M. Shimon, and B.G. Keating. "CMB Beam Systematics: Impact on Lensing Parameter Estimation". In: *Phys. Rev.* D79 (2009), p. 063008. DOI: 10.1103/PhysRevD.79.063008. arXiv: 0806.3096 [astro-ph].

[51] BICEP2 Collaboration et al. "BICEP2 III: Instrumental Systematics". In: *The Astrophysical Journal* 814.2, 110 (Dec. 2015), p. 110. DOI: 10.1088/0004-637X/814/2/110. arXiv: 1502.00608 [astro-ph.IM].

[52] S. Takakura et al. "Performance of a continuously rotating half-wave plate on the POLARBEAR telescope". In: *Journal of Cosmology and Astroparticle Physics* 2017.05 (2017), p. 008. URL: http://stacks.iop.org/1475-7516/2017/i=05/a=008.

[53] A. Suzuki et al. "The POLARBEAR-2 and the Simons Array Experiments". In: *Journal of Low Temperature Physics* 184.3-4 (Aug. 2016), pp. 805–810. DOI: 10.1007/s10909-015-1425-4. arXiv: 1512.07299 [astro-ph.IM].

[54] Jason R. Stevens et al. "Designs for next generation CMB survey strategies from Chile". In: *Millimeter, Submillimeter, and Far-Infrared Detectors and Instrumentation for Astronomy IX*. Vol. 10708. Society of Photo-Optical Instrumentation Engineers (SPIE) Conference Series. July 2018, p. 1070841. DOI: 10.1117/12.2313898. arXiv: 1808.05131 [astro-ph.IM].

[55] T. Essinger-Hileman et al. "Systematic effects from an ambient-temperature, continuously rotating half-wave plate". In: *Review of Scientific Instruments* 87.9, 094503 (Sept. 2016), p. 094503. DOI: 10.1063/1.4962023. arXiv: 1601.05901 [astro-ph.IM].

[56] Satoru Takakura. "Characterization of a continuous polarization modulator using a half-wave plate for measurements of degree-scale cosmic microwave background with the POLARBEAR experiment". PhD thesis. Osaka University, June 2017.

[57] Kevin T. Crowley et al. "Studies of systematic uncertainties for Simons Observatory: detector array effects". In: *Proc. SPIE Int. Soc. Opt. Eng.* 10708 (2018), 107083Z. DOI: 10.1117/12.2313414. arXiv: 1808.10491 [astro-ph.IM].

[58] A. Pham. In preparation. PhD thesis. University of Melbourne, 2019.

[59] Elleflot Tucker. "Characterization of Multiplexed Transition Edge Sensor Bolometers for the POLARBEAR-2 Cosmic Microwave Background Experiment". In preparation. PhD thesis. University of California San Diego, 2017.

[60] Planck Collaboration et al. "Planck 2013 results. XXVIII. The Planck Catalogue of Compact Sources". In: *Astronomy and Astrophysics* 571, A28 (Nov. 2014), A28. DOI: 10.1051/0004-6361/201321524. arXiv: 1303.5088 [astro-ph.CO].

[61] T. Murphy et al. "The Australia Telescope 20 GHz Survey: the source catalogue". In: *Monthly Notices of the RAS* 402 (Mar. 2010), pp. 2403–2423. DOI: 10.1111/j.1365-2966.2009.15961.x. arXiv: 0911.0002 [astro-ph.GA].

[62] G. C. Jaehnig. "Measuring Cosmic Microwave Background Polarization with POLARBEAR and Simons Array". PhD thesis. University of Colorado at Boulder, 2018.

[63] J. Aumont et al. "Measurement of the Crab nebula polarization at 90 GHz as a calibrator for CMB experiments". In: *Astronomy and Astrophysics* 514, A70 (May 2010), A70. DOI: 10.1051/0004-6361/200913834.

[64] F. T. Matsuda et al. "Cross-polarization systematics due to Mizuguchi-Dragone condition breaking by a continuously rotating half-wave plate at prime focus in the Huan Tran telescope". In: vol. 10708. 2018. DOI: 10.1117/12.2313177. URL: https://doi.org/10.1117/12.2313177.

[65] B. G. Keating, M. Shimon, and A. P. S. Yadav. "Self-calibration of Cosmic Microwave Background Polarization Experiments". In: *The Astrophysical Journall* 762, L23 (Jan. 2013), p. L23. DOI: 10.1088/2041-8205/762/2/L23. arXiv: 1211.5734 [astro-ph.CO].

[66] S. Takakura et al. "Measurements of tropospheric ice clouds with a ground-based CMB polarization experiment, POLARBEAR". In: *Submitted to: Astrophys. J.* (2018). arXiv: 1809.06556 [astro-ph.IM].

[67] B. R. Johnson et al. "MAXIPOL: Cosmic Microwave Background Polarimetry Using a Rotating Half-Wave Plate". In: *The Astrophysical Journal* 665.1 (Aug. 2007), pp. 42–54. DOI: 10.1086/518105. arXiv: astro-ph/0611394 [astro-ph].

[68] A. Kusaka et al. "Publisher's Note: "Modulation of cosmic microwave background polarization with a warm rapidly rotating half-wave plate on the Atacama B-Mode Search instrument" [Rev. Sci. Instrum. 85, 024501 (2014)]". In: *Review of Scientific Instruments* 85.3, 039901 (Mar. 2014), p. 039901. DOI: 10.1063/1.4867655. arXiv: 1310.3711 [astro-ph.IM].

[69] E. Hivon et al. "MASTER of the Cosmic Microwave Background Anisotropy Power Spectrum: A Fast Method for Statistical Analysis of Large and Complex Cosmic Microwave Background Data Sets". In: *The Astrophysical Journal* 567 (Mar. 2002), pp. 2–17. DOI: 10.1086/338126. eprint: arXiv:astro-ph/0105302.

[70] Kendrick M. Smith. "Pseudo-C_ℓ estimators which do not mix E and B modes". In: *Physical Review D* 74.8, 083002 (Oct. 2006), p. 083002. DOI: 10.1103/PhysRevD.74.083002. arXiv: astro-ph/0511629 [astro-ph].

[71] K. M. Smith and M. Zaldarriaga. "General solution to the E-B mixing problem". In: *Physical Review D* 76.4, 043001 (Aug. 2007), p. 043001. DOI: 10.1103/PhysRevD.76.043001. eprint: astro-ph/0610059.

[72] BICEP2 Collaboration and Keck Array Collaboration: Ade, P. A. R. et al. "BICEP2/Keck Array. VII. Matrix Based E/B Separation Applied to BICEP2 and the Keck Array". In: *The Astrophysical Journal* 825, 66 (July 2016), p. 66. DOI: 10.3847/0004-637X/825/1/66. arXiv: 1603.05976 [astro-ph.IM].

[73] Emory F. Bunn et al. "E/B decomposition of finite pixelized CMB maps". In: *Physical Review D* 67.2, 023501 (Jan. 2003), p. 023501. DOI: 10.1103/PhysRevD.67.023501. arXiv: astro-ph/0207338 [astro-ph].

[74] Planck Collaboration et al. "Planck 2018 results. III. High Frequency Instrument data processing and frequency maps". In: *arXiv e-prints* (July 2018). arXiv: 1807.06207 [astro-ph.CO].

[75] Colin Bischoff. "Observing the Cosmic Microave Background Polarization Anisotropy at 40 GHz with QUIET". PhD thesis. University of Chicago, Aug. 2010.

[76] Immanuel Buder. "Measurement of the CMB Polarization at 95 GHz from QUIET". PhD thesis. -, Sept. 2012.

[77] B. Thorne et al. "The Python Sky Model: software for simulating the Galactic microwave sky". In: *Monthly Notices of the RAS* 469.3 (Aug. 2017), pp. 2821–2833. DOI: 10.1093/mnras/stx949. arXiv: 1608.02841 [astro-ph.CO].

[78] R. A. Battye et al. "Statistical properties of polarized radio sources at high frequency and their impact on cosmic microwave background polarization measurements". In: *Monthly Notices of the Royal Astronomical Society* 413.1 (May 2011), pp. 132–148. DOI: 10.1111/j.1365-2966.2010.18115.x. arXiv: 1003.5846 [astro-ph.CO].

[79] Planck Collaboration et al. "Planck 2018 results. II. Low Frequency Instrument data processing". In: *arXiv e-prints* (July 2018). arXiv: 1807.06206 [astro-ph.CO].

[80] N. Krachmalnicoff et al. "S-PASS view of polarized Galactic synchrotron at 2.3 GHz as a contaminant to CMB observations". In: *Astronomy and Astrophysics* 618, A166 (Oct. 2018), A166. DOI: 10.1051/0004-6361/201832768. arXiv: 1802.01145 [astro-ph.GA].

[81] Samira Hamimeche and Antony Lewis. "Likelihood analysis of CMB temperature and polarization power spectra". In: *Physical Review D* 77.10, 103013 (May 2008), p. 103013. DOI: 10.1103/PhysRevD.77.103013. arXiv: 0801.0554 [astro-ph].

[82] Jean-Francois Cardoso et al. "Component separation with flexible models. Application to the separation of astrophysical emissions". In: *arXiv e-prints* (Mar. 2008). arXiv: 0803.1814 [astro-ph].

[83] Planck Collaboration Int. XXX. "Planck intermediate results. XXX. The angular power spectrum of polarized dust emission at intermediate and high Galactic latitudes". In: *A&A* 586, A133 (2016), A133. DOI: 10.1051/0004-6361/201425034. arXiv: 1409.5738.